CARBON NANOTUBES / MANGANESE DIOXIDE NANO-STRUCTURED PLANAR MACRO, 3D MICRO, AND SOLID-STATE SUPERCAPACITORS

By

Serkan Akbulut

Dissertation

Submitted to the Faculty of the

Graduate School of Vanderbilt University

in partial fulfillment of the requirements

for the degree of

DOCTOR OF PHILOSOPHY

in

Electrical Engineering

June 30, 2017

Nashville, Tennessee

Approved:

Weng Poo Kang, Ph.D.

Supil Raina, Ph.D.

Bharat Bhuva, Ph.D.

Deyu Li, Ph.D.

Yaqiong Xu, Ph.D.

Richard Mu, Ph.D.

To my dearest parents, Mr. Mehmet Akbulut and Mrs.Gulseren Akbulut and sister, Serap Durmaz

ACKNOWLEDGEMENTS

I would first like to thank my academic and research advisor, Prof. Weng Poo Kang, for his assistance, guidance and encouragement throughout my study at Vanderbilt University. He has been the constant source of inspiration, encouraging me through my failures and inspiring me to achieve more. I am thankful to him for giving me the opportunity to work in this research project, which helped me gain confidence in my research work and providing fresh insight to further enhance my dissertation.

I would like to give special thanks to my co-advisor, Dr. Supil Raina. Whenever I have run into difficulties, technical or with life, I have turned up in his desk. He is always there to help. Without his help, this work would have never seen the light of the day. Whatever laboratory skills I have acquired, all are because of him. He was the one, who showed me the path going to success with his wisdom and huge experience in both academic and daily life.

I am grateful to my dissertation committee members Professors Bharat Bhuva, Deyu Li, Yaqiong Xu, and Richard Mu for their valuable advice, support, and encouragement. I am thankful to all my present and ex-colleagues and faculty members associated with the Vanderbilt Diamond Microelectronics group for their help and support throughout my graduate studies: Mr. Mick Howell, Dr. Siyu Wei, Dr. Nikkon Ghosh, Dr. Shao-Hua Hsu, Dr. William Paxton, and Mesut Yilmaz.

I would like to thank the Turkish Ministry of Education for the scholarship to pursue my graduate study in the United States. Also, I must express my gratitude to Turkish Government for giving me such an excellent opportunity, and supporting me in every step of my academic life. This study would not have been possible without their

support. I am also thankful for the Electrical Engineering Department of Vanderbilt University for financial support as teaching assistantship and research assistantship.

My deepest thanks go to my family and I would like to express my greatest respect to them. Without their continuous love, support, and encouragement throughout my life, I could not have completed anything. First of all, I would like to thank my mother Gulseren Akbulut and my father Mehmet Akbulut, who brought me into this world, supported me and everything else in between. I must express my gratitude to my lovely sister Serap Durmaz, who has always supported my endless pursuit of higher education, and all other members of my family that I could not list their names here. I love you all forever.

TABLE OF CONTENTS

LIST OF FIGURES

Figure **Page**

LIST OF TABLES

Table **Page**

CHAPTER I

INTRODUCTION

Advanced energy storage technologies will play an important role in the widespread deployment of renewable energy sources. Solar and wind energy are very consistent from year to year but have significant variation over shorter time frames. Battery technology has been prevalent for some time now, but the high cost and small capacity is a hindrance in its large-scale deployment. New battery technologies are being investigated. Another promising solution to the supplement storage of electricity is offered by electrochemical supercapacitors or ultracapacitors which are able to deliver a huge amount of energy in a short time [1-3].

1.1 Supercapacitors as Energy Storage Devices

Power density and energy density are the two key parameters for characterizing the performance of an energy storage device [4]. The ideal energy storage device should be characterized by both high power density and high energy density. Figure 1.1 shows the Ragone plot, specific energy (Wh/kg) vs. specific power (W/kg), of various energy storage technologies [5]. To use the analogy of an electric car, the specific energy provides information on how far the car can travel, while specific power tells us how fast it can go. From the Ragone plot we can see that Li-ion batteries are superior, in terms of specific energy, to other rechargeable energy storage options such as nickel metal hydride (Ni-MH), nickel-cadmium (NiCad) and electrochemical capacitors.

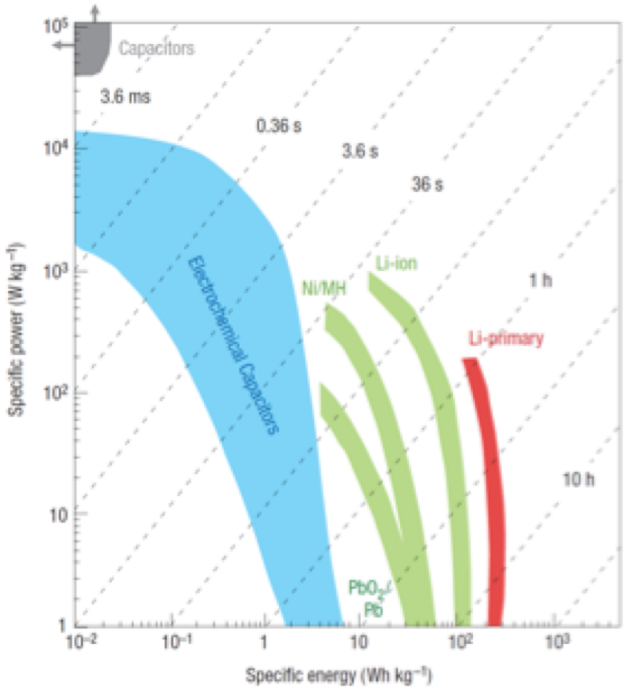

Figure 1.1 Ragone plot of specific power versus specific energy for various electrical energy storage and conversion devices [5].

However, the Li-ion technology still lags in terms of power density, as well as key issues such as safety. However, the latest innovation of supercapacitors, using pseudocapacitive materials, could deliver high power density and significantly higher energy density. In comparison with batteries, supercapacitors have the following advantages: shorter charge/discharge time, longer cycle life, wider working temperature range, and higher power density. Table 1.1 summarizes the performance comparison between supercapacitors and lithium-ion batteries [6].

An emerging energy storage solution that bridges the gap between conventional capacitors and rechargeable batteries, namely supercapacitors, will grow based mainly on adoption in transportation applications like hybrid electric vehicles and micro-hybrids. According to Lux research, the overall market for supercapacitors is expected to expand from $416 million in 2013, to an $836 million market in 2018 [6].

Table 1.1 Comparison of performance characteristics of supercapacitors and lithium ion batteries [6].

Function	Supercapacitor	Lithium-ion (general)
Charge time	1–10 seconds	10–60 minutes
Cycle life	1 million or 30,000h	500 and higher
Cell voltage	2.3 to 2.75V	3.6 to 3.7V
Specific energy (Wh/kg)	5 (typical)	100–200
Specific power (W/kg)	Up to 10,000	1,000 to 3,000
Cost per Wh	$20(typical)	$2 (typical)
Service life (in vehicle)	10 to 15 years	5 to 10 years
Charge temperature	–40 to 65°C (–40 to 149°F)	0 to 45°C (32°to 113°F)
Discharge temperature	–40 to 65°C (–40 to 149°F)	–20 to 60°C (–4 to 140°F)

The latest innovations of supercapacitors have led to other applications that may involve power supply optimization in electric vehicles, which could help to reduce pollution and improve air quality in future [7]. There are lots of places where supercapacitors are replacing batteries entirely such as hybrid bus brakes [7], seaport cranes [8], memory backup systems in computers [9], emergency doors on planes [10], portable consumer electronics [10], and wind turbines. Portable fuel cells also provide a new market for supercapacitors to enhance peak-load performance.

1.2 Why 3D Micropatterned Supercapacitors?

The development of miniaturized electronic systems has increased the demand for miniaturized power sources that can be integrated into electromechanical systems (MEMS), micro-robots, active radio frequency identification (RFID), implantable medical devices and wireless sensors. Among all power generation systems such as energy harvesters and micro-fuel cells for miniaturized devices, micro-batteries are considered to be the main candidates for these applications. However, micro-batteries

have certain drawbacks such as lower power density, and a limited lifetime compared to their larger counterparts. Due to low power densities, micro-batteries remain insufficient for power harvesting devices or some specific applications that require high power in a very short time. Micro-supercapacitors as energy storage devices with a high power density can be paired with micro-batteries to improve the cycle lifetime or can be coupled with energy harvesting devices to provide peak power and store the generated energy. Despite the need for micro-supercapacitors for specific applications, such as power harvesting devices, there has been exponential growth in the number of reports about fabricating such devices. Most of the recent research related to micro-supercapacitors has focused on increasing power and energy densities by changing the architecture of the devices and improving the material properties. Various nanostructured materials have been used as electrode materials to improve the material properties for micro-supercapacitors. From the device architecture aspect, it has been shown that device performance can be improved by employing three-dimensional (3D) micropatterned electrodes with highly effective surface areas. However, more facile fabrication techniques are needed to expand the application of this type of micro-supercapacitor [11,12].

1.3 Objective of this research

The prime objective of this research is to develop advanced three-dimensional supercapacitors with higher energy and power densities to meet the requirements of future applications. Conventionally, carbonaceous nanomaterials such as activated carbons, carbide derived carbons, graphene, carbon onions, and carbon nanotubes (CNT)

have been used to fabricate EDLC supercapacitors; while transition metal oxides such as ruthenium oxide and conductive polymers such as polypyrrole (PPy) have been used as materials for pseudo-capacitive supercapacitors. Herein I propose to improve the energy and power density of supercapacitors by exploring nano-composite structures where transition metal oxides are combined with three dimensional, high specific surface area and conducting carbon nanotubes to achieve the high performance, advanced devices in a) planar supercapacitors; b) micropatterned 3D micro-supercapacitors; and c) solid-state supercapacitors. In order to achieve high specific energy and specific power, the device structure is very critical. Fabrication of 3D structure for electrochemical micro-supercapacitors is a promising approach to meet those targets by providing large effective surface area per unit device footprint. Additionally. this dissertation aims to synthesize, fabricate and characterize solid polymer electrolytes for solid-state supercapacitors. Solid polymer electrolytes replace flammable liquid (organic) electrolytes, and act as separators while supporting ion transport through them and do not require complex encapsulation materials and technologies. The research includes:

- Fabrication and characterization of supercapacitors on silicon substrate.
- Fabrication and characterization of supercapacitors on highly flexible graphite foil substrates.
- Fabrication and characterization of double-sided supercapacitors on highly flexible graphite foil substrates.
- Integration of double-sided MnO_2/CNT/Graphite electrodes to fabricate multi-layer supercapacitor prototype cell.

- Design, fabrication and characterization of the micro supercapacitors based on three-dimensional micro-patterned MnO_2/CNT/Si electrodes.
- Design, fabrication, and characterization of the solid-state supercapacitors based on planar and micro-electrode array.

1.4 Organization of the Dissertation

There are six chapters in this dissertation and they have been organized in the following structure and explanation corresponding to each of them:

- ***Chapter I*** gives a brief introduction about the energy storage technologies and provides a comparison between Li-ion batteries and supercapacitors. Also, the importance of 3D micro-patterned supercapacitors are included followed by the objective of this research, to develop advance energy storage devices based on three dimensional supercapacitors consisting of hybrid structure achieved by combining pseudocapacitive materials with carbon nanotubes.
- ***Chapter II*** reviews the supercapacitors as energy storage solutions, compares benefits of 3D structure vs. 2D structure and investigates 3D micro-batteries and micro-supercapacitors. Additionally, the properties and applications of the solid-state supercapacitors are described.
- ***Chapter III*** describes the fabrication, material analysis and characterization of planar supercapacitor electrodes consisting of MnO_2/CNT on silicon and graphite substrates. Subsequently, the development of a double-sided MnO_2/CNT supercapacitor electrodes on graphite foil and their integration into a working

prototype symmetric cell is presented and the cell performance is characterized and discussed. .

- ***Chapter IV*** provides the development of micropatterned 3D MnO_2/CNT supercapacitor microelectrode arrays on silicon substrate, including the microelectrode design, fabrication, characterization, results, and discussion.
- ***Chapter V*** describes the designing, fabrication, material analysis and cell performance characterics of the advanced flexible solid-state supercapacitors based on 3D nanostructured MnO_2/CNT electrodes on graphite and solid-state electrolyte.
- ***Chapter VI*** summarizes the dissertation and provides recommendations for future work.

CHAPTER II

BACKGROUND AND LITERATURE REVIEW

2.1 Introduction

Over the past few decades, there has been significant concern among people due to environmental changes resulting from the use of non-renewable energy sources. Global warming, damages to ecosystem and biodiversity have resulted in greater focus on research and development of alternative energy sources. However, it is not possible to meet the rising global demands of energy, merely by using renewable energy resources. Batteries and supercapacitors (ECs) (also known as electrochemical or ultra-capacitors) are two important devices that have a growing impact in our lives by storing energy in applications ranging from portable electronics, power tools, hybrid vehicles, electric vehicles, and large industrial equipment [13]. In the field of energy storage devices, significant progress and effort has been made in developing the next generation of Li-ion batteries and other types of secondary batteries to improve their performance to meet the requirements of more challenging applications. The different types of nanomaterials as battery electrodes along with advances in packaging, electrolytes, and fabrication methods, have resulted in improved performance of batteries. However, the current battery technologies have performance limitations such as short cycle life, slow charge/discharge rates (limited power capability) and calendar life [14]. Batteries have relatively slow power delivery and uptake, therefore there is a need for high power energy systems in a number of applications which has been the motivation behind the research on supercapacitors. The first electrochemical charge storage devices using

double layer charge storage was patented by Becker [15] from General Electric Company in 1957. The Nippon Electric Company (NEC) developed the first commercial electrochemical capacitor and used the term “supercapacitor” for the developed device in 1978. Panasonic developed its own commercial supercapacitor called “Goldcap” in the Central Research Laboratory of Panasonic in 1978. Electrochemical capacitors were restricted to replacing batteries for memory back-ups until the late 1970s. Professor B.E Conway, University of Ottowa, carried out extensive research on new mechanism for electrochemical capacitors based on a faradic reaction on the surface of the electrode materials and was termed as pseudo-capacitance. Due to increased amount of possible applications, supercapacitors attracted a lot of attention in the early 1990s. In the present days, leading companies such as Maxwell technologies, AVX, Cooper, ELNA, NNC, Cap-XX, and among others have invested in the development of supercapacitors [16].

2.2 Electrochemical Properties of Supercapacitors

Electrochemical properties of supercapacitors can be emphasized by their capacitance, voltage, power and energy densities. The capacitance of a supercapacitor is commonly reported in terms of specific capacitance which is the capacitance normalized by surface area, weight or volume of the cell or single electrode. In general, the capacitance of the supercapacitors depends on the amount of charge stored on the electrodes, which in turn depends on the properties of the each electrode. A voltage will build up across the two electrodes while a supercapacitor is charging. The maximum energy stored in a supercapacitor is calculated by:

$$W = \frac{1}{2} C V_0^2 \text{.....1.1}$$

where W (Wh) is the energy, C (F) is the capacitance, and V (V) is the operating voltage. By increasing C and V, the energy stored in the supercapacitor can be increased. The resistance of the electrolyte affects the equivalent series resistance of the cell thus reducing the maximum obtainable power, which is determined by the following [17]:

$$P = \frac{V^2}{4R} \text{.....1.2}$$

Where P (W) is the power, R is the total equivalent series resistance (ESR). To improve the power performance, the supercapacitors must have small ESR to be charged or discharged fast. The ESR depends on the electrolyte, the current collectors, and the material of electrodes.

To obtain supercapacitors with high energy and power density, the current collectors must have good conductivity; the electrodes must have large surface area and small resistance; electrolytes must have high ionic conductivity. Among these, the increase of the effective surface area of electrodes to support greater mass loading becomes the first priority for the design of supercapacitors [18].

2.3 Charge Storage Mechanisms of Supercapacitors

Latest innovations in technology have made supercapacitors an integral part of energy storage systems for high power applications [19]. Based on the charge storage mechanism, supercapacitors can be divided into three typical classes: (i) electrochemical

double layer capacitors (EDLCs), (ii) pseudocapacitors, and (iii) hybrid-supercapacitors. Electrochemical double layer capacitors include two electrodes immersed in an electrolyte solution with a semi-permeable separator that prevents electrical contact between the two electrodes, but allows ionic diffusion [20]. When an electrical potential is applied to the electrodes, the counter ions approach the electrode surface and form a double layer balancing the electrode charge [21].

As compared to the charge storage mechanism of EDLC, (that is non-faradaic in origin), pseudocapacitors store energy by faradaic reactions involving electron transfer that follows reduction-oxidation (redox) reactions and intercalation processes [22,23].

In addition to pseudocapacitors and EDLCs, hybrid capacitors usually combine one EDLC capacitive electrode (as power source) with one battery-type electrode (as energy source) (pseudocapacitive or lithium insertion electrode) in the same cell [24]. In hybrid capacitor systems, the battery type electrode provides high energy density while the EDLC electrode provides high power capability in such systems. Although hybrid capacitors show high energy density and high capacitance compared with other charge storage mechanisms, there is a main drawback for these systems, the limited cyclability of the faradaic electrodes [25].

2.4 Electrode Materials for Supercapacitors

Supercapacitors (EDLCs) store charge solely on the electrode surface, increasing the surface area that's accessible to the electrolyte ions can result in higher capacitance values. Therefore, the main principle for high performance EDLCs is the use of electrochemically stable electrode materials with high surface area and conductivity.

Traditional supercapacitors use activated carbon as the active material on a metallic substrate as the current collector. Carbon is an excellent electrical conductor, and chemically stable with a wide electrochemical window in a large variety of electrolytes. There are several carbon-based materials available commercially, such as carbon nanotubes (CNT), activated carbon (AC), carbon fibers, graphite and its compounds, that are used for the production of supercapacitors [26].

Due to their low cost, high surface area, and relatively good electrical properties, activated carbon is the most widely used materials for supercapacitor electrodes [27]. Production of activated carbon (AC) usually follows physical, chemical, or electrochemical activation of the carbonaceous materials such as wood, pitch, coal, coke or fruit shell such as coconut or even synthetic polymer precursors. The most important step for the production of AC is the electrochemical activation, which usually performed by oxidation and reduction of carbon electrodes in an electrochemical cell. The specific surface area is generally from 450 to 2600 m^2/g, corresponding to the high specific capacitance around 100 –150 F/g in organic electrolyte with operating voltage up to 3.2V [7]. Although AC has a very high surface area, the main challenge for these materials is the control of their pore size distribution and pore structure. To improve the energy and power density of AC based supercapacitors, most of the recent work has been focused on designing ACs with well-controlled interconnected pore structure [7].

Another type of carbon material that is used for supercapacitor applications is template-derived carbon. Compared to ACs, the template-derived carbons offer a much higher specific surface area with excellent network of interconnected pores, which allow easy ionic transportation. As for their recent performance, template-derived carbon based

supercapacitors with very high surface areas can exhibit a very high specific capacitance of 220 Fg^{-1}. One of the major problems with these carbons is wettability by electrolyte and restricted access to the surface, which is particularly caused by very small pores (d~0.8nm and less) and the narrow pore size distribution in carbon [27].

Over the last decade, a new type of carbon material has attracted a lot of attention for supercapacitor applications, namely carbon nanotubes (CNT). CNTs have many potential applications due to their electrical conductivity, excellent chemical properties, mechanical strength, and high surface area. CNTs based electrode offers exceptional energy and power performance due to the high surface area and the ability to functionalize the CNTs to optimize electrochemical supercapacitor properties. Large amounts of resources have been invested for understanding and developing the carbon nanotube material. Overall, the volume of nanotube research is growing, and commercial applications will not be far behind. There is a wide range of methods available for the synthesis of the CNTs. including laser ablation, arc discharge, and chemical vapor deposition (CVD) [28]. Among these techniques, CVD is a simple and economical technique for synthesizing CNTs at low temperature and ambient pressure. In the CVD technique, the catalyst, such as nickel, cobalt, stainless steel, gold, platinum, and many alloys, is one of the key aspects in carbon nanotube growth allowing for their synthesis under favorable conditions [28]. The specific surface area is around 100 m^2/g, corresponding to the high specific capacitance is generally between 15 –300 F/g reported for different configurations of CNTs [28].

Other types of carbon materials such as carbide-derived carbons (CDC), and carbon black are also under are also under extensive research for application as

supercapacitor electrode materials. Specific capacitances in the range of 130 to 270 F/g have been reported for CDC supercapacitor electrodes depending on chlorination temperature of carbide, the precursor carbide, and the electrolytes that were used to test the supercapacitors [7]. Table 2.1 presents properties and performance of various carbon-based supercapacitor electrodes.

The mechanism of charge storage in the pseudo-capacitor is by faradic reactions involving electron transfer or reduction-oxidation (redox) reactions that take place on the surface and the bulk of capacitive materials resulting in faradic current passing through the supercapacitor cell. This faradic reaction results in higher specific capacitance of pseudo-capacitors compared to EDLCs. However, since these faradic processes in bulk materials are generally very slow, pseudo-capacitors like batteries suffer from relatively low power density compared to EDLCs. The cation diffusion is slower and the charge transfer kinetics are less than optimum which affect the overall performance.

The most commonly used pseudocapacitive materials are: (i) conducting polymers and (ii) transition-metal oxides. Conducting polymers such as polypyrrole, polythiophene, polyaniline, and their derivatives have disadvantages over metal oxide based pseudocapacitors in terms of long-term stability, cost and cycle life, which limits their commercial potential. Various metal oxides such as RuO_2 [29], MnO_2 [30], V_2O_5 [31], NiOx [32], Co_3O_4 [33], and MoO_3 [34] have also been evaluated as a possible electrode material for pseudocapacitors because of their high conductivity and capacitance, long operation time, and high output [35]. Metal oxides that can be used for supercapacitor applications should be electronically conductive and should have two or more oxidation states that exist over a continuous potential range without irreversible

phase and structure changes. Ruthenium oxide has very high specific capacitance, electronic conductivity and also has three distinct oxidation states in a 0-1.2 V voltage range [8]. However, high cost of ruthenium oxide (RuO_2) makes it economically less attractive to use for electrode materials and its low (1V) potential window limits the application of supercapacitors based on RuO_2 to small electronic devices.

Table 2.1: Properties and performance of various carbon-based supercapacitor electrodes [7].

Materials	Specific Surface area/ m^2g^{-1}	Density/ gcm^{-3}	Aqueous electrolyte		Organic electrolyte	
			Fg^{-1}	Fcm^{-3}	Fg^{-1}	Fcm^{-3}
Commercial activated carbons (ACs)	1000–3500	0.4-0.7	<200	<80	<100	<50
Particulate carbon from SiC/TiC	1000–2000	0.5-0.7	170-220	<120	100-120	<70
Functionalized porous carbons	300–2200	0.5-0.9	150-300	<180	100-150	<90
Carbon nanotube (CNT)	120–500	0.6	50-100	<60	<60	<30
Templated porous carbons (TC)	500–3000	0.5-1	120-350	<200	60-140	<100
Activated carbon fibers (ACF)	1000–3000	0.3-0.8	120-370	<150	80-200	<120
Carbon cloth	2500	0.4	100-200	40-80	60-100	24-40
Carbon aerogels	400-1000	0.5-0.7	100-125	<80	<80	<40

Among these electrode materials, manganese oxide (MnO_2) has been regarded as the most appealing electrode materials for the next generation of electrochemical supercapacitors (ES) because of its outstanding capacitive performance, abundance, environment-friendliness and low cost. The charge storage mechanism in metal oxides in an electrochemical (EC) system, e.g. MnO_2 can be seen in equation 1. The pseudocapacitive (Faradaic) reactions occurring on the surface and the bulk of the

electrode involve the adsorption and desorption of alkali metal cations ($X^+ = Li^+$, Na^+, K^+) or protons ($X^+ = H^+$) [36].

$$MnO_2 + e^- + X^+ \leftrightarrow MnOOX \quad (1)$$

Despite its low price and a large theoretical capacity (1,370 $F.g^{-1}$), MnO_2 has many difficulties due to its low ion diffusion constant, Mn dissolution into the electrolyte [23], and low electronic conductivity (~10^{-6} $S.cm^{-1}$), which limits its application in the development of high performance supercapacitors [37-38].

To enhance the ionic conductivity, electrical conductivity, and specific capacitance of MnO_2-based electrodes, extensive efforts are placed on exploring hybrid composite structures where MnO_2 is combined with extremely conductive and high surface area materials. A hybrid, 3D, nanostructured material contains a carbon based material with a pseudo-capacitor material takes advantage of both high surface area substrate and pseudocapacitance to improve the energy and the power density of supercapacitor cells and have been extensively studied in recent years.

Forming hybrid structures give several advantages such as high surface area, absence of additives, shorter cation diffusion distance, lower contact resistance, and faster electron transfer. Figure 2.1 shows a comparison in terms of specific capacitance (F/g) among different supercapacitor materials based on carbon materials, conducting polymers, transition metal oxides, especially RuO_2 [24].

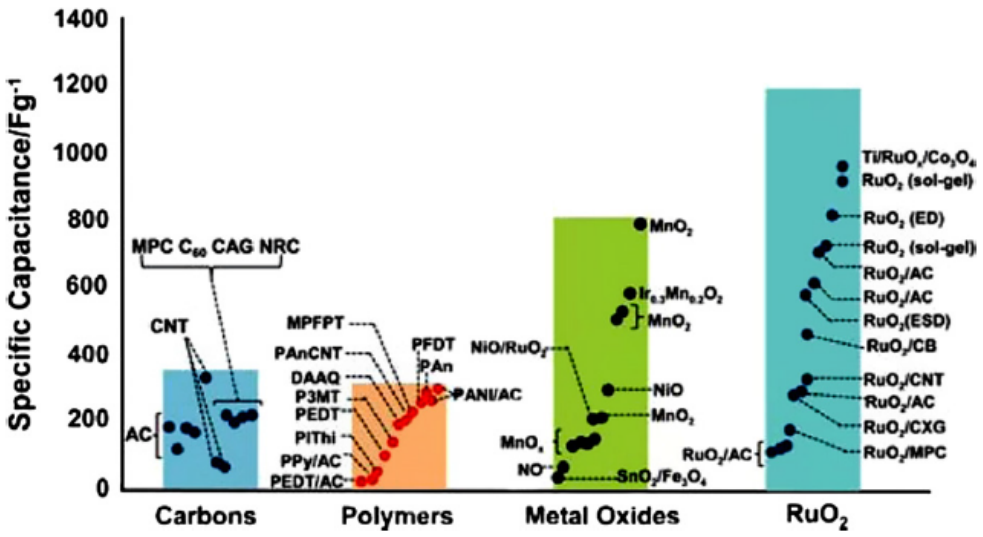

Figure 2.1 Properties and performance of various carbon-based supercapacitor electrodes. [24].

2.5 Electrolyte Materials for Supercapacitors

The electrolyte, which dwells between the two electrodes, is one of the most important supercapacitor components. The ionic conductivity of the electrolyte affects the equivalent series resistance (ESR) of the device, and thus its power output characteristics. The requirements for selection of the ideal electrolyte in supercapacitors are as follows: a high ionic concentration, a wide potential window, environmentally friendly, low cost, safety, high compatibility with active electrode materials, a wide operating temperature range, high purity, and easy packaging. A lot of research has gone into improving the overall performance of electrolytes to meet most of these requirements [39-41]. Figure 2.2 shows the effects of different properties of electrolytes on the supercapacitor performance [42].

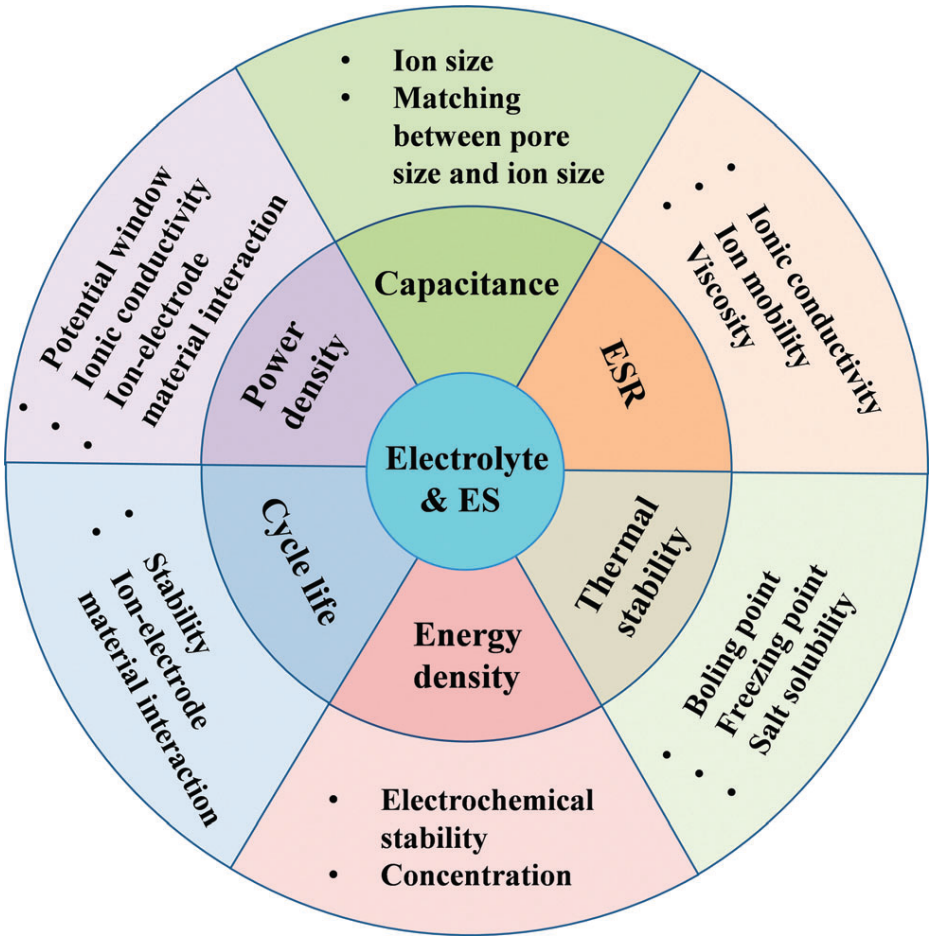

Figure 2.2 Effect of the properties of electrolytes on the energy storage performance of supercapacitor electrodes [42].

One of the criteria to classify different supercapacitors is the type of electrolyte used - liquid electrolytes or solid-state electrolytes. The liquid electrolyte for a supercapacitor can be aqueous or organic solutions as shown Fig.2.3.

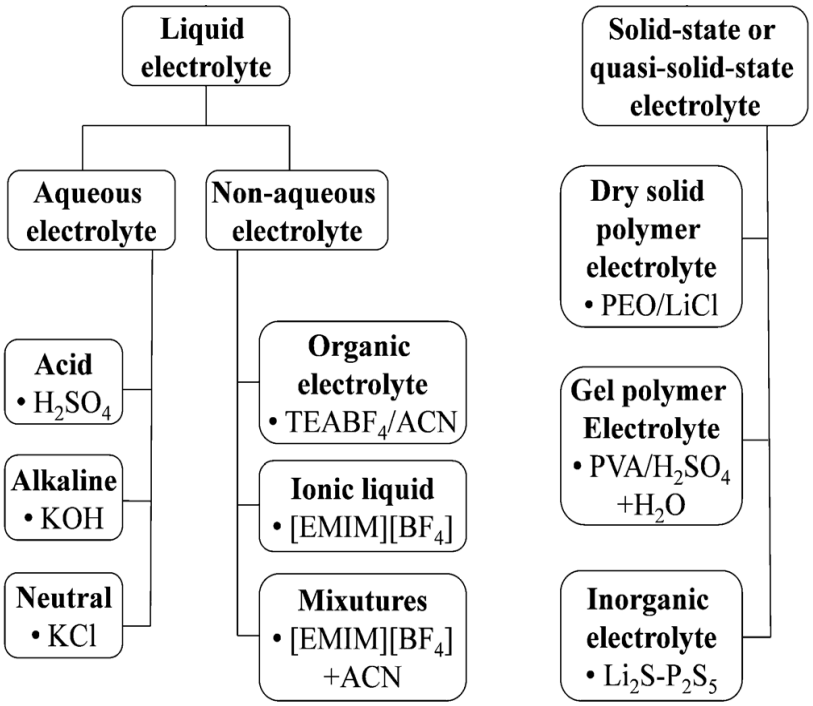

Figure 2.3 Classification of electrolytes for supercapacitors [42].

Aqueous electrolytes such as KCl, Na_2SO_4, H_2SO_4, and KOH offer low viscosity, excellent conductivity and low internal resistance but limit the operating voltage to 1 V [43,44]. Furthermore, aqueous electrolyte can be prepared and utilized in the laboratory conditions without needing special conditions while the organic electrolytes need safe handling protocols, in a glove box to avoid introduction of moisture.

Organic electrolytes allow a higher voltage limit ≥ 2.5 V depending on the electrodes, but suffer from lower conductivity, higher viscosity and can be flammable and toxic. However, organic electrolytes have been widely used because the higher voltage translates into higher specific energy and power values as both of them vary with the square of the voltage (V^2). Moreover, organic electrolytes also allow the use of cheaper

materials such as aluminum for the packages and current collectors. The most common organic electrolytes for the commercial supercapacitors consist of the conductive salts (tetraethylammonium tetrafluoroborate (TEATFB)) dissolved in the acetonitrile, butylene carbonate (BC), glutaronitrile (GLN), adiponitrile (ADN), and propylene carbonate (PC) solvents [45-48].

Ionic liquids are commonly known as low temperature molten salts with several potential advantages including, low vapor pressure, non-flammability, wide electrochemical and thermal stability [49]. However, there are several main drawbacks with most ionic liquids, such as high cost, high viscosity, and low ionic conductivity, which can limit their practical use in supercapacitors. Ionic liquids are mostly used at very high temperatures due to its low ionic conductivity at room temperature. Their physical and chemical properties can be highly variable due to their large variety of combinations of anions and cations. In this sense, ionic liquids are very attractive as supercapacitor electrolytes because the electrolyte compositions can be customized or optimized to meet certain requirements of supercapacitor performance such as the working temperature range, operative cell voltage, and equivalent series resistance (ESR) [50]. The development of ionic liquids for supercapacitor applications is still in the early stage and further progress is needed to ensure their full management.

Solid-state or quasi-solid-state electrolytes offer several advantages in terms of safety, higher operating temperature and easy packaging, although the ion diffusion in solid-state electrolyte cannot be as fast as in liquid electrolyte. Solid electrolytes can include both low melting point salts and polymer materials that contain free and mobile ions, however a vast majority of solid electrolytes are polymer electrolytes and only very

limited work has been focused on inorganic solid-materials such as ceramic electrolyte [51,52]. The polymer-based solid electrolytes for supercapacitors can be further classified into three types: the solid polymer electrolyte (SPEs), the gel polymer electrolyte (GPE) and the polyelectrolyte. Some studies called GPEs as quasi-solid-state due to the presence of a liquid phase in their fabrication process. GPEs have the highest ionic conductivity between these three types of solid-state electrolytes and they currently dominate the solid-state electrolyte based supercapacitor products [53].

The polymer-based solid electrolytes have been used for several kinds of supercapacitors such as EDLCs, pseudocapacitors and hybrid ESs with different kinds of electrode materials. When developing the polymer-based solid electrolytes for supercapacitor applications, the following requirements should be considered;

(i) High ionic conductivity at room temperature

(ii) Sufficient mechanical strength and dimensional stability

(iii) High chemical, electrochemical and thermal stability

In practice, it is difficult for a solid-sate electrolyte to meet all of these requirements for future applications.

The polymer electrolytes mostly conduct via movement of protons [54], hydroxide ions [55,56], lithium ions [57], and ionic species in ionic liquids [58-62]. Based on the conduction mechanism, proton and lithium ion conducting polymer electrolytes are the most popular electrolytes. Lithium ion conducting polymer electrolytes are extremely moisture sensitive and thus need an oxygen free environment, which require special laboratory conditions. Proton conducting polymer electrolytes have the highest ionic conductivity among all polymer electrolytes and can be utilized under

ambient conditions but suffer from their narrower voltage window. Depending on the nature of the ionic conductor, proton conducting polymer electrolytes can be further classified into different types as shown in Fig. 2.4.

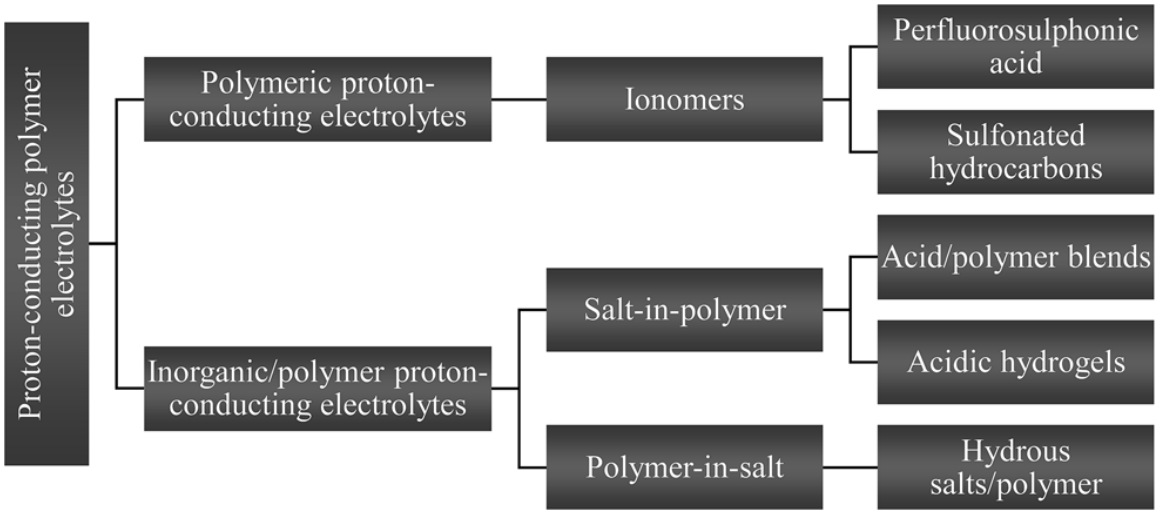

Figure 2.4 Categories of proton-conducting polymer electrolytes depending on the type of proton conductor [41].

A limited number of solid state systems have been studied with polymer/gel electrolytes, such as poly (ethylene oxide) (PEO), Poly(vinyl chloride) (PVC) [63], Poly(vinylidene fluoride) (PVF), as well as poly(methyl methacrylate) PMMA based electrolytes [64]. Yoon et al. [65] proved that Lithium phosphorous oxy-nitride (LiPON) electrolyte is also suitable for solid-state supercapacitors based on RuO_2 electrodes. Park et al. [66] fabricated an all solid-state supercapacitor by using a Nafion membrane and an ionomer, which is commonly used in fuel cells. LiPON is always fabricated by sputtering, which is not suitable to fill in a 3D interdigitated spacing. Sung et al. [67] reported a solid state electrolyte for polypyrrole (PPy) based planar micro supercapacitor, which is Polyvinyl Alcohol (PVA) based gel PVA/ H_3PO_4.

The most fundamental requirement of the electrolyte is that it contains mobile ions. This means that (aside from exotic materials such as ionic liquids) the electrolyte must consist of a solvent with an ionic compound (salt) dissolved in it. The most commonly used salts are lithium salts including $LiClO_4$, LiBF , LiPF , LiAsF , $Li(CF_3SO_3)$ (LiTFS), $LiN(CF_3SO_3)$ (LiTFSI), and $LiC(CF_3SO_3)$ that can readily be dissolved in high molecular weight polyether hosts such as PEO and PPO [67]. However, reactions can occur in Li/MnO_2 cells due to the reaction of lithium with MnO_2.

2.6 2D design vs. 3D design

In recent years it has been realized that performance of supercapacitors and batteries can be enhanced by reconfiguring the active materials currently used in 2D configuration into 3D architecture. The use of 2D design reduces the costs for mass production of devices by building up active materials on top of one another. However, the electrochemical cells with 2D structures are limited in the amount of energy that they can store or the amount of power that they deliver per unit area, volume or mass. There is always a trade-off between achieving high energy density or high power density. In contrast, 3D architecture based on complex non-planar configuration of electrode materials can increase the power and energy density of cells within the geometric footprint of the device. In particular, small devices cannot spare the square footage necessary for a thin-film 2D battery or electrochemical capacitor to provide the energy sufficient for the anticipated demands on the device. The 3D design of electrodes is necessary to decrease the transport of ions between the electrodes and at the same time increase the energy density. In recent research, Long et al. [68] gave an approximate

calculation based on the comparison of a thin film 2D battery that consists of a cathode and an anode with a surface area of 1cm^2 and thickness of 23.5 μ m, separated by a 5-μ m-thick electrolyte and total volume of 0.0055 cm^3. The 3D structure with the same volume and constructed from a 5-μm-radius cathode and anode array that are separated by 10 μm, the 3D battery contains only 39% of the energy capacity of the thin film battery.

There are several advantages of the 3D design, which are not revealed in these calculations. For the same areal footprint, the 3-D design with L=500 μm has a capacity that is **350%** larger than the 2-D design. In order to determine advantages of 3D design, the conventional 2D parallel-plate design and the 3D interdigitated cell can be considered, as shown in Fig. 2.2. The capacity of the 3D design can be increased by increasing the height of the posts (L) without sacrificing the small footprint. The 3D structure of Fig. 2.5 is achievable by several MEMS fabrication methods. For example, If we assume L to be 200 μm, the calculated surface area of the anode and cathode would be ~7.5 cm^2 each. If we increase L to 500 μm the surface area of anode and cathode would be ~19.5 cm^2 each. This cell consists of a total of 62500 anodes and cathodes and has a total of ~39 cm^2 active materials. If L becomes large we can assume that the ohmic resistance of the electrodes becomes sufficiently large to offset the advantages of increased areal capacity. However, as Long et al pointed out the optimized value for L depends on the electronic conductivity of the materials and ionic conductivity of the electrodes and electrolyte [68].

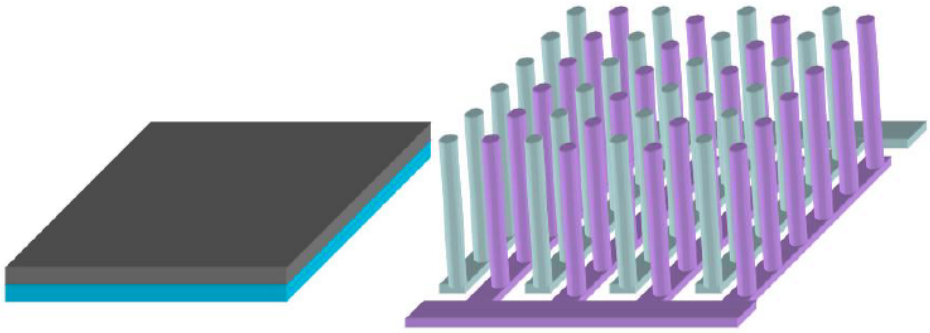

Figure 2.5 Schematic views of a 2D (a) and 3D (b) electrode design [7].

2.7 Three Dimensional Microsupercapacitors

Supercapacitors as high power density devices are well suited to replace with batteries and energy harvesting devices that are used for micro-systems, provided we can increase their energy densities. Relatively low power density is a big limitation for micro-batteries, as well as the short shelf life and lifetime also limits their application in permanent devices where battery replacement is impossible or impractical. Supercapacitors, with substantially higher power densities, longer cycle lifetimes and faster charge/discharge capabilities, rise as an alternative in miniaturized power supply fields. Although several potential applications are available for micro-supercapacitors, very few references in literature can be found. Sung et al. [69] have fabricated all-solid-state microsupercapacitors by using different techniques such as electrochemical polymerization, photolithography, and solution casting. They prepared the microsupercapacitor by electrochemical deposition of polypyrrole (PPy) on interdigitated gold microelectrode arrays. They only achieved the specific capacitance of 2mF.cm^{-2} from their work.

Sun et al. [70] reported on-chip 3D electrodes by reactive ion etching of Si substrate followed by electroless plating of Ni current collector and electrodeposition of

polypyrrole. Later, Sun developed their design and fabricated a full micro-supercapacitor cell. They reported a specific capacitance of 30 $mF.cm^{-2}$ at the current density of 1 $mA.cm^{-2}$ for a single electrode of their fabricated device. Y Jiang fabricated a double layer supercapacitor using vertically aligned carbon nanotube forests around 80 μm in height on silicon wafer [71], which has capacitance of 428 $\mu F.cm^{-2}$ and power density of 0.28 $mW.cm^{-2}$. Recently, Shen et al. [72] reported an on-chip micro-supercapacitor with 3D electrodes of activated carbon. The device was fabricated by injection of mixture of polymeric binder and activated carbon in silicon chip, which served as template. Pre-fabricated channel on a silicon chip were fabricated by etching silicon wafer by ICP (inductively coupled plasma), then the silicon walls between the electrodes were removed by a second ICP step. The electrode with a 3D interdigitated design was between 50 to 70 μm thick. They reported a specific capacitance of 90.5 $mF.cm^{-2}$ and power density of 5105 $mW.cm^{-2}$.

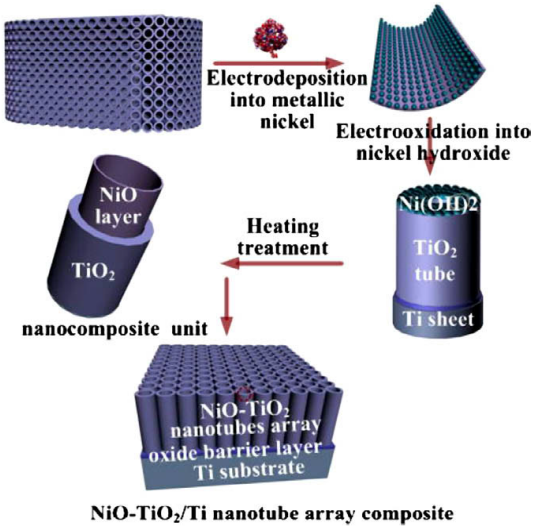

Figure 2.6. A diagram of preparation of $NiO–TiO_2$/Ti nanotube composites [51].

Y. Xie reported a NiO electrode for supercapacitor as shown in Fig. 2.6, which was deposited on the inside walls of anodically oxidized TiO_2 nanotubes [73]. Although the CV (cyclic voltammetry) curve for the electrode is not the ideal rectangular shape, they reported a specific capacitance of about 40-70 $mF.cm^{-2}$ under different testing conditions.

W. Rubloff and S. B. Lee fabricated a metal-insulator-metal electrostatic capacitor as shown in Fig 2.7 [74]. Atomic layer deposition (ALD) [75] was used for the conformal deposition of dielectric layer Al_2O_3 of few nanometers thickness. They achieved the specific capacitance of 102 $\mu F.cm^{-2}$. The supercapacitor can operate at high temperature because it is electrolyte free.

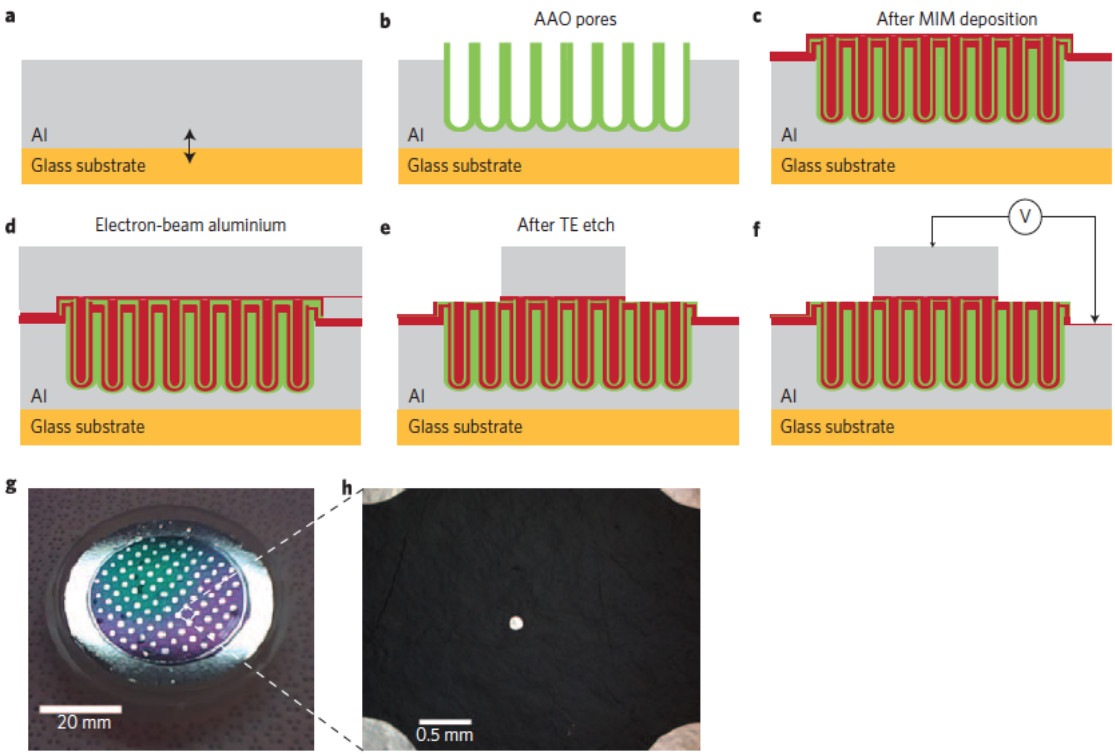

Figure 2.7. Fabrication process flow for electrostatic supercapacitors [53].

Chmiola et al. [76] developed microsupercapacitors based on monolithic carbide-derived carbon (CDC) interdigitated electrodes in 2010. The electrodes were fabricated by selective etching of monolithic CDC film using gold electrode both as a mask for current collector and etching. Heon et al. [77] later improved the process and developed their design. Their supercapacitors showed high volumetric capacitance of 180 $F.cm^{-3}$ at low scan rates of 20 $mV.s^{-1}$, however the capacitance dropped to almost half of its initial value by increasing the scan rate to 500 $mV.s^{-1}$, highlighting the poor rate handling capability of these micro-supercapacitors. Pech et al. [78] fabricated a micro-supercapacitor based on onion-like carbon (OLCs). The OLC based micro-supercapacitors are particularly important as they offer very high power handling capability with a very low resistance. The main drawback of OLC based micro-supercapacitors is their low specific capacitance (1.7 $mF.cm^{-2}$) and their high temperature processing requirements (~1900 °C).

Pech et al. [79] also reported on fabrication of on-chip micro-supercapacitors by ink-jet printing of activated carbon on micro-patterned gold electrodes. The device showed specific a low capacitance of 0.4 $mF.cm^{-2}$ however, due to the use of polymeric binders and limited ion transfer in the porous network of the electrode materials, AC micro-supercapacitors show relatively poor frequency response. Lim et al. [80] reported on the earliest work on thin film supercapacitors, a microsupercapacitor based on two thin films of pseudo-capacitive material and solid electrolyte. Ruthenium oxide (RuO_2) was used as pseudo-capacitive material in their work. The microsupercapacitor cell delivered a volumetric capacitance of 40 $mF.cm^{-3}$, however, the capacitance dropped to almost half of its initial value after only 600 cycles. The relatively short lifetime of thin

film supercapacitors based on pseudo-capacitive materials is their main drawback that limits their application.

There are very few reports in the literature about micro-supercapacitors based on metal oxide pseudo-capacitive materials. Xue et al. [81] fabricated micro-supercapacitors through micro-fluidic etching of films of manganese oxide nanofiber arrays. They achieved a specific capacitance of about 345 $F.g^{-1}$ at a very low discharge rate of 0.55 $mA.cm^{-2}$, but the device showed very high resistance at higher discharge rates. Gao et al. [82] reported a microsupercapacitor fabricated with interdigitated electrode design and hydrated graphene oxide (GO) as the electrolyte and separator. While the fabrication method is promising, the electrodes were fabricated in millimeter scales with the maximum capacitance of only 0.49 $mF.cm^{-2}$ for an in-plane design of electrodes. Table 2.2 shows results from some of the typical microsupercapacitors that have been reported recent years.

Table 2.2 The characteristics and properties of some of the reported micro-supercapacitors [8].

Electrode material	Electrolyte	Potential range (V)	Specific capacitance ($mFcm^{-2}$)	Frequency response and rate capability
AC	1 M Et_4NBF_4 in PC	0-2.5	2.1	-Capacitance quickly drops at frequencies more than 10 mHz -poor frequency response
CDC	1.5 M $TEABF_4$	-1-1	180 Fcm^{-3} (volumetric capacitance of single electrode)	-Capacitance drops to half of its initial value at scan rates as low as 500 mVs^{-1} -poor rate capability
CNT	BMIM/ BF_4	-0.5-0.5	0.428	N/A
Gr	PVA/ H_3PO_4	0-1	<0.4	-The device was tested up to the scan rate of 0.01 Vs^{-1}
OLC	1 M Et_4NBF_4 in PC	0-3	1.7 at 1 Vs^{-1}	-RC time constant of 26 ms indicating good frequency response.
AC	1 M Et_4NBF_4 in PC	0-3	11.6 at 500 mVs^{-1}	-RC time constant of 700 ms. -Capacitance drops with increase in scan rate
Gr	PVA/ H_2SO_4	0-1	7.6	Capacitance drops by about 75% scan rate of 4 Vs^{-1}
Ppy	PVA/ H_3PO_4	-0.25-0.25	-	Poor capacitive performance at high scan rate
MnO_2	1 M Na2SO4	-0.2-1	338 Fg^{-1} at 50 mVs^{-1}	The capacitance quickly drops at higher scan rates

Batteries are also promising devices for energy storage in miniaturized systems such as MEMS, sensors, and mobile devices. To fabricate micro-batteries, thin film techniques are the main directions that are being pursued both by academia and industry. A thin film microbattery is a device made up of thin layers of cathode, solid electrolyte and anode. In recent years, different kinds of cathodes, anodes and electrolyte materials have been developed for thin film batteries. Table 2.3 shows results from some of the typical thin film batteries that have been reported in recent years [4]. The main drawback of thin film micro-batteries is their relatively low energy density. To increase the energy

Table 2.3: Typical thin film batteries [4].

Anode	Cathode	Electrolyte	Voltage (V)	Current (μAcm^{-2})	Capacity
LiV_2O_5	V_2O_5	LiPON	3.5	10	6 $\mu Ahcm^{-2}$
V_2O_5	$LiMn_2O_4$	LiPON	3.5-1	2	18 $\mu Ahcm^{-2}$
Li	$LiCoO_2$	LiPON	4.2-2	50-400	35 $\mu Ahcm^{-2}$
Cu	$LiCoO_2$	LiPON	4.2-3.5	1-5	130 $\mu Ahcm^{-2}$
Li	$LiMn_2O_4$	LiPON	4-5.3	10	10-30 $\mu Ahcm^{-2}$
SiSnON	$LiCoO_2$	LiPON	2.7-4.2	5000	340-450 mAg^{-1}

density of thin film micro-batteries, most of the researchers are focused on developing new materials for the cathode, anode and electrolyte. On the other hand, as it was discussed in the previous section, the most promising approach for increasing the energy density is designing three dimensional architectures for micro-batteries.

In recent years several techniques and different concepts have been reported for developing micro-batteries with 3D architecture. Micro-molding is one of the techniques that have been used to fabricate 3D structures for microbatteries. The mold is prepared by high-aspect-ratio etching techniques and the electrode fabrication process depends on the specific battery system. The main idea of this approach is that a variety of different electrode materials can be fabricated into post-electrode-array structures. Chamran et al [83] used this technique to fabricate interdigitated electrode array post structures of zinc and nickel hydroxide. The assembled battery was tested in 6 M KOH and the capacity of 2.5 $\mu Ah.cm^{-2}$ was achieved.

One other important approach to fabricate the 3D structure is the development of a micro-channel plate or MCP. Nathan [84], from Tel Aviv University, fabricated a 3D micro-battery on both silicon and glass substrates. Their 3D micro batteries have a sandwich-like structure of conformal thin-film electrodes, electrolyte and current collectors. The films are consecutively deposited using wet chemistry on all available surfaces of the substrate (silicon or a glass microchannel plate or "MCP"), which consists of thousands of holes per unit surface area. Due to high-aspect ratio holes per square cm, this 3D structure provides one order of magnitude higher surface area per footprint compared to the original 2D electrode. The full 3-D cell consists of a nickel (Ni) cathode current collector, a nominally MoOySz (amorphous form of MoS_2-molybdenum oxosulfide) cathode, a hybrid polymer electrolyte (HPE) and a lithiated graphite anode that also serves as the anode current collector, as seen in Figure 2.8. A 3D cell with a roughly 1 μm thick cathode exhibited the capacity of 2mAh.cm^{-2}, about 33 times higher than similarly built planar 2D cells with the same footprint and cathode thickness.

Golodnitsky [85] used the same fabrication concept and by depositing new composite cathode materials improved the capacity to 3.5 mAh.cm^{-2}, 25 to 35 times that of a planar 2D thin-film cell with the same footprint and about twice that of semi-3D cells. Recently, several researches have been focus on fabricating 3D nanoelectrodes for lithium ion batteries. Cheah et al [86] fabricated a nanostructured 3D battery, which consists of aluminium nanorods as the current collector and a 17 nm uniform layer of TiO_2 as anode material. The electrode has 11.2 μAhcm^{-2} capacitance, which is 10 times higher than that of the corresponding 2D electrode.

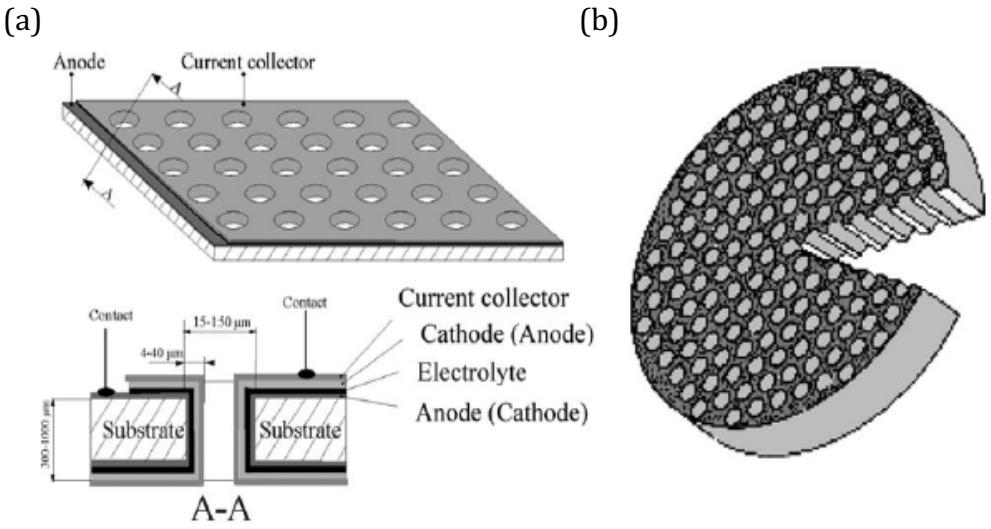

Figure 2.8 (a) Schematic structure of a 3-D thin-film battery on a perforated silicon substrate; (b) Schematic structure of an MCP substrate [44].

Although batteries have several advantages over supercapacitors, batteries have a limited number of charge/discharge cycles and take time to charge and discharge because the process involves chemical reactions with non-instantaneous rates. These chemical reactions have freeloading thermal release that causes the battery to heat up extremely. Batteries have a limited life cycle with a degrading performance and acidic batteries are extremely hazardous to the environment. They work well as a continuous source of low power, however, they cannot efficiently handle peak power demands or recapture energy in today's applications because they discharge and recharge slowly. Batteries do not like be held fully charged and they require maintenance or replacement after some time. In general, batteries have several drawbacks that limit their application where a battery is really needed [7].

2.8 Solid-State Supercapacitors

The conventional supercapacitors consist of two advanced electrodes with insulating separator film between them in organic or aqueous electrolyte. However, they suffer two main drawbacks for practical applications due to the liquid electrolytes. Firstly, the electrolyte leakage may lead to the decrease in specific capacitance, reduction of electrochemical performance, and hazardous to the environment. Secondly, the supercapacitors are packaged in rigid container which are pressure sensitive and lack flexibility. Therefore, tremendous effort has been made to replace liquid electrolytes with solid electrolytes for the next generation solid-state supercapacitors. These supercapacitors, prepared by the incorporation of solid electrolyte, offer to provide safe operation for flexible, printable, wearable, lightweight, and high performance devices applications [87,88]. Over the past few years, efforts have been dedicated to developing all-solid-state supercapacitors including fabrics, woven cotton, textile, and paper [89-92]. At the same time, thin or free standing electrodes including carbon nanotubes (CNT), reduced graphene oxide, graphene sheets, metal oxide/carbon composite, and conducting polymer/carbon nanotubes composites have been investigated for solid-state supercapacitors.

Proton-conducting polymer electrolytes are gaining interest since they have the highest ionic conductivity of all polymer electrolytes and most of the pseudo-capacitive electrodes require protons for their Faradaic redox reactions. Proton-conducting polymer electrolytes have not been discussed extensively, and they are not widely used for solid-state supercapacitors to date. Commonly, an effective way to make polymer electrolyte is

by adding a polymer, such as polyvinyl alcohol (PVA), polyethylene glycol (PEO) or polyvinylpyrrolidone (PVP), into a proton conducting aqueous solution.

PVA is a polar polymer with high dielectric strength and dopant-dependent electrical and optical properties. In the development of solid polymer electrolyte system, the electrolyte part consists of polyvinyl alcohol-containing silica gels doped with $HClO_4$, H_2SO_4, or H_3PO_4 [93-96]. Phosphoric acid (H_3PO_4) has been chosen since it shows higher conductivity than other materials. The PVA/ H_3PO_4 solid-state electrolyte has been selected for the solid-state supercapacitor research in this work. The PVA/ H_3PO_4 solid electrolyte has been reported to show good reversibility and electrochemical stability up to 1.6 V. Figure 2.9 shows schematic of polymer electrolyte based supercapacitors cell assembled in different configurations.

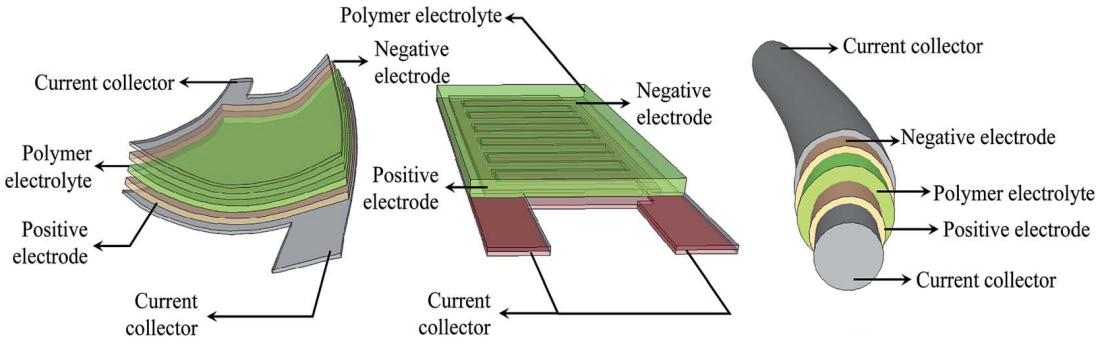

Figure 2.9 Schematic of polymer electrolyte based supercapacitors in different configurations (left) sandwich, (middle) interdigitated finger cell, and coaxial fiber cell (right) [41].

CHAPTER III

DEVELOPMENT OF PLANAR MACRO SUPERCAPACITORS

This chapter highlights the development of planar CNT/MnO_2 supercapacitors. Initially, CNT/MnO_2 electrodes were separately fabricated on silicon and flexible graphite substrates for fundamental study as supercapacitor electrodes. The findings were then utilized to develop double-sided CNT/MnO_2 electrodes on graphite foils for application in multi-layer supercapacitor prototype cells.

CNT/MnO_2 electrodes were fabricated on silicon substrates using hot filament chemical vapor deposition (HF-CVD) to grow carbon nanotubes (CNTs). Electrochemical deposition technique was then used to deposit manganese dioxide (MnO_2) directly on the CNTs. Material analysis and characterization were performed using scanning electron microscope (SEM) and Raman spectroscopy. Charge storage performance was evaluated by electrochemical techniques such as cyclic voltammetry (CV) and galvanostatic charge/discharge measurement.

In addition, supercapacitors using conductive and flexible graphite substrates were also fabricated. CNTs were synthesized on single side as well as both sides of the graphite substrate in order to develop single-sided and double-sided electrodes using thermal chemical vapor deposition (T-CVD) technique. Material analysis was also performed using scanning electron microscope (SEM) and Raman spectroscopy.

Finally, double-sided electrodes were used to fabricate multi-layer supercapacitor prototype cells. The electrochemical characterization of supercapacitor in organic electrolyte, including cyclic voltammetry (CV), galvanostatic charge–discharge, and

electrochemical impedance spectrometry (EIS), were investigated. Figure 3.1 presents the flow chart of the experimental process followed in this work.

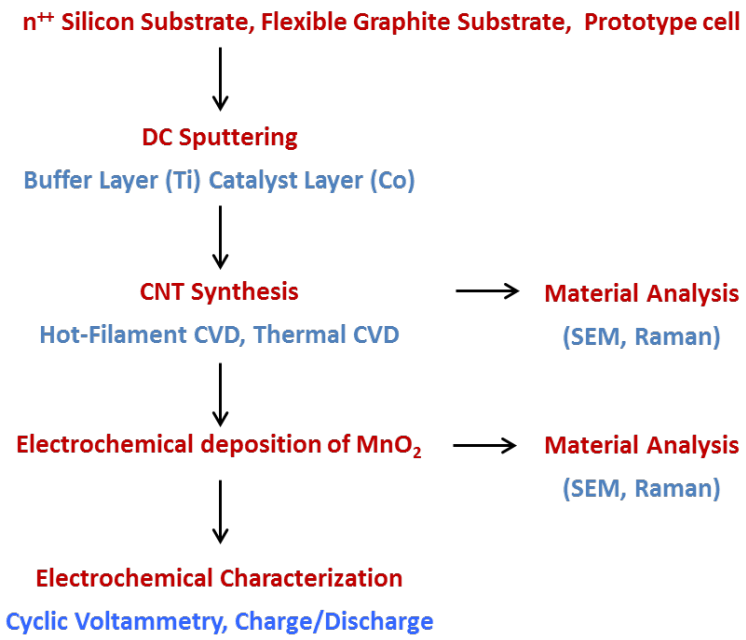

Figure 3.1 Flow chart of the experimental process followed in this work.

3.1 Fabrication and Characterization of CNT/MnO_2 Supercapacitor Electrodes on Silicon Substrate

3.1.1 Synthesis of Vertically Aligned CNTs on Silicon Substrate – Method, Results and Discussion

This section provides details on the synthesis and characterization of CNTs under different growth conditions, including SEM analysis. In addition, summary charts for CNTs grown under different conditions have also been included.

Since the discovered of carbon nanotubes by Iijima in 1991, there have been a variety of techniques developed for the synthesis of CNT. The three most common techniques for producing high quality CNTs include electric arc discharge, laser ablation,

and chemical vapor deposition (CVD) [97]. However, both the arc discharge and laser ablation techniques are limited to volume of samples in comparison to the size of the carbon source. The equipment requirements and large amount of energy consumed by these methods make them less popular for laboratory research. Research activities have been focused on the control of selective deposition and orientation of CNTs by CVD synthesis using various gas sources, different substrates, and different catalysts [98].

Multiple experiments/trials were performed to examine the role of different process parameters on the growth of vertically aligned CNTs. For all sets of experiments, a hot filament (HF) CVD system that was built in-house was used to grow CNTs. Highly doped n++ silicon substrates with resistivity of 0.0035 Ω-cm and 2.5 cm x 1.5 cm in size were used for growing CNTs. The silicon substrates were first coated with a thin layer (~15nm thick) of titanium (Ti) followed by a thin layer (~5nm thick) of cobalt (Co), using DC magnetron sputtering under a vacuum of ~$5x10^{-5}$ Torr [99]. The Ti acts as a diffusion barrier layer for the catalysts to prevent the formation of silicides at high temperatures [100].

The substrates were loaded into the HFCVD system for growth of CNTs, per the processing parameters described in Table 3.1. After loading the sample into the HFCVD system, the reactor chamber is evacuated to a base pressure of ~ 0.2 Torr, and raised to the final pressure with the predetermined hydrogen gas flow rate. The substrate temperature was gradually increased to 700 ^{0}C at this pressure. The samples from all the groups were subject to same working temperature (~700 ^{0}C). Hydrogen (H_2), methane (CH_4), and ammonia (NH_3) gases were used to grow vertically aligned CNTs in all the trials in both the sets of experiments

The ammonia gas used in this work consists of 100ppm of NH_3 diluted in Nitrogen gas. The role of ammonia has been investigated both in the pretreatment phase and growth of CNT phase. During the growth phase ammonia is believed to generate atomic hydrogen species which provide preferential etching of amorphous carbon generated during the CNT synthesis. Hydrogen was also found to play an important role in this experiment by increasing the catalytic activity on the surface of CNT and helping reduce amorphous carbon content on the CNTs. Consequently, ammonia and hydrogen are believed to be essential to the growth of CNTs, although the reason responsible for the effect of ammonia in CNT growth has not been clearly known yet [4].

Table 3.1 Specific details of the synthesis parameters used to grow CNTs. The parameters include buffer/catalyst thickness, temperature (T), pressure (P), flow rates, pretreatment time, and growth time [4].

Experiment	Sample #	Catalyst Ti/Co			Flow Rates			Pretreatment time	Growth time
		nm	T	P	H_2	CH_4	NH_3	(min)	CH_4 (min)
			^0C	Torr	Sccm	Sccm	Sccm	H_2/ NH_3	
1	A1	15/5	700	15	75	25	75	40/5	2
	A2	15/5	700	15	75	25	75	40/5	4
	A4	15/5	700	15	75	25	75	40/5	6
	A5	15/5	700	15	75	25	75	40/5	8
	A6	15/5	700	15	75	25	75	40/5	10
2	B1	15/5	700	15	75	25	100	40/5	2
	B2	15/5	700	15	75	25	100	40/5	4
	B3	15/5	700	15	75	25	100	40/5	6
	B4	15/5	700	15	75	25	100	40/5	8
	B5	15/5	700	15	75	25	100	40/5	10

Figure 3.2 shows the SEM cross sectional micrographs of the carbon nanotubes on the highly conductive silicon substrates. The flow rates were selected for NH_3 because they yielded vertical aligned CNTs. The heights of the carbon nanotubes changed from ~2 μm to ~50 μm when the growth time (with CH_4 flow) was increased. The variation of the CNT height by adjusting the growth time and the effect of NH_3 used in the input gas mixture were plotted as seen in the graph in figure 3.3. In general, for the same growth time, the CNT height was observed to be higher with 75 sccm of NH_3 as compared to that recorded for 100sccm. This observation suggests that even though the NH_3 is important for CNT growth, but there is a limit beyond which the benefit decreases.

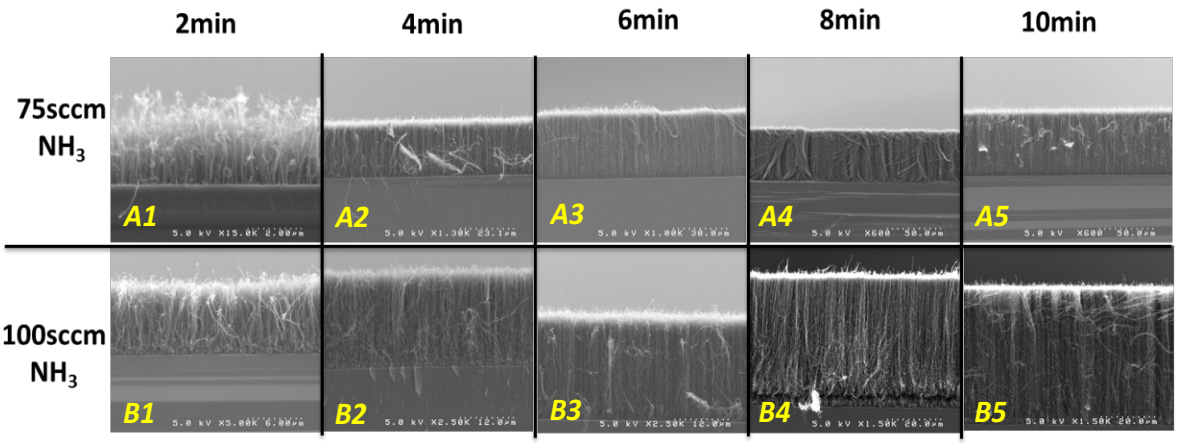

Figure 3.2 SEM images of CNTs with different ammonia flow rates and growth time CNT (min).

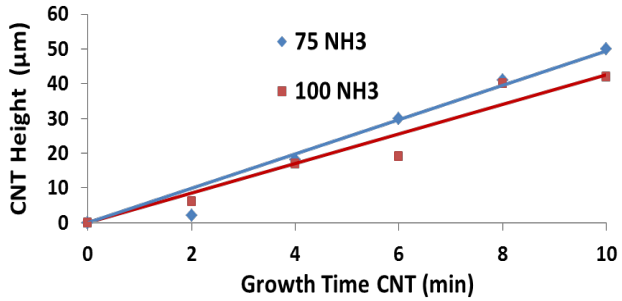

Figure 3.3 CNT height (µm) versus CNT growth time (min).

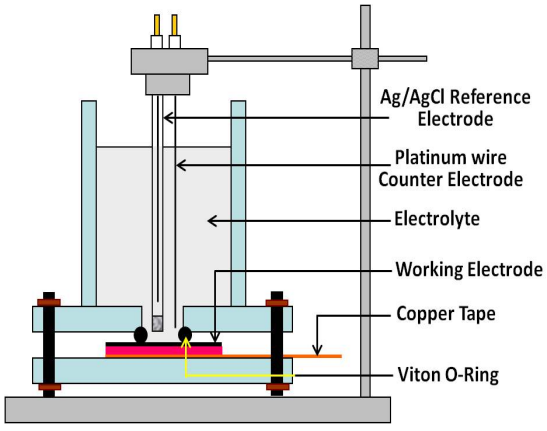

Figure 3.4 Test setup for electrochemical deposition of MnO_2 and electrochemical characterization.

3.1.2 Deposition of MnO_2 on CNTs – Method, Results and Discussion

In the last decade, manganese dioxide has attracted considerable attention in the supercapacitors due to its low-cost, environment-friendly, and good electrochemical performance. Manganese (IV) oxide is the inorganic compound having the chemical formula MnO_2. A number of deposition methods have been used for the deposition of MnO_2 include sol-gel method [101], chemical bath deposition [102], anodic oxidation of Mn^{2+} [103], spray pyrolysis [104], and electrochemical deposition [105]. Since electrochemical deposition technique is relatively clean, provides excellent thickness control, is reproducible and does not require expensive infrastructure, it was used for manganese dioxide (MnO_2) deposition in this research.

Deposition of manganese dioxide (MnO_2) on CNTs was achieved electrochemically by direct reduction of potassium permanganate ($KMnO_4$) solution in de-ionized water (18MΩ-cm). $KMnO_4$ is a strong oxidizing agent, however, it can be electrochemically reduced directly on the conducting substrate by the following reaction.

$$MnO_4^- + 2H_2O + 3e^- \rightarrow MnO_2 + 4OH^-$$

Cyclic voltammetry was used at room temperature to electrochemically deposit MnO_2 thin-films directly on a CNT network grown on a highly doped silicon substrate. The CV experiments were performed by using a flat cell in a 3 electrode configuration shown in figure 3.4. The CNT/Si was the working electrode, Ag/AgCl (3M KCl) reference electrode and a platinum wire as the counter electrode. CVs were recorded in 0.1M KCl as the electrolyte at different scan rates (10mV/s, 50mV/s, 100mV/s, 200mV/s

and 500mV/s) before and after any MnO_2 deposition step. The deposition parameters are detailed in following tables.

To find the optimum parameters for electrochemical deposition of MnO_2, the effects of various deposition parameters such as scan rate, wider deposition potential, the time interval during MnO_2 deposition, and height of CNTs were investigated. The initial set of parameters used are listed in table 3.2, part 1.

Table 3.2 Part 1- Deposition parameters for MnO_2.

	[$KMnO_4$](mM)	**Scan Rate (mV/s)**	**Scan Window**	**# of cycles**	**# of steps**	**Interval between cycles**
1	10	10	0V to +1V	15	3	0s
				10	1	0s
2	10	10	0V to -1V	10	2	0s

Electrochemical deposition of MnO_2 from 10mM $KMnO_4$ at 10mV/s and two different scan limits, 0V to +1V and 0V to -1V were performed. For sample 1, the MnO_2 deposition step was performed between 0 V to +1 V, 4 times for a total of 25 cycles [3 sets of 5 cycles each and 1 set of 10 cycles] and after each round of deposition, CV measurements in KCl were taken. Based on the CVs recorded at 100mV/s, there is a gradual increase in the capacitive currents until 10 cycles of MnO_2 deposition, where a 3.2x improvement in capacitance was observed, after which it saturates and further deposition only worsens the capacitive behavior. The CVs recorded before MnO_2 deposition, i.e., using only CNTs, after 5, 10, 15 and 25 cycles at 100mV/s have been overlaid and can be seen in figure 3.5. The SEM micrographs of the MnO_2/CNT supercapacitor can also be seen in figure 3.5. There is formation of multiple sections of CNTs finely coated with MnO_2 film.

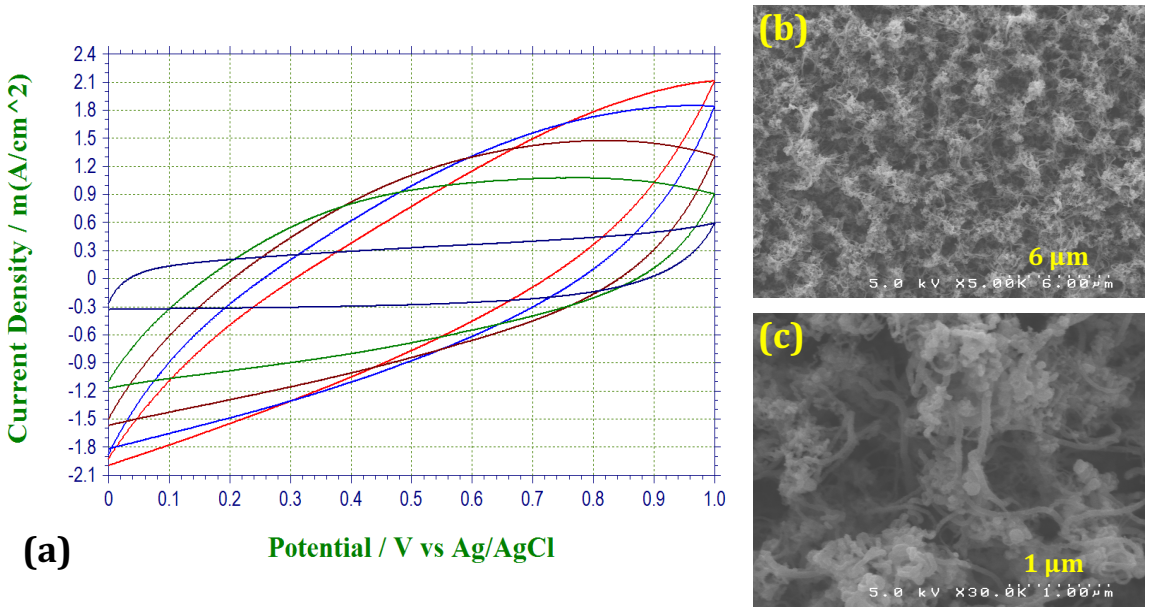

Figure 3.5 CVs recorded at 100mV/s with MnO_2 deposition on sample 1 and the corresponding enhancement in capacitance- after 25 cycles (RED) (2.5x), 15 cycles (BLUE) (3.1x), 10 cycles (BROWN) (3.2x), 5 cycles (GREEN) (2.7x) and without MnO_2 (BLUE). SEM pictures after 25 cycles of MnO_2 deposition on sample 1.

For sample 2, the MnO_2 deposition step was performed between -1 V to 0 V, 2 times for a total of 10 cycles [2 sets of 5 cycles] and after each round of deposition, CV measurements in KCl were taken. Sample 2 also showed an increase in capacitive currents after the first 5 cycles of MnO_2 deposition, however, after another 5 cycles of deposition, the capacitance fell drastically, about half of what was observed previously. The CVs recorded before and after MnO_2 deposition have been overlaid and can be seen in figure 3.6. This behavior can only be explained by the presence of a thick MnO_2 layer, which blocks free movement or diffusion of the K^+ ions. SEM micrographs seen in figure 3.6 confirm this conclusion. There is a 3-5µm thick layer of MnO_2 on the top which itself comprises of multiple layers formed during the 10 cycles of deposition. The MnO_2 film consists of small clusters 50-100 nm in sizes, seen in the top-view, which have coalesced to form a complete film. Cyclic voltammetry in the negative potential region (0V to -1V)

has a much higher deposition rate than that observed in the positive potential region (0V to +1V).

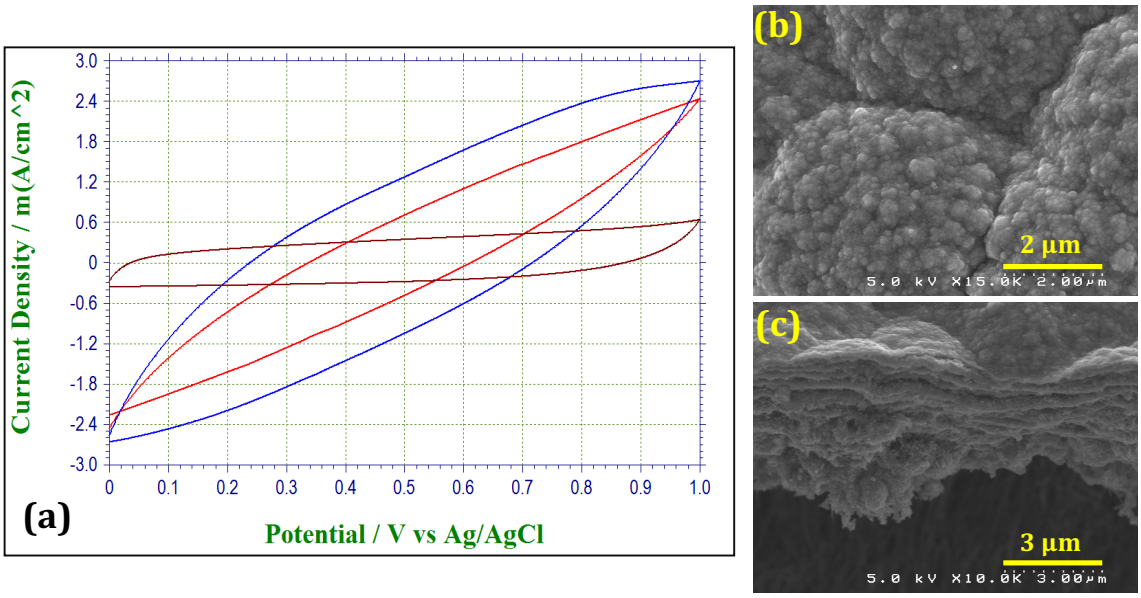

Figure 3.6 (a) CVs recorded at 100mV/s before and after MnO_2 deposition on sample 2 and the corresponding enhancement in capacitance - after 10 cycles (RED) (1.9x), 5 cycles (BLUE) (3.7x) and without MnO_2 (BROWN). (b) and (c) SEM pictures after 10 cycles of MnO_2 deposition on sample 2.

As the next step, sample 3, the scan rate was increased to 100mV/s for the scan window of 0V to -1V while keeping the $KMnO_4$ concentration constant. Electrochemical deposition of MnO_2 from 10mM $KMnO_4$ at 100mV/s was done 4 times in steps of 10 cycles each for a total of 40 cycles. The deposition parameters have been summarized in table 3.2- part 2. The CVs recorded at 100mV/s before and after 10, 20, 30 and 40 cycles of deposition were overlaid and can be seen in figure 3.7. Based on the CVs recorded at 100mV/s, there is a gradual increase in the capacitive currents until 30 cycles of MnO_2 deposition where we observe a 5.6x improvement in capacitance and further deposition only worsens the capacitive behavior. The microstructure of the MnO_2 deposited on sample 3 after 40 cycles can be seen in figure 3.7. We observe a thin yet continuous

layer of MnO_2 near the top of the surface. However, underneath this top layer, at the tips of the CNTs, bulbous/spherical yet porous growth of MnO_2 exists. This porous network is more suited for achieving enhanced capacitance in the device. The formation of the spherical shape at the tips of the CNTs can be explained by the fact that the CNTs have very high aspect ratio resulting in enhanced fields that can increase the flux on the reactants yielding higher reaction kinetics. These results suggest that the MnO_2 deposition rate decreases as the scan rate is increased which provides a better control over the process and the tall, vertically aligned CNTs can limit MnO_2 deposition to the top section/portion only.

Table 3.2 Part 2- Deposition parameters for MnO_2 for sample 3.

	[$KMnO_4$](mM)	**Scan Rate (mV/s)**	**Scan Window**	**# of cycles**	**# of steps**	**Interval between cycles**
3	10	100	0V to -1V	40	10	0s

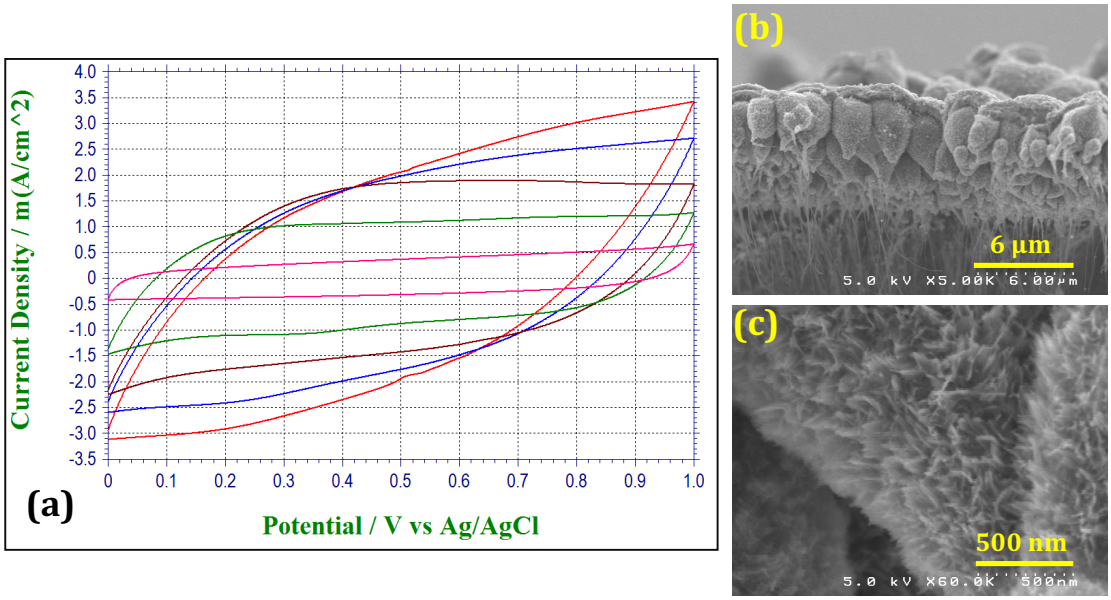

Figure 3.7 (a) CVs recorded at 100mV/s before and after MnO_2 deposition for sample 3 and the corresponding enhancement in capacitance - after 40 cycles (RED) (4.2x), 30 cycles (BLUE) (5.6x), 20 cycles (BROWN) (4.8x), 10 cycles (GREEN) (2.9x) and without MnO_2 (PINK). (b) and (c) SEM pictures after 40 cycles of MnO_2 deposition on sample 3.

In case of sample 4, the deposition potential window was widened to -1V to +1V while keeping the scan rate at 100mV/s, same as that for sample 3. The deposition parameters have been summarized in table 3.2- part 3. The CVs recorded at 100mV/s before and after 5, 15, 25 and 35 cycles of MnO_2 deposition have been overlaid and can be seen in figure 3.8. Based on the CVs recorded at 100mV/s, there is a gradual increase in the capacitive currents as the MnO_2 deposition progresses. This suggests that at the given MnO_2 thickness, the K^+ ions are still able to diffuse deeper into the porous MnO_2/CNT network to enhance the capacitance. CVs recorded after 10, 20 and 30 cycles of MnO_2 deposition have been omitted to reduce the congestion and make the curves more readable. As compared to the previous samples, much higher enhancements in capacitance have been observed for this sample, as much as 9.1x after 30 cycles. The SEM images, as seen in figure 3.8, show that the MnO_2 forms ball shaped clusters

growing preferentially near the top of the CNTs, rising vertically above. The top surface is still open and easily accessible by the K^+ ions in the electrolyte.

These results indicate that a wider deposition potential window of -1V to +1V provides a better control over the growth rate and the microstructure of MnO_2 due to the fact that we observed much higher improvements in capacitance.

Table 3.2 Part 3- Deposition parameters for MnO_2 for sample 4.

	[$KMnO_4$](mM)	**Scan Rate (mV/s)**	**Scan Window**	**# of cycles**	**# of steps**	**Interval between cycles**
4	10	100	-1V to +1V	35	5	0s

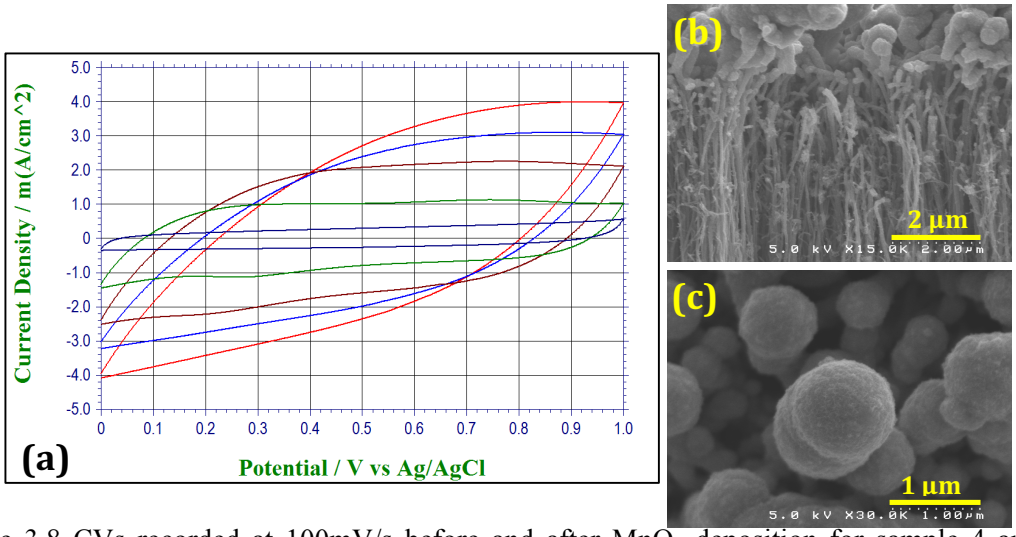

Figure 3.8 CVs recorded at 100mV/s before and after MnO_2 deposition for sample 4 and the corresponding enhancement in capacitance - after 35 cycles (RED) (9.1x), 25 cycles (BLUE) (7.9x), 15 cycles (BROWN) (6.7x), 5 cycles (GREEN) (3.3x) and without MnO_2 (BLUE). SEM pictures after 35 cycles of MnO_2 deposition on sample 4.

Table 3.2 Part 4- Deposition parameters for MnO_2 for sample 5.

	[$KMnO_4$](mM)	Scan Rate (mV/s)	Scan Window	# of cycles	# of steps	Interval between cycles
5	1	100	-1V to +1V	10	5	60s
				30	10	60s

In the next set of experiments, the deposition parameters were kept the same as that for sample 4 except for the $KMnO_4$ concentration which was reduced to 1mM from 10mM used in previous experiments. The deposition was carried out 2 times in sets of 5 cycles for a total of 10 cycles and thereafter 3 times in sets of 10 cycles for a total of 30 cycles. The deposition parameters have been summarized in table 3.2- part 4. The CVs recorded at 100mV/s recorded before and after 5, 10, 20, 30 and 40 cycles of deposition have been overlaid and can be seen in figure 3.9. Based on the CVs recorded at 100mV/s in 0.1M KCl, there is a small yet gradual increase in the capacitive currents as MnO_2 deposition progresses, with a maximum increase of 2.4x in capacitance after the 40

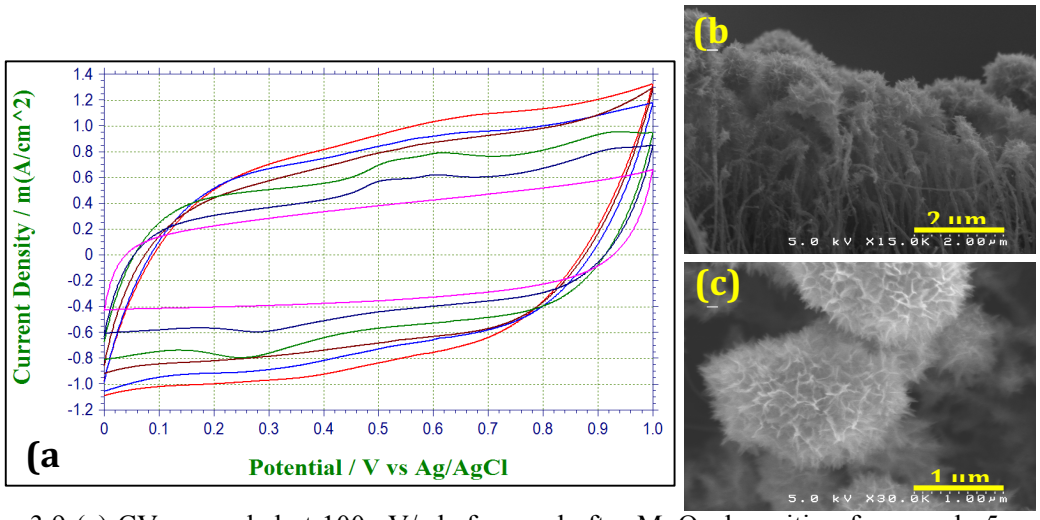

Figure 3.9 (a) CVs recorded at 100mV/s before and after MnO_2 deposition for sample 5 and the corresponding enhancement in capacitance - after 40 cycles (RED) (2.4x), 30 cycles (BLUE) (2.1x), 20 cycles (BROWN) (2.0x), 10 cycles (GREEN) (1.7x), 5 cycles (BLUE) (1.4x) and without MnO_2 (PINK). (b) and (c) SEM pictures after 35 cycles of MnO_2 deposition on sample 5.

cycles. The SEM images, as seen in figure 3.9, show that the MnO_2 forms porous ball shaped clusters growing preferentially near the top of the CNTs, somewhat similar to that observed in sample 4 but smaller in size. The top surface is still open and easily accessible by the K^+ ions in the electrolyte. These results clearly indicate that the rate of MnO_2 deposition is also dependent on the $KMnO_4$ solution concentration. Lower concentration may provide better control but at the cost of increase in the deposition time.

In the previous experiments, cross sectional analysis by SEM revealed that most of the MnO_2 was localized near the top of the CNTs. This meant that the heights of the tall, vertically aligned CNTs could not be used to our benefit in order to maximize the MnO_2 coverage and thereby the capacitance. Therefore, for the last set of experiments 2μm tall CNTs on silicon substrate was considered. The deposition parameters have been summarized in table 3.2- part 5. The concentration of $KMnO_4$ was increase to 10mM and the deposition was performed in 3 sets of 10 cycles with 60s intervals between each cycle, to allow for MnO_4^- concentration to reach equilibrium near the CNT surface.

The CVs recorded before and after 10, 20 and 30 cycles of MnO_2 deposition have been overlaid and can be seen in figure 3.10. Based on the CVs recorded at 100mV/s in 0.1M KCl, there is a huge increase in the capacitive currents as MnO_2 deposition progresses. A 63x improvement in capacitance is observed after 30 cycles of deposition, which highlights the contribution of MnO_2 and the effect of short CNT height that allows for enhanced MnO_2 deposition.

The SEM micrographs before and after MnO2 deposition can also be seen in figure 3.10. By using electrochemical reduction of $KMnO_4$ we are able to deposit MnO_2 on all the CNTs, from base to the tips. There is a thick deposit of MnO2 in the form of

clusters with very small grain size. The MnO_2/CNT network is still open enough to allow free movement of the electrolyte and thus we were able to utilize the high surface area of the CNTs and achieve very high enhancement in capacitance.

Table 3.2 Part 5- Deposition parameters for MnO_2 for sample 6.

	[$KMnO_4$](mM)	Scan Rate (mV/s)	Scan Window	# of cycles	# of steps	Interval between cycles
6	10	100	-1V to +1V	30	10	60s

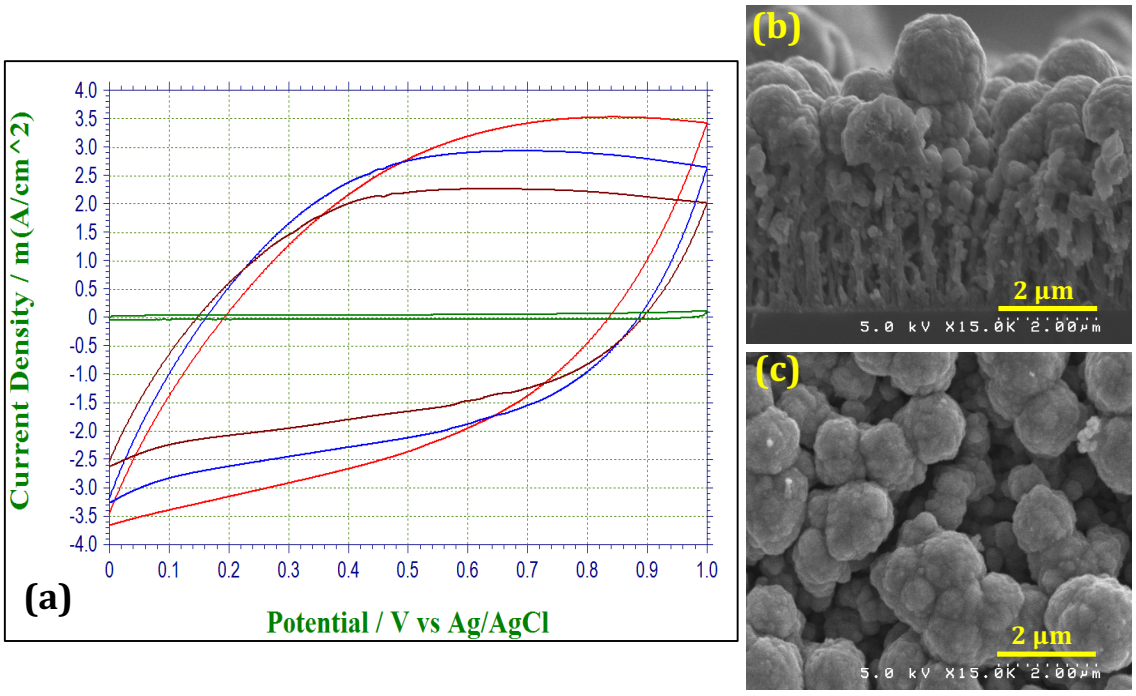

Figure 3.10 CVs recorded at 100mV/s before and after MnO_2 deposition for sample 6 and the corresponding enhancement in capacitance - after 30 cycles (RED) (63x), 20 cycles (BLUE) (60x), 10 cycles (BROWN) (47x) and without MnO_2 (GREEN). SEM pictures after 30 cycles of MnO_2 deposition on sample 6.

Based on the experiments performed on planar supercapacitors using electrochemically deposited MnO_2 on CNTs, the following conclusions can be reached at regarding the deposition process.

- In-situ deposition of MnO_2 on CNTs can be achieved by using cyclic voltammetry in a $KMnO_4$ solution.
- Cyclic voltammetry in the negative potential region (0V to -1V) has a much higher deposition rate than that observed in the positive potential region (0V to +1V).
- The deposition rate varies inversely with the scan rate used. Increasing the scan rate reduces the deposition rate thus providing better control.
- Increasing the potential scan limits at the same scan rate yields a better coverage of MnO_2 on the CNTs as inferred from the greater enhancement in the capacitive currents.
- Introducing a wait-period (60s) between successive CV scans during the deposition process may increase the proportion of CNTs covered. The deposition rate however is less than that with no wait-period.
- The deposition rate is directly proportional to the concentration of the $KMnO_4$ solution used. A lower concentration can be used to achieve better control at the same scan rate.
- In a planar electrode configuration, tall CNTs are not advantageous. Shorter CNTs allow for excellent MnO_2 coverage and thereby a very high enhancement in the capacitance. Optimum parameters for MnO_2 deposition can be tabulated as follows:

[$KMnO_4$](mM)	**Scan Rate (mV/s)**	**Scan Window**	**# of cycles**	**# of steps**	**Interval between cycles**
10	100	-1V to +1V	≤ 30	10	$\geq$ 60s

3.2 Fabrication and Characterization of CNT/MnO_2 Supercapacitor Electrodes on Flexible Graphite Substrate

3.2.1 Synthesis of CNTs on Flexible Graphite Substrate – Method, Results and Discussion

The properties of graphite, such as low cost, flexibility, and good thermal and electrical conductivity, suggest that graphite foils would be suitable substrates for synthesis of CNTs [102]. More importantly, there are very few reports concerning the growth of CNTs directly on graphite substrates. CNTs grown on conducting and chemically stable graphite substrates can be utilized in high performance supercapacitors, batteries, or field emitting electron source. In addition to the previous work using n++ silicon substrates, focus of this dissertation was also on the fabrication of vertically aligned CNTs on graphite foil substrates.

Chemical vapor deposition (CVD) method has been shown to be the simplest and most reliable method in fabricating vertically aligned CNTs [103]. In comparison to hot filament CVD, the thermal CVD has the following advantages- low cost, scalable, and relatively easy to implement. As such, this work focuses on optimizing the parameters in thermal-CVD process that influence the growth of CNTs in order to improve its performance.

In thermal CVD, a conventional heat source such as a furnace, infrared lamp, or inductive or resistive heater is used. Usually a catalyst material is heated to 500~1000°C in an inert or reducing gas flow through a tube reactor followed by the introduction of a hydrocarbon gas as the carbon feed source for a period of time. CNTs grown on the substrate are collected after the system is cooled to room temperature.

As part of this work, thermal CVD process in a tube furnace at atmospheric pressure was used for CNT synthesis. In this process, acetylene was used as the carbon source gas, which is easier to break down than methane. Unlike the hot-filament CVD machine, a tube furnace does not have an energy source like the tungsten filament operating at 2000 ^{o}C which is sufficient to break down the input gas mixture, especially methane. Other than acetylene, hydrogen, diluted in argon gas, as well as ammonia diluted in nitrogen gas form the remaining input gas mixture. The graphite foil substrates were sputtered with different thicknesses of buffer (titanium) and catalyst (cobalt) layers for multiple trials to identify and optimize thermal CVD conditions for growing CNTs. The thickness values of titanium and cobalt layers sputtered on the graphite substrates and the CNT growth parameters have been tabulated in table 3.3.

Cross sectional SEM images obtained for the samples at different temperatures and pretreatment times can be seen in figure 3.11 (2 parts). The SEM images for CNT growth trial #22, with near-optimum conditions for CNT growth on graphite can be seen in figure 3.12. This too is a partial collection of the SEM images recorded during these trials.

Table 3.3 Graphite substrates- Ti/Co thicknesses and thermal CVD parameters for CNT synthesis.

Graphite Substrate #	**#1**	**#2**	**#3**	**#4**	**#5**	**#6**	**#7**
Titanium (nm)	10	5	5	15	20	15	20
Cobalt (nm)	3	5	3	3	3	5	5

Trial #	**Samples**	**Temp (^oC)**	**Gases** C_2H_2**= 1 sccm** Ar:H_2:NH_3	**Pretreatment Time (min)**	**CNT growth time (min)**
1	1-3	700	5:1:4	3’	15’
2	1-3	700	5:1:4	2’	15’
3	1-3	700	5:1:4	4’	15’
4	1-3	700	5:1:4	6’	15’
5	1-3	650	5:1:4	3’	15’
6	1-3	650	5:1:4	5’	15’
7	1-3	650	5:1:4	7’	15’
8	1-3	650	5:1:4	9’	15’
9	1-3	650	5:1:2	1’	15’
10	1-3	650	5:1:4	12’	15’
11	1-3	650	5:1:4	15’	15’
12	1-4	650	5:1:6	3’	15’
13	1-4	650	5:1:6	6’	15’
14	1-4	650	5:1:6	9’	15’
15	4-6	650	5:1:4	9’	15’
16	1,4-6	650	5:1:4	11’	15’
17	5,6	650	5:1:6	9’	15’
18	1, 4-6	650	5:1:6	11’	15’
19	5-7	650	5:1:4	6’	15’
20	7	650	5:1:4	9’	15’
21	4-7	650	5:1:4	4’	15’
22	4-7	650	5:1:4	7’30”	15’

As the pretreatment time for the sample 1 (Ti/Co 10/3 nm) was increased at a fixed substrate heater temperature of 650^{o}C, some CNT growth was observed until 12 min pretreatment time after which almost no CNTs were present. As we increased the pretreatment time for the sample 1 at fixed substrate heater temperature of 700^{o}C, there is no improvement in the CNTs' growth for all pretreatment times. Possibly, amorphous carbon might have poisoned the catalyst thus limiting the CNT growth.

In case of sample 2 (Ti/Co 5/5 nm), as the pretreatment time was increased at a fixed temperature of 650^{o}C, poor CNT growth is observed. Same observations were true for the sample with a substrate temperature of 700^{o}C and different pretreatment times. Sample 3 (Ti/Co 5/3 nm) did not show any improvement either at both substrate temperatures, 650 and 700 ^{o}C.

After increasing the buffer layer thickness in case of samples 4 (Ti/Co 15/3) nm) and 5 (Ti/Co 20/3 nm), more CNT growth was observed at 650 ^{o}C, although presence of amorphous carbon could be seen and a lack of any alignment. By further increasing the catalyst thickness in case of samples 6 (Ti/Co 15/5 nm) and 7 (Ti/Co 20/5 nm), CNT growth was noticeably improved with heights of 5-10 μm. Some alignment was observed, but dense CNT growth was also evident.

Cross-sectional SEM images recorded for graphite substrates #4, #5, #6 and #7 at substrate temperature of 700^{o}C and at fixed pretreatment time of 7' 30" show more aligned CNTs growth Figure 3.12. The best results were obtained for sample 6 (Ti/Co 15/5 nm) from trial 22, the CNTs are found to be much more aligned and less amorphous carbon on the top, and it was relatively best CNT growth result.

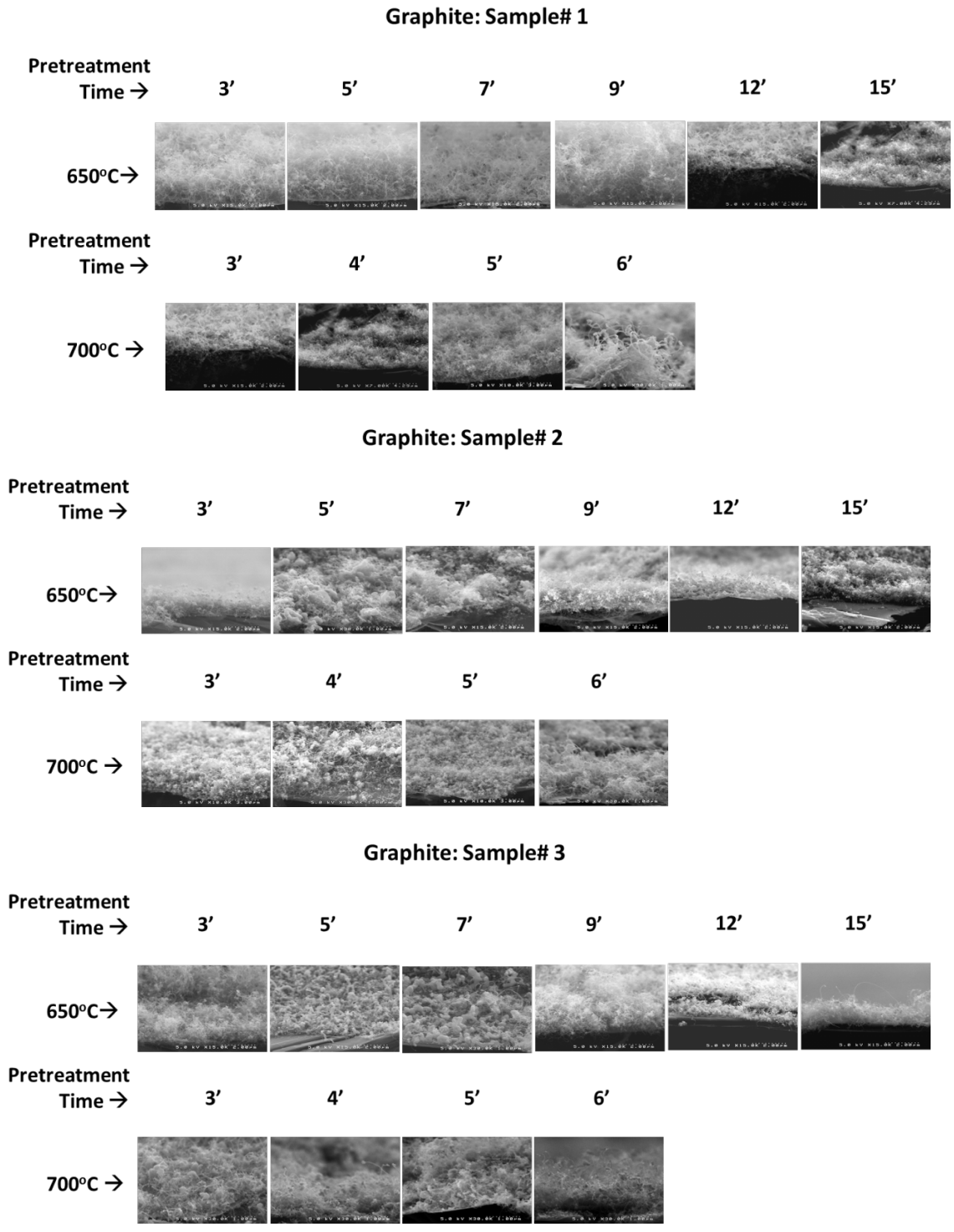

Figure 3.11 (Part 1/2) Cross sectional SEM images recorded under different thermal CVD conditions for Graphite substrates #1, #2 and #3.

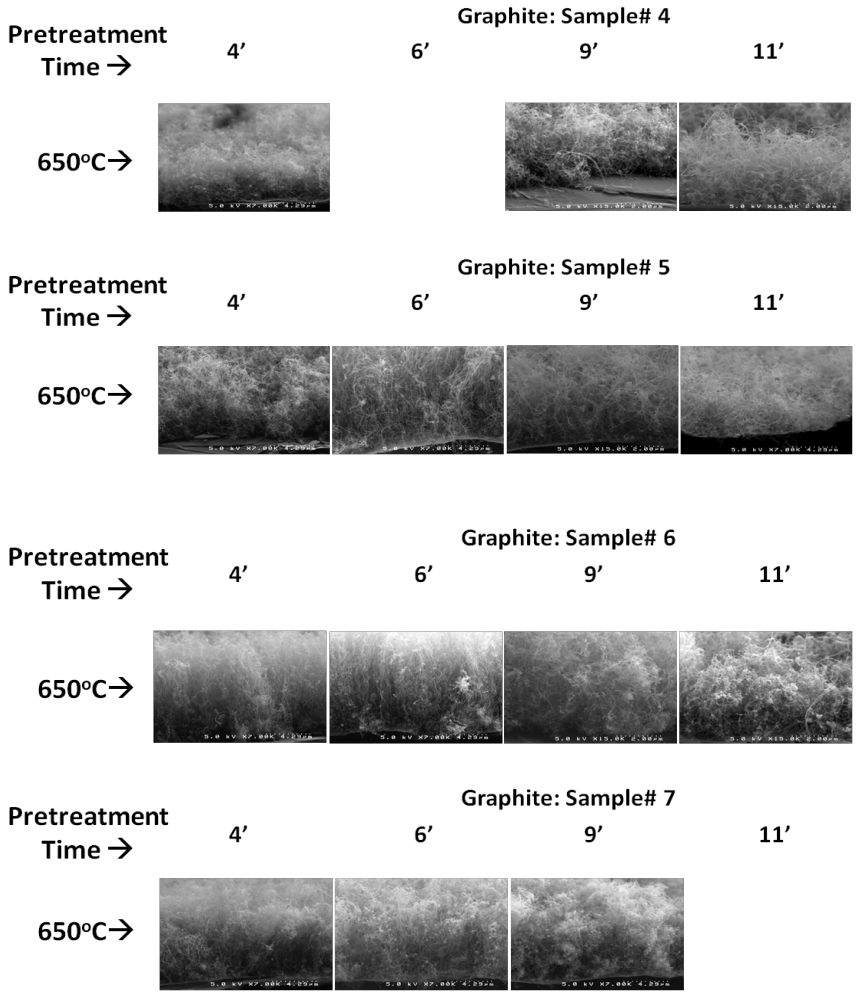

Figure 3.11 (Part 2/2) Cross sectional SEM images recorded under different thermal CVD conditions for Graphite substrates #4, #5, #6 and #7.

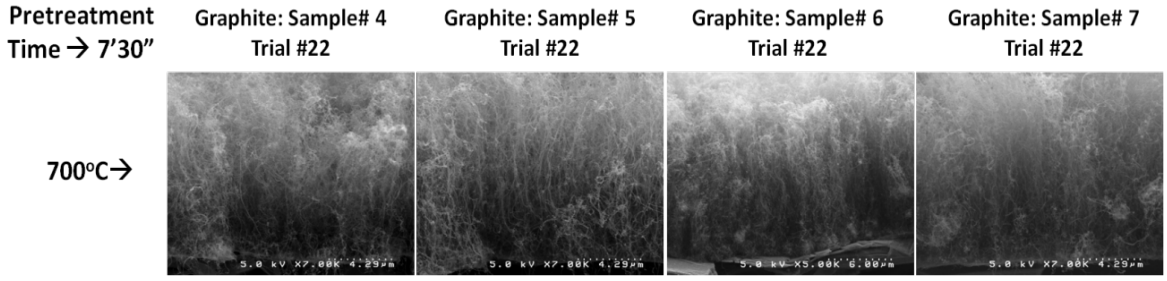

Figure 3.12: Cross sectional SEM images recorded for Graphite substrates #4, #5, #6 and #7 under near-optimum CVD conditions for growing CNTs.

3.2.2 Electrochemical Deposition of MnO_2 on CNT– Results and Discussion

Sample 6 from trial 22, with relatively best CNT growth results, was used as the substrate for electrochemical deposition of the MnO_2. For this experiment, the deposition parameters have been summarized in table 3.4. Electrochemical deposition of manganese dioxide (MnO_2) on CNTs was achieved by direct reduction of 10 mM potassium permanganate ($KMnO_4$) in de-ionized water (18MΩ-cm). The deposition was carried out in a flat cell using cyclic voltammetry in a standard three electrode configuration. Figs. 3.13 shows the SEM images of the MnO_2 coated carbon nanotubes on a highly conductive graphite foil. The MnO_2 is observed to be uniformly and exclusively deposited on the surface of CNTs.

Table 3.4 MnO_2 deposition parameters for CNT synthesized on graphite foil.

[$KMnO_4$](mM)	**Scan Rate (mV/s)**	**Scan Window**	**# of cycles**	**# of steps**	**Interval between cycles**
10	100	-1V to +1V	≤ 40	10	≥ 60s

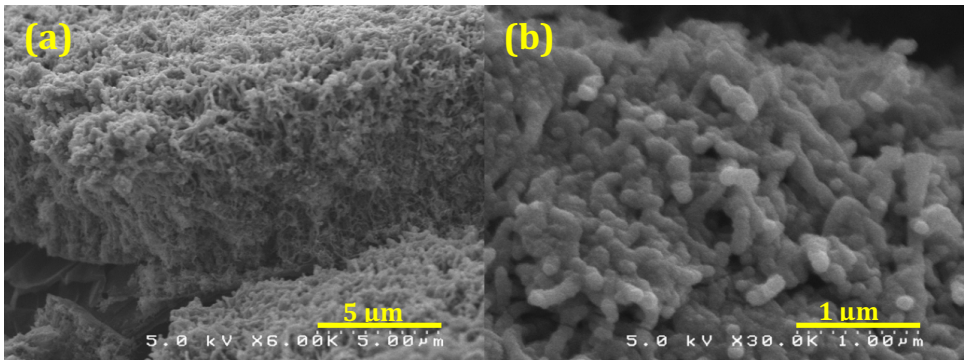

Figure 3.13 (a) and (b) SEM images showing MnO_2 coating on the CNT synthesized on flexible graphite foil.

The CVs were recorded in 0.1M KCl before and after 40 cycles of MnO_2 deposition at 100mV/s, 50mV/s, and 10mV/s and have been overlaid, as seen in figures 3.14. The CVs recorded before MnO_2 depositions have also been included for comparison. CVs recorded at 50mV/s before and after 30 and 40 cycles of MnO_2 deposition have been overlaid, as seen in figure 3.15. Based on the CVs, there is a gradual increase in the capacitive currents until 40 cycles of MnO_2 deposition which suggests that at the given MnO_2 thickness, the K^+ ions are still able to diffuse deeper into the MnO_2/CNT network to enhance the capacitive currents at the slower scan rates. The CVs change shape because of greater IR losses which distort the CVs as the MnO_2 deposited has poor electrical conductivity.

Figure 3.14 CVs recorded in KCl before (a) and after (b) 40 cycles of MnO_2 deposition at different scan rates (Red→ 100mV/s, Blue→ 50mV/s, Brown→ 10mV/s).

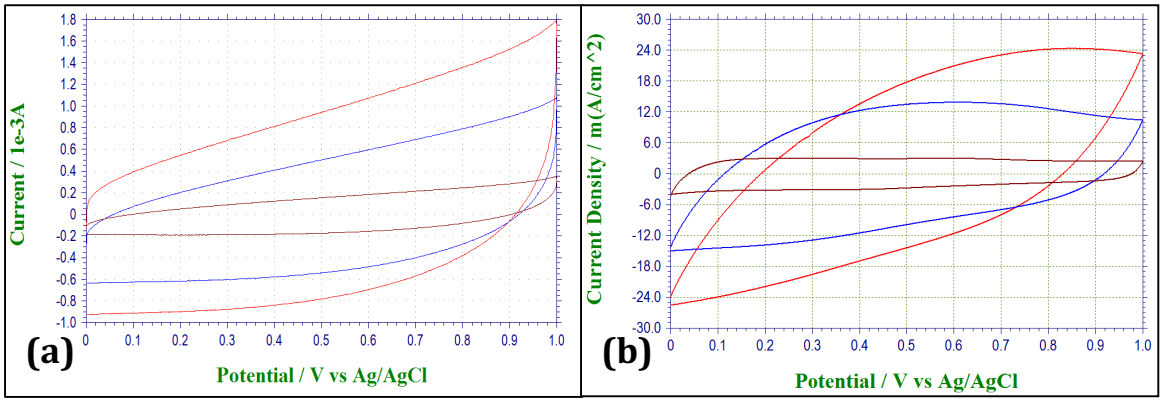

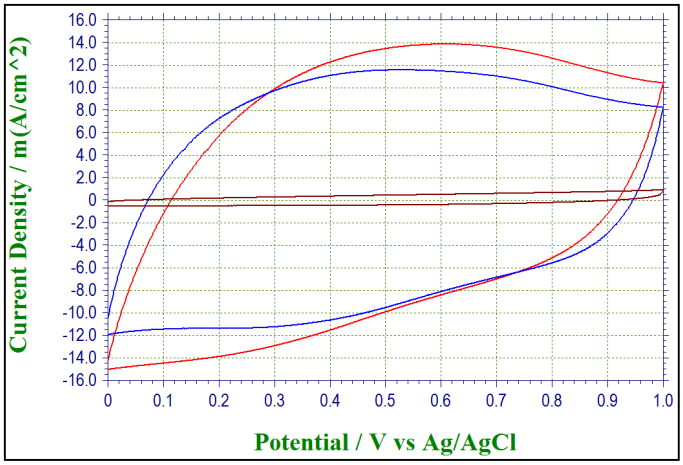

Figure 3.15 CVs recorded in KCl after 40 cycles of MnO_2 deposition at 50mV/s (Red→ 40 cycles, Blue→ 30 cycles, Brown→ CNT+Gr).

The presence of the CNTs and MnO_2 films were further investigated using Raman spectroscopy. The spectra were collected using Thermo Scientific DXR spectrometer using 532nm green laser as the excitation sourceThe Raman spectrum recorded from the as-grown CNTs can be seen in figure 3.16 (a), with signature peaks at 1590 cm^{-1} (graphitic G- band) and 1350 cm^{-1} (defect or disorder D- band). The ratio of the peak intensities, I_D/I_G of 1.4 suggests that the CNTs may possess structural defects and amorphous carbon. However, since they are being coated with MnO_2 film, they have a limited effect on the final energy storage behavior of the supercapacitor cell. The Raman spectrum for the MnO_2 film can be seen in figure 3.16 (b). A very strong peak at 635.5 cm^{-1} with a small FWHM of ~40 cm^{-1} is observed which is characteristic of α-MnO_2 phase, arising from the breathing or symmetric stretching vibrations of the MnO_6 octahedron in the MnO_2 compounds. Two weak peaks recorded at approximately 292 and 350 cm^{-1}, which correspond to the bending modes of O-Mn-O, were also observed in the spectrum and can be attributed to the formation of Mn_2O_3 or Mn_3O_4 induced by the laser heating. The two characteristic peaks of G-band and D-band arising from the vibration of

the sp^2 hybridized C–C bonds and disorder-induced signal, respectively, were not observed in spectrum due to the MnO_2 layer.[106 -108].

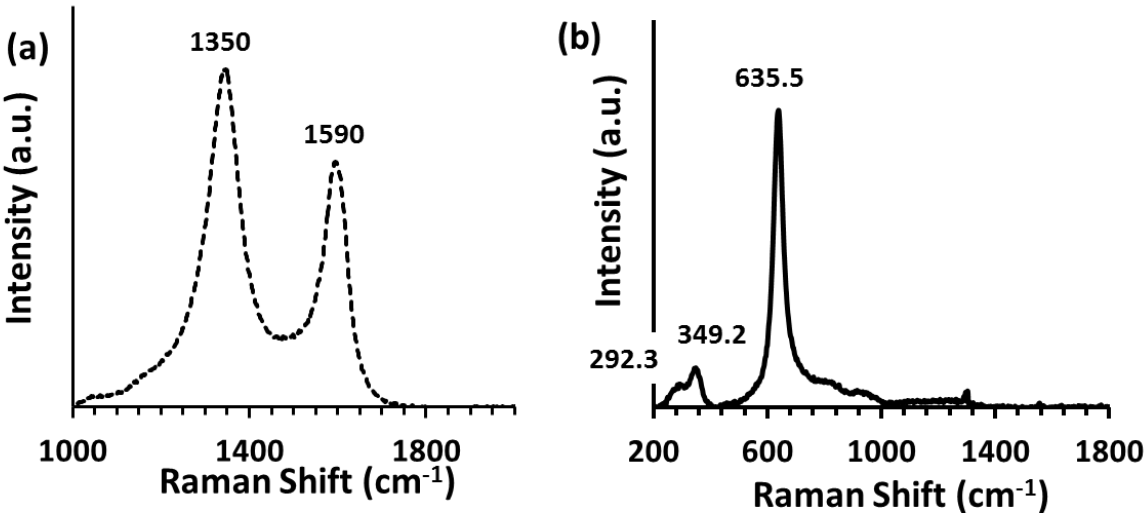

Figure 3.16 Raman spectra, obtained using green laser (532 nm) as the excitation source: (a) As grown CNTs with the D peak at 1350 cm^{-1} and the G peak at 1590 cm^{-1}; (b) MnO_2 spectrum showing the characteristic Mn-O vibrational bands.

The electrochemical characterization was performed in a three-electrode arrangement using platinum as the counter electrode and Ag/AgCl as a reference electrode in 0.1 M KCl electrolyte. Cyclic voltammograms were recorded at different scan rates in 0.1 M KCl solution: 2 mV/s, 10 mV/s, 50 mV/s and 100 mV/s. The as-prepared electrode delivers the highest capacitance at 2 mV/s scan rate: 2.25 F, 240 mF/cm^2, 187.8 mF/cm^2 and 163.3 F/g. The electrode shows a 12x improvement in capacitance at 10 mV/s over as synthesized CNTs. Based on the Nyquist plot, the ESR for this scaled up electrode was calculated to be 1.4 Ω.

The results for the MnO_2/CNT/Graphite electrode from the cyclic voltammetry and A. C. impedance experiments have been summarized in table 3.5. The CV in terms of C (mF/cm^2) vs. potential (V) recorded at 2 mV/s with the highest capacitance can be seen

in figure 3.17(a). The Nyquist plot recorded by A.C. impedance measurements can be seen in figure3.17 (b).

Table 3.5 Results from electrochemical characterization using cyclic voltammetry on MnO_2/CNT/Graphite supercapacitor electrode.

C(mF)	Area (cm^2)	Mass (mg)	Scan Rate (mV/s)	C (mF/cm^2)	C_{sp} (F/g)	(ΔV)	E_{sp} (Wh/kg)	ESR (Ω)	P_{sp} (kW/kg)
2253	12	13.8	2	187.8	163.3	1	22.68	1.4	12.94

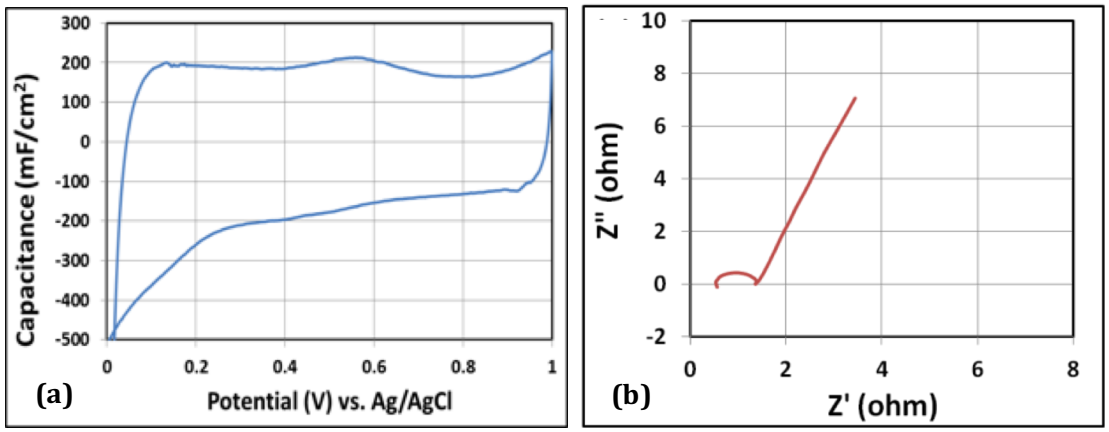

Figure 3.17 Ultracapacitor electrode characterized in 0.1 M KCl:
(a) CV recorded at 2 mV/s and expressed as C (mF/cm^2) versus potential (V).
(b) Nyquist plot recorded for the ultracapacitor electrode using A.C. Impedance Spectroscopy.

Constant current charge-discharge experiments were also performed at different current densities: 0.8 mA/cm^2, 2 mA/cm^2, 5 mA/cm^2 and 10 mA/cm^2. The highest capacitance for the MnO_2/CNT/Graphite supercapacitor electrode was obtained at 0.8mA/cm^2 or 10mA: 2.212F, 184.3mF/cm^2 and 160.3F/g. From the potential drop, the series resistance of 2.66Ω was obtained. The charge discharge curves recorded at the

different current densities can be seen in figure 3.18. Results from the charge-discharge experiments have been tabulated in table 3.6.

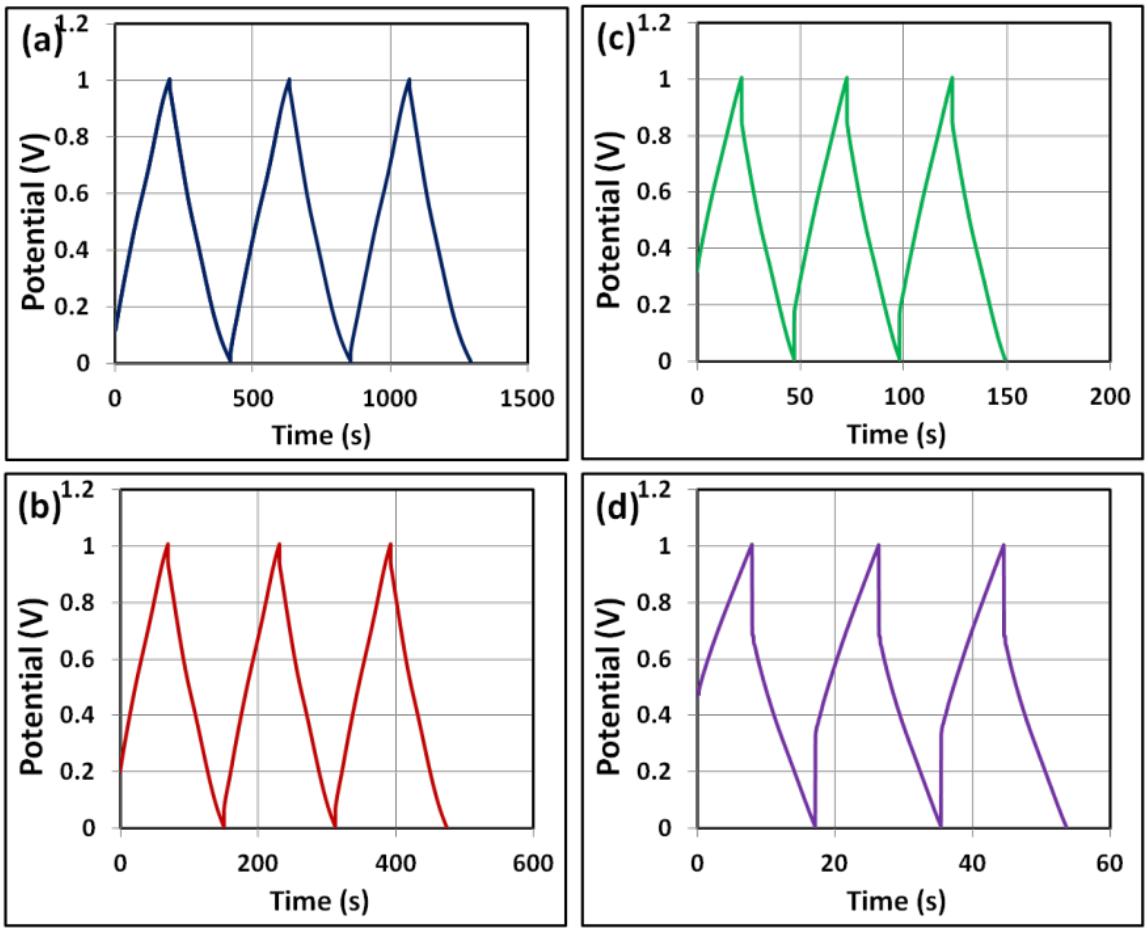

Figure 3.18 Constant current charge discharge curves recorded at different current densities (a) 10mA or 0.8mA/cm^2; (b) 24mA or 2mA/cm^2; (c) 60mA or 5mA/cm^2; (d) 120mA or 10mA/cm^2.

Table 3.6 Results from constant current charge-discharge experiments using MnO_2/CNT/Graphite supercapacitor electrodes.

C(mF)	Area (cm^2)	Mass (mg)	J (mA/cm^2)	C (mF/cm^2)	C_{sp} (F/g)	(ΔV)	E_{sp} (Wh/kg)	R (Ω)	P_{sp} (kW/kg)
2212	12	13.8	0.83	184.33	160.29	1	22.26	2.66	6.81
1944	12	13.8	2	162.00	140.87	1	19.57	2.65	6.84
1521	12	13.8	5	126.75	110.22	1	15.31	2.64	6.86
1080	12	13.8	10	90.00	78.26	1	10.87	2.66	6.81

3.3 Fabrication and Characterization of Double-Sided CNT/MnO_2 Supercapacitor Electrodes on Flexible Graphite Substrate

3.3.1 Double-Sided Synthesis of CNTs on Graphite Substrate

The objective of these experiments was to scale up the electrodes by utilizing both sides of the substrate. In this study, CNTs were synthesized on both sides of the graphite foil uniformly and consistently. To accomplish this, two different substrate holders were fabricated using (2 mm thick graphite foil) where the substrates can be mounted vertically as shown in figure 3.19 (a) or horizontally as shown in figure 3.19 (b). Mounting the substrates in a vertical configuration raised the possible issue of gravitational effects and how it may affect the distribution of the catalyst nanoparticles and thereby the uniformity of the CNTs. To counter this, the second substrate holder was designed and fabricated that allowed horizontal mounting of the substrates. In this way, the gravitational force distribution would be uniform across the surface, although it might vary between the top and bottom surfaces. Additionally, thinner quartz rods were procured and used to fabricate this substrate holder. As per this design, a pair of quartz rods would secure the substrate near the tabs, away from the active area, while single quartz rod on the left would be placed to provide support at the other end.

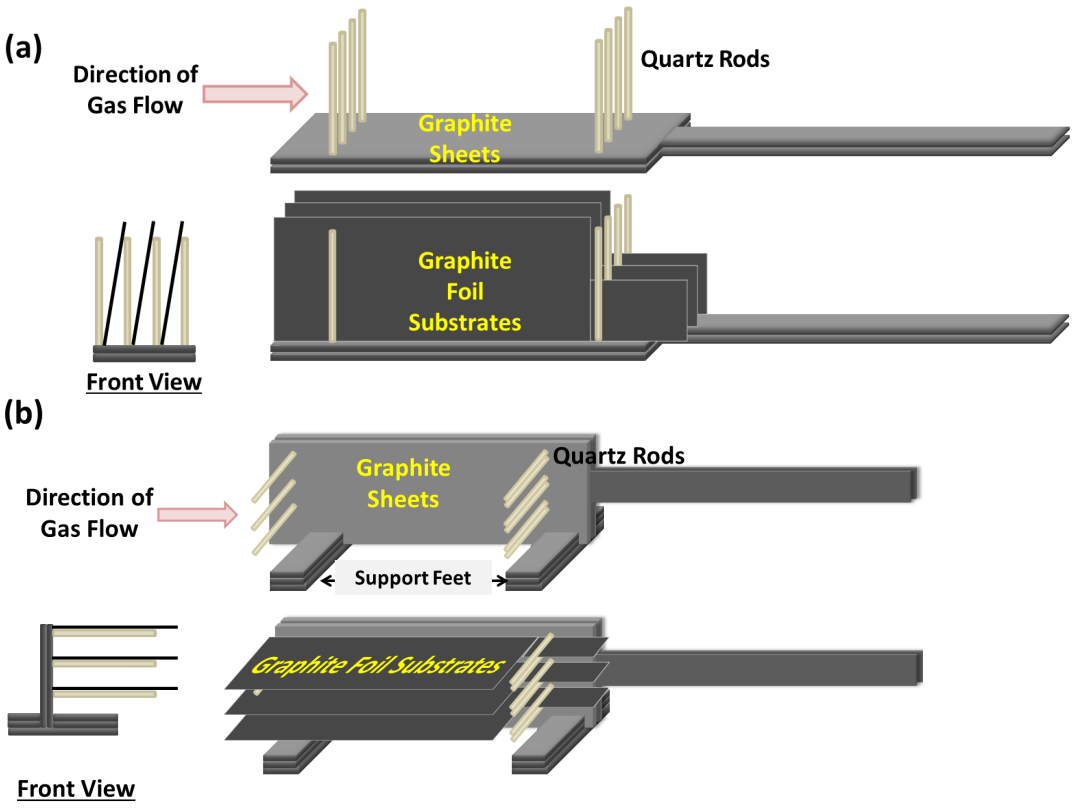

Figure 3.19. Schematic representation of the double-sided synthesis of CNTs on Graphite substrate.
(a) The substrates mounted in vertical configuration.
(b) The substrates mounted in horizontal configuration.

As reported in our previous section, a thin graphite foil (127µm) is used as our substrate. After cleaning in acetone, D. C. sputtering technique was used to deposit buffer (Ti) and catalyst (Co) layers. Table 3.7 summarizes the different parameters used in the trials to grow uniform CNT on the large substrates, placed in vertical and horizontal orientations. Cross sectional images of CNTs grown on both sides were recorded using SEM and have been included in figure 3.20. The first three attempts did not yield any CNTs on the graphite substrates and were not used for SEM characterization. The cross-sectional SEM micrographs of the graphite substrates placed vertically show CNT growth consistent on both sides of the graphite foil, with CNT height of 2 around µm. However,

the CNTs are not well aligned in this orientation. The cross-sectional SEM micrographs of the graphite substrates placed horizontally show dense CNT growth consistent on both sides of the graphite foil, with CNT height of around 10 μm and were used for subsequent experiments.

Table 3.7 Process parameters used for large area CNT synthesis on both sides of the graphite substrates placed vertically and horizontally in the thermal CVD tube-furnace.

Trial #	**Ti /Co (nm) (both sides)**	**Temp (^{O}C)**	**Gases**		**Pre-Treatment Time (min)**	**CNT Growth Time (min)**
			Ar:H_2:NH_3	**C_2H_2**		
Vertically Mounted Graphite Substrates						
1	15/3	650	5:1:9	3	8	15
2						
3						
4	15/3	650	5:1:9	3	8	15
5		700				
6		750				
7		800				
Horizontally Mounted Graphite Substrates						
8	15/3	650	5:1:9	2	8	15
9		700				
10		750				
11		800				

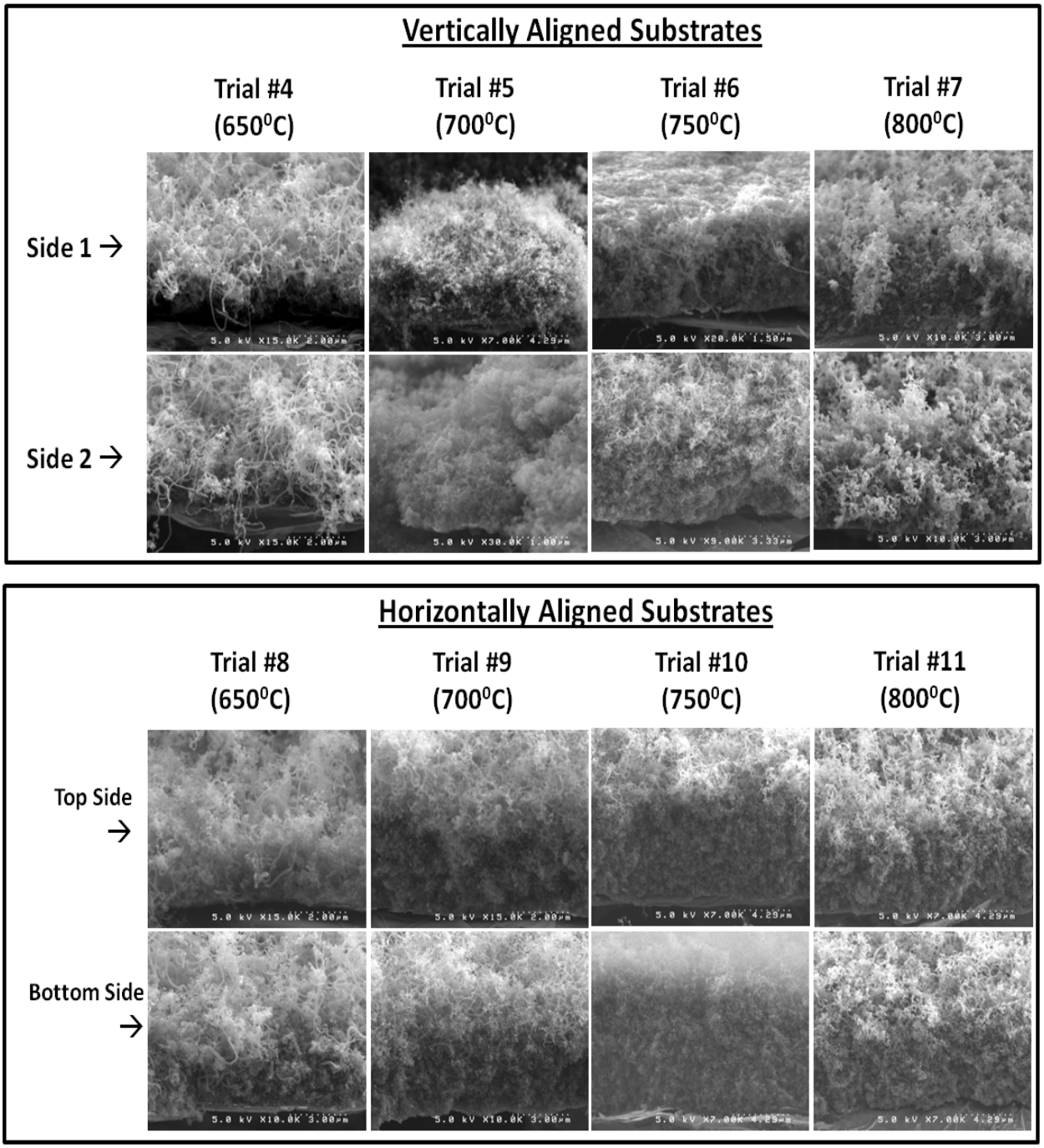

Figure 3.20 Cross sectional SEM micrographs recorded for CNT synthesized on both sides of graphite substrates mounted and placed inside the tube furnace in vertical and horizontal configurations.

3.3.2 Electrochemical Deposition of MnO_2 on CNT – Results and Discussion

Electrochemical deposition of MnO_2 was achieved using parameters discussed in table 3.4. In order to preserve the CNTs grown on both sides of the graphite foil, extreme care had to be taken while handling the samples. In order to perform electrochemical deposition and characterization, a new substrate holder was fabricated out of Teflon. This allowed concurrent deposition of MnO_2 on both sides of the substrate. A blow-up of the fixture fabricated can be seen in figure 3.21. Figure 3.22, left, shows the SEM image of the cross section view of the MnO_2 coated carbon nanotubes on a highly conductive graphite foil. The MnO_2 is observed to be uniformly and exclusively deposited on the surface of CNTs, and based on the calculation, a mass loading of 0.651 mg/cm^2 was achieved.

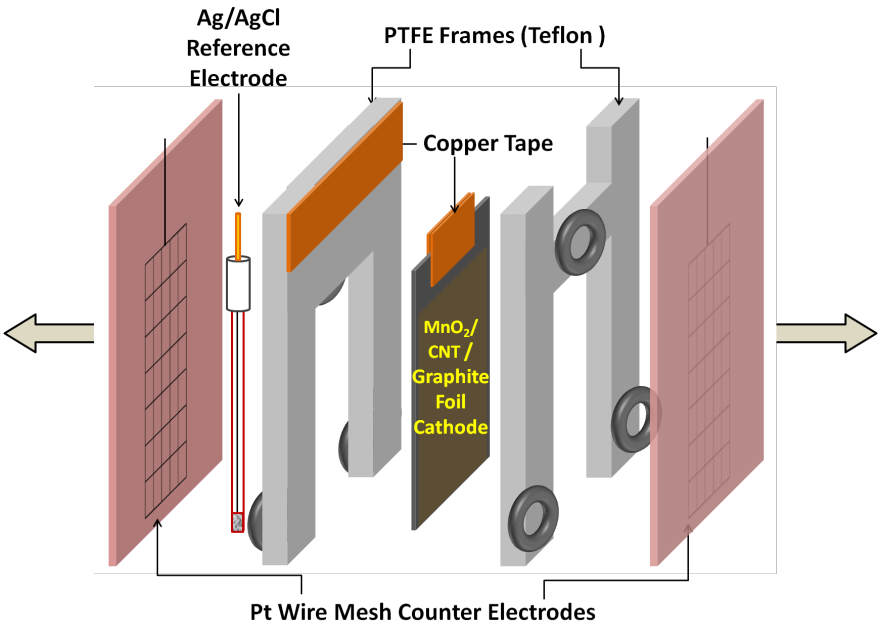

Figure 3.21 Schematic 'blow-up' representation of test setup for electrochemical deposition of MnO_2 and electrochemical characterization.

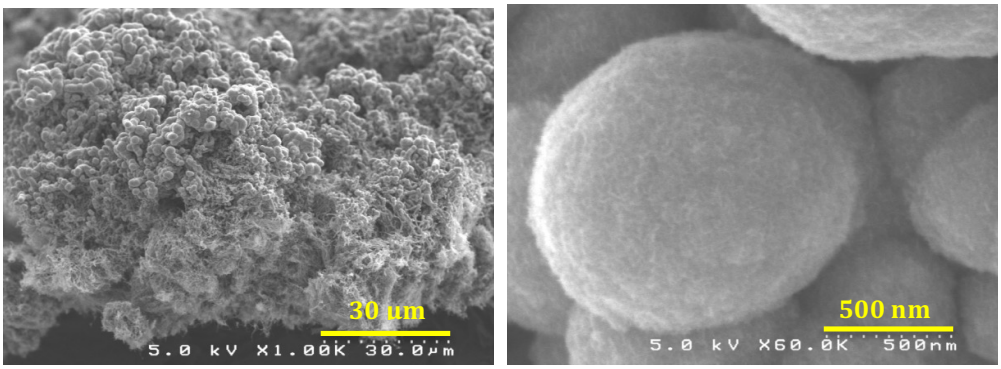

Figure 3.22: SEM image on the left showing the cross-section of the electrode showing MnO_2 coating on the CNT; the SEM micrograph on the right showing the porous microstructure of the MnO_2 coating.

The electrochemical characterization was performed in aqueous electrolyte (0.1 M KCl) in a 3-electrode configuration with Ag/AgCl reference electrode and Pt wire counter electrode. The substrate size was 4cm x 1.8cm with a total mass of the active material (MnO_2) mass on the electrode of 4.2 mg. The capacitance value calculated from cyclic voltammetry at 2 mV/s was more than 1.8 F, which is equal to 144 mF/cm^2 and 439 F/g. The equivalent series resistance calculated using A.C. Impedance Spectroscopy was 2.75 Ω. The results for the MnO_2/CNT double-sided electrode from the cyclic voltammetry and AC impedance experiments have been summarized in table 3.8. The CV with the high capacitive currents, expressed in terms of current (mA/cm2) versus potential (V), can be seen in Figure 3.23 (a). The CV, in terms of C (mF/cm^2) versus potential (V) recorded at 2 mV/s, with the highest capacitance can be seen in Figure 3.23(b). The Nyquist plot recorded by AC Impedance Spectroscopy can be seen in Figure 3.23(c). The specific energy and specific power were calculated according to equations 3.1 and 3.2.

$$E_{sp}\left(\frac{Wh}{kg}\right) = \frac{1}{2}\,\frac{CV^2}{3600\,m_{eff}} \qquad 3.1$$

$$P_{sp}\left(\frac{W}{kg}\right) = \frac{V^2}{4Rm_{eff}} \qquad 3.2$$

where E_{sp} is the specific energy, P_{sp} is the specific power, C is the total capacitance, R is the resistance from the charge-discharge curve, m_{eff} is the effective mass of MnO_2 ,and V is the potential window.

Table 3.8 Double-sided Ultracapacitor Electrode: Results from electrochemical characterization in aqueous electrolyte (0.1M KCl) in a three-electrode configuration.

C(mF)	Area (cm^2)	Mass (mg)	Scan Rate (mV/s)	C (mF/cm^2)	C_{sp} (F/g)	ΔV (V)	E_{sp} (Wh/kg)	ESR (Ω)	P_{sp} (kW/kg)
1843.5	6.4	4.2	2	144	**439**	1	61	2.75	22

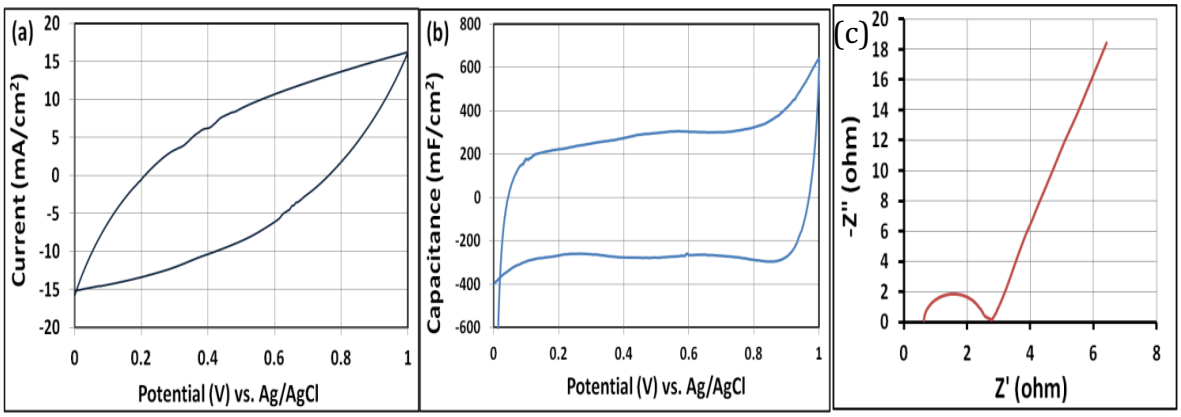

Figure 3.23 Double-sided Ultracapacitor Electrode characterized in 0.1M KCl:
(a) CV recorded at 100 mV/s and expressed as current (mA/cm^2) versus potential (V);
(b) CV recorded at 2 mV/s and expressed as C (mF/cm^2) versus potential (V).
(c) Nyquist plot recorded for the double-sided ultracapacitor electrode using A.C. Impedance Spectroscopy.

In order to evaluate the consistency of the double-sided electrode, each side was tested individually by galvanostatic or constant-current charge/discharge experiments. High current values were used in these experiments: 16mA (2.5mA/cm^2) and 40mA (6.25mA/cm^2) in 0.1M KCl. The electrode was able to handle these high current densities without any problems. At both the current densities, the capacitance values for each side varied within 10%. The discharge segments of the two sides recorded at 16mA and 40mA can be seen in figure 3.24 (a) and (b), respectively. The inset includes the preceding charging segment in the same experiments. The results for the MnO_2/CNT double-sided electrode from the cyclic voltammetry and AC impedance experiments have been summarized in Table 3.9. The capacitance from the two sides of the electrode can be added to arrive at the total value based on the fact that they form two capacitors in parallel. The specific quantities for capacitance, energy and power, have been calculated for Side 1 + Side 2 and included in table 3.9.

The capacitance can be calculated from the slope of the discharge segment using equation 3.3, while the resistance can be calculated using the initial potential drop, as seen in equation 3.4.

$$C\left(\frac{mF}{cm^2}\right) = \frac{I\left(\frac{mA}{cm^2}\right)}{\Delta V/\Delta t\ \left(\frac{V}{s}\right)} \qquad 3.3$$

$$R(\Omega) = \frac{\Delta V(V)}{I(A)} \qquad 3.4$$

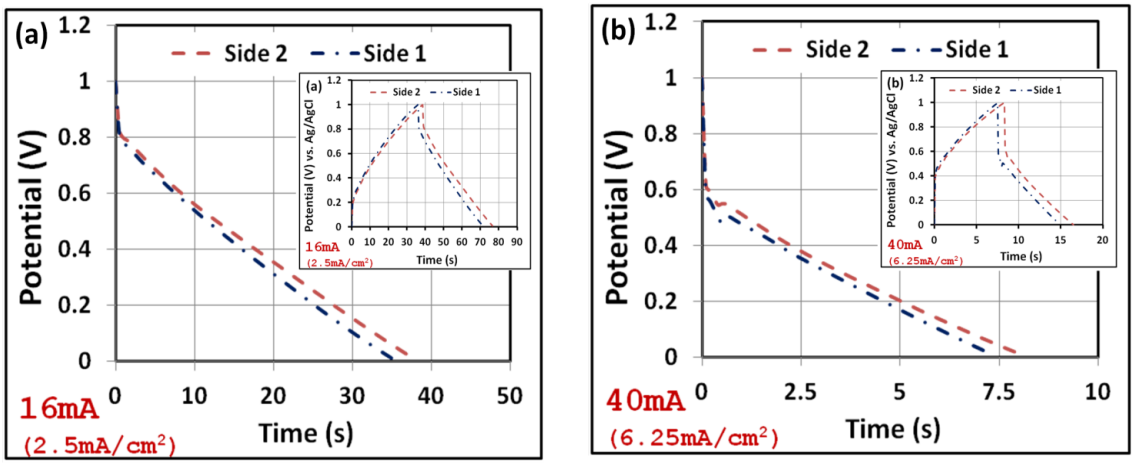

Figure 3.24 Discharge plots recorded from galvanostatic charge and discharge experiments in aqueous electrolyte (0.1M KCl) in a 3-electrode configuration performed independently for each side (a)Charge/Discharge Current= 16mA (b) Charge/Discharge Current= 40mA.
Inset: Both the charge and discharge segments of the plots.

Table 3.9 Summary of results from galvanostatic charge and discharge experiments for each side of the ultracapacitor electrode with an active area of 6.4 cm^2 and total MnO_2 mass of 4.2 mg, in aqueous electrolyte (0.1M KCl) recorded at 16mA (2.5mA/cm^2) and 40mA (6.25mA/cm^2) in a voltage window of 1 V.

	C (mF)	Area (cm^2)	J (mA/cm^2)	C (mF/cm^2)	C_{sp} (F/g)	E_{sp} (Wh/kg)	R (Ω)	P_{sp} (kW/kg)
Side 1	**558.4**	6.4	**2.5**	87	-	-	12	-
Side 2	**598.4**		**2.5**	94			11.1	
Side 1	**292**	6.4	**6.25**	46	-	-	10.4	-
Side 2	**322.8**		**6.25**	50			9.6	
Combined Results from Side 1 and Side 2								
Side 1+ Side 2	**1156.8**	12.8	**2.5**	90	275	38	5.76	10
	614.8	12.8	**6.25**	48	146	20	4.99	12

3.4 Development of CNT/MnO_2 Symmetric Supercapacitor Prototype Cell

3.4.1 Fabrication of the Multi-Layer Supercapacitor Prototype Cell

In the previous section, CNTs and MnO_2 were combined to form a single electrode of high power density and energy density. The MnO_2 needs to have a porous structure to sustain cation diffusion and facile charge transfer kinetics. The CNTs can provide a mesoporous structure with large surface area to coat MnO2 and act as current conductors. Based on these results, a scaled up prototype was designed and fabricated using a stack of multiple, double-sided electrodes. **To the best of my knowledge, no work has been published on such a device.** The electrolyte used was a solution of 1M TEATFB (tetraethylammonium tetrafluoroborate) in acetonitrile (ACN).

Figure 3.25 shows a schematic representation of the structure, consisting of vertically aligned CNTs grown on the opposite faces of a graphite substrate. Vertically aligned carbon nanotubes were directly grown on double-sided graphite foil by the thermal chemical vapor deposition (T-CVD) technique in a tube furnace with a 2-inch-diameter horizontal quartz tube at atmospheric pressure as discussed in section 3.3.1. The graphite substrates were placed in the middle of CVD reactor, where the highest point of

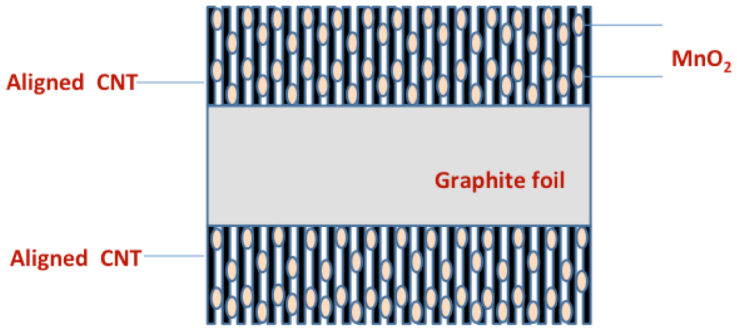

Figure 3.25 Schematic representation of the CNT array fabricated by T-CVD on both sides of the graphite substrate and coated with MnO_2.

temperature is measured. Then the CVD reactor was heated up to 650°C in Argon (Ar)/ Hydrogen (H_2) (1:5) environment and the substrates were annealed for 15 minutes followed by exposure to ammonia (NH_3) (100 ppm in N_2), which helps to reduce formation of amorphous carbon. The ammonia gas was kept flowing with a constant flow rate (H_2:Ar:NH_3= 1: 5: 10) for both the pretreatment duration of 7.5 minutes and the following growth period. Acetylene (C_2H_2) gas at flow rate of 5 sccm was introduced, as the carbon source. After 15 minutes CNT growth time, both NH_3 and C_2H_2 were switched off to terminate the CNT growth and then the reactor was cooled down to room temperature under Ar/ H_2 gas flow.

Electrochemical deposition of manganese dioxide (MnO_2) on the double-sided CNTs was achieved by direct reduction of 10 mM potassium permanganate ($KMnO_4$) in de-ionized water (18MΩ-cm). The deposition was carried out in a flat cell using cyclic voltammetry in a standard three electrode configuration.

The objective of this work was to fabricate a supercapacitor prototype cell by assembling eight double-sided electrodes, stacked on each other with a polyethylene separator between each electrode resembling the schematic seen on the left in Figure 3.26. The electrodes at the ends were only single sided. The equivalent circuit of the supercapacitor cell can be seen on the right in figure 3.26, consisting of seven capacitors connected in parallel. The substrates used had an active area of 4cm x 2 cm and 1cm x 2cm tabs for electrical contacts. The prototype supercapacitor cell was assembled by stacking eight double-sided electrodes *(the two electrodes at the ends had MnO_2 on one side only)*, with a polypropylene separator between each electrode resembling the schematic seen in figure 3.26. The separators and electrodes were pre-soaked in the

organic electrolyte consisting of 1M TEATFB in acetonitrile for 5 minutes to ensure complete incorporation of the electrolyte. Electrodes were assembled with the separators and placed in a flexible pouch cell package, the Al tabs were laid over the graphite tabs and sealed using an impulse heat sealer. The remaining electrolyte (10 cc) was added to the cell from the open side of the package before finally sealing it off.

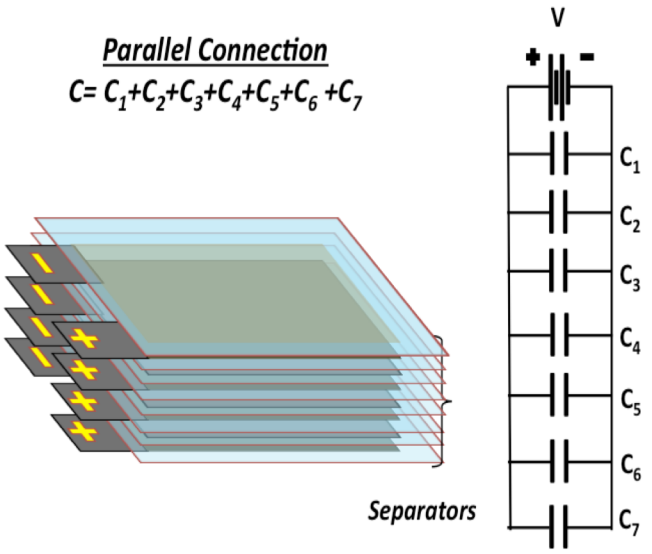

Figure 3.26 Multi-layer electrode structure for a supercapacitor

A prototype supercapacitor cell based on double-sided CNT/MnO_2 electrodes in organic electrolyte, as shown in a schematic in Figure 3.27, was successfully fabricated. The prototype cell supercapacitor measures 8 cm x 10 cm, with a final packaged weight of 10.756 grams. This prototype cell is not optimized design for the commercial applications. The electrochemical characterization of supercapacitor in organic electrolyte, including cyclic voltammetry (CV), galvanostatic charge–discharge, and

electrochemical impedance spectrometry (EIS), were investigated using an electrochemical working station (CHI660C) at room temperature.

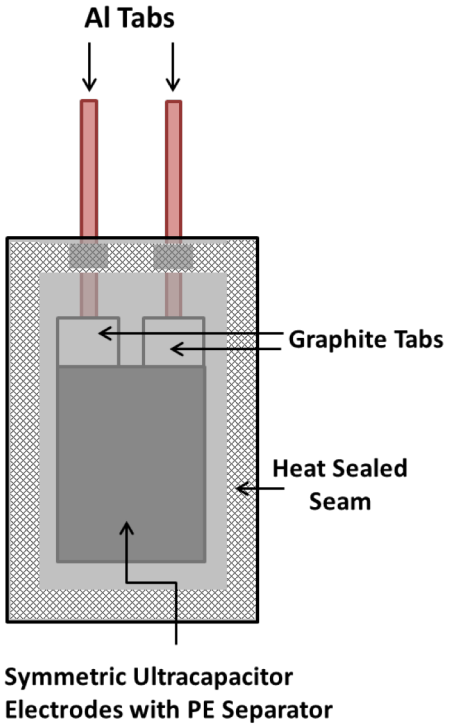

Figure 3.27 A schematic of supercapacitor cell assembled in a pouch cell with Al tab for electrical contact.

3.4.2 Electrochemical Characterization of CNT/MnO_2 Symmetric Supercapacitor Prototype Cell – Results and Discussion

The supercapacitor cell was characterized in 1M TEATFB in acetonitrile and the cyclic voltammograms (CV) recorded at 2 mV/s and expressed as capacitance (mF/cm^2) versus potential (V) can be seen in Figure 3.28. Cyclic voltammetry was performed over different potential windows ranging from 0 -1 V, 0 -2 V, and 0 -2.5 V. In order to extend the potential window, organic electrolyte is preferred over aqueous electrolyte for supercapacitor.

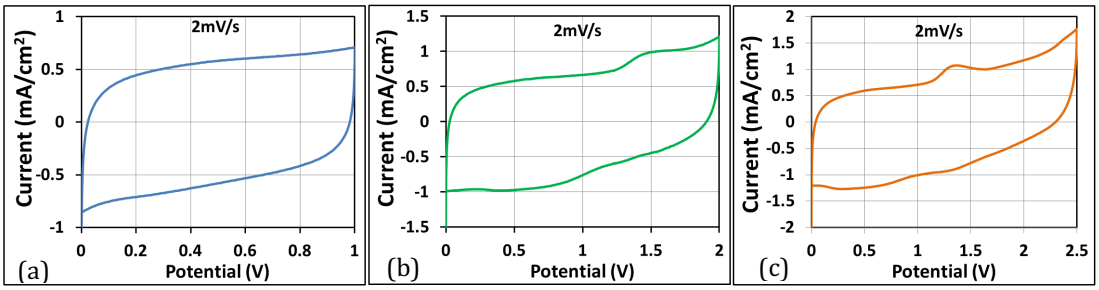

Figure 3.28 Supercapacitor characterized in 1M TEATFB in Acetonitrile-Cyclic voltammograms recorded at 2 mV/s and expressed as Current (mA/cm^2) versus potential (V); (a) 0-1V, (b) 0-2V, (c) 0-2.5V.

As shown in Fig. 3.28, the CV curves of the supercapacitor at scan rate of 2 mV/s exhibit a nearly rectangular shape, which indicate an excellent capacitance behavior, low contact resistance, and fast charge propagation within the electrodes. The capacitance was found to be equal to 2325 mF, 3120 mF, and 3662 mF, for 0 - 1 V, 0 - 2 V, and 0 - 2.5 V, respectively.

The specific capacitance of the MnO_2 in organic electrolyte can be calculated by equation 3.5.

$$C_{sp}\left(\frac{F}{g}\right) = \frac{C_T}{3.5} \times \frac{14}{m_T} \qquad 3.5$$

where C_{sp} is the specific capacitance, C_T is the total capacitance, and m_T is the total mass of MnO_2 on all eight electrodes (or 14 sides), *the electrodes at the two ends are coated only on one side*.

Each electrode's MnO_2 mass was measured individually using a microbalance with an accuracy of 0.1 mg. If we consider all electrodes have equal capacitance of C (for each side), then, based on the circuit diagram in figure 3.26, the equivalent or total capacitance of the prototype cell, C_T will be equal to 3.5C (as calculated by 7 x C/2 because of 2 capacitors in series and then 7 in parallel). The total mass of MnO_2 in the cell, m_T,

considering 14 sides, can be used to calculate the average mass of MnO_2 on each side by $m_T/14$. This allows us to use equation 3.5 to calculate the specific capacitance of MnO_2. The highest specific capacitance of 514 $F.g^{-1}$ is achieved at scan rate of 2mV/s for the potential window of 0 - 2.5 V.

Figure 3.29 shows the Nyquist plot of the supercapacitor operated at 0.01 Hz and 100 kHz frequency range. The Nyquist plot was recorded for the supercapacitor using A.C. Impedance Spectroscopy showing a low equivalent series resistance (ESR) value of 0.8 Ω. The low values of ESR in supercapacitor are related to the interconnected network of highly conductive vertically aligned CNTs within the MnO_2.

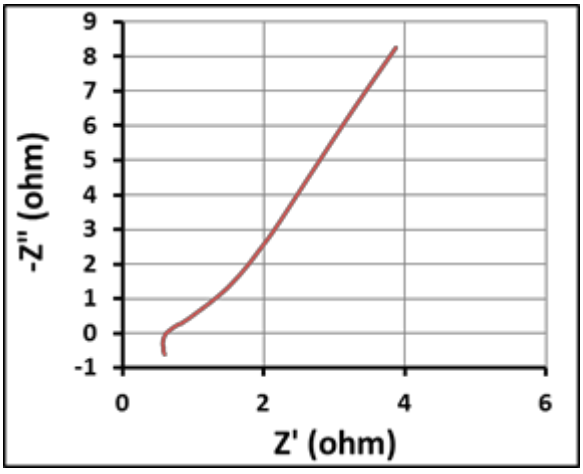

Figure 3.29 Nyquist plot recorded for the supercapacitor in 1M TEATFB in Acetonitrile using A.C. Impedance Spectroscopy showing a low ESR value of 0.8Ω.

The specific energy and specific power for the prototype cell were calculated according to equations (3.1) and (3.2). The results from the CV characterization using organic electrolyte (1M TEATFB in ACN) have been summarized in table 3.10.

Table 3.10 Electrochemical characterization of supercapacitor prototype cell in organic electrolyte (1M TEATFB in ACN) using cyclic voltammetry experiments at 2 mV/s scan rate. The electrodes had an active area of 8 cm^2, with MnO_2 mass of 28.5 mg, and ESR of 0.8 Ω.

C (mF)	**Scan Rate ($mV.s^{-1}$)**	**C ($mF.cm^{-2}$)**	**ΔV**	**E_{sp} ($Wh.kg^{-1}$)**	**ESR (Ω)**	**P_{sp} ($kW.kg^{-1}$)**
2323.5	2	290.44	1	11.32	0.8	10.96
3120.8	2	390.09	2	60.83	0.8	43.86
3662.8	2	457.84	2.5	111.56	0.8	68.53

Figure 3.30 shows results from galvanostatic charge and discharge experiments for supercapacitor in organic electrolyte (1M TEATFB in acetonitrile) at different currents (40mA, 80mA, and 160 mA) for three voltage windows ranging from 0 - 1 V, 0 - 2 V, and 0 - 2.5 V. As shown in Fig 3.30, all charge–discharge curves are a non-ideal triangular shape at various current densities, which is a typical characteristic of pseudocapacitors due to redox process.

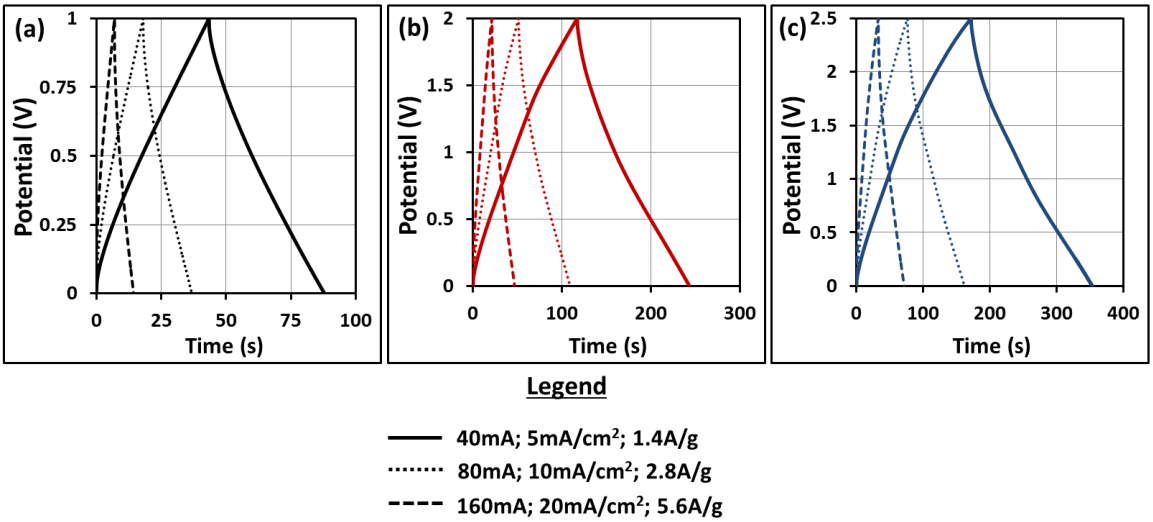

Figure 3.30 Results from galvanostatic charge and discharge experiments for supercapacitor (1M TEATFB in Acetonitrile) for three voltage windows: (a) 0 – 1V, (b) 0 – 2V, and (c) 0 – 2.5V.

The highest capacitance for potential ranges of 0 - 1V, 0 - 2 V, and 0 - 2.5 V was found to be equal to 1800 mF, 2448 mF, and 2764 mF, respectively, at a constant discharge current of 40mA or 5mA.cm^{-2}. The supercapacitor exhibited the highest specific capacitance at the low discharge current densities used in this work, for all voltage windows. When high discharge rates are used (high discharge currents), the cations do not have enough time to diffuse through the hybrid structure resulting in lower capacitance values.

The resistance is a very important factor to determine the power density of a supercapacitor since it limits the rate at which the supercapacitor can be charged and discharged. The low R value leads to a maximum specific power value P_{sp} of 62.66 kW/kg at 160 mA constant current at 2.5 V. A maximum specific energy of 84.19 Wh/kg was reached at a current of 40 mA at 2.5 V. The results from electrochemical characterization in organic electrolyte (1M TEATFB in ACN) using galvanostatic charge-discharge experiments are listed in Table 3.11.

Table 3.11 Results from electrochemical characterization of supercapacitor in organic electrolyte using galvanostatic charge-discharge experiments. The electrodes had an active area of 8 cm^2, with MnO_2 mass of 28.5 mg.

C (mF)	**Mass (mg)**	**J ($mA.cm^{-2}$)**	**C ($mF.cm^{-2}$)**	**(ΔV)**	**E_{sp} ($Wh.kg^{-1}$)**	**R (Ω)**	**P_{sp} ($kW.kg^{-1}$)**
1800	28.5	5	225.0	1	8.77	0.75	11.70
1515	28.5	10	189.4	1	7.38	0.625	14.04
1333	28.5	20	166.6	1	6.50	0.625	14.04
2448	28.5	5	306.0	2	47.72	1	35.09
2244	28.5	10	280.5	2	43.74	0.75	46.78
2201	28.5	20	275.1	2	42.90	0.687	51.07
2764	28.5	5	345.5	2.5	84.19	1	54.82
2633	28.5	10	329.1	2.5	80.20	0.937	58.51
2587	28.5	20	323.4	2.5	78.80	0.875	62.66

CHAPTER IV

DEVELOPMENT of 3D MICROPATTERNED MnO_2/CNT SUPERCAPACITOR ELECTRODES ON SILICON SUBSTRATE

In this chapter, work done on supercapacitors based on three dimensional micropatterned electrodes. These microelectrode arrays were fabricated using conventional silicon microfabrication techniques and hot-filament CVD process for CNT synthesis. Electrochemical technique was used to achieve direct deposition of MnO_2 on the vertically aligned CNT array. The 3D structures improve MnO_2 dispersion on CNT and allow for enhanced mobility of the electrolyte to access the interior of the porous CNT/MnO_2 microelectrodes. Material analysis and characterization were performed using scanning electron microscope (SEM). Charge storage performance was evaluated by electrochemical techniques such as cyclic voltammetry (CV) and galvanostatic charge/discharge measurement.

4.1 Design and Fabrication of the Microelectrode Array

Structuring the electrodes in a 3D platform offers higher effective surface area for the same footprint of devices compared to thin film and 2D interdigitated electrodes. This fact has been schematically illustrated on the left in Figure 4.1. By using conventional silicon microfabrication techniques, such supercapacitors can be easily integrated with other devices such as sensors to get the energy storage/delivery system on the same chip, thus improving overall device performance and further shrink the size. The 3D design improves the accessibility of the cations allowing greater use of the high specific surface

area which was not possible in the planar, macro electrodes. In addition to that, the thin film coating of MnO_2 reduces the solid-state diffusion length for the cations and also provides for facile electron transfer kinetics between the MnO_2 and the CNT current conductors. The poor conductivity of bulk MnO_2 that limits high power application can be overcome by using this novel approach. By fabricating the electrodes in an interdigitated structure, the need for a separator is eliminated which further improves the performance for high power applications [109]. This 3-D nanostructured design provides the efficient design for MnO_2 electrodeposition as represented by the schematic seen on the right in figure 4.1.

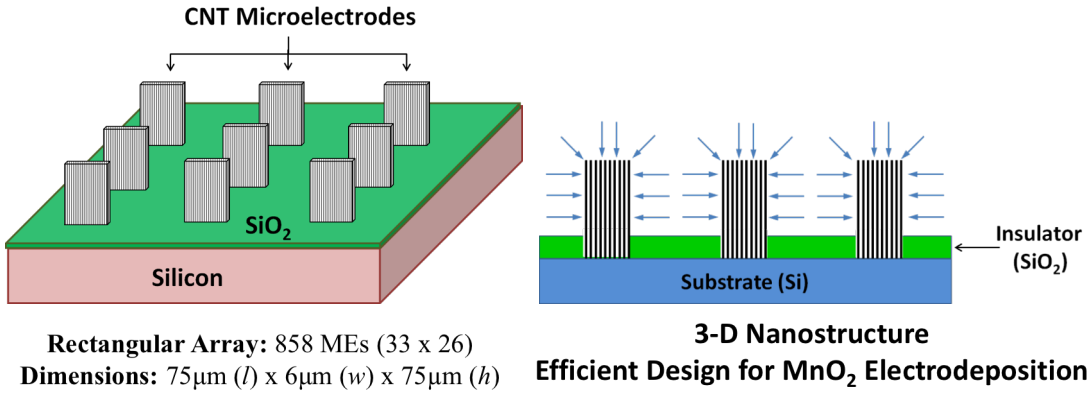

Figure 4.1 Left; Schematic 3D view of a MnO_2/CNT supercapacitor in form of a microelectrode array isolated by the SiO_2 layer; Right- The open 3D structure of the microelectrode array provides better access to the CNTs to allow multidirectional deposition of MnO_2, unlike planar electrodes.

The fabrication process starts with a highly doped n-type silicon substrate (0.005 Ω-cm), 550µm thick, that was first thermally oxidized to form a thin-layer of SiO_2 (0.5µm). The photoresist AZ54214E was used for conventional UV photolithography process to define the array layout. PR AZ54214E was spin coated on the substrate with

initial speed of 1000 rpm (5 sec) and then accelerated to 3000 rpm and held for 30 s. Then, the substrate was baked for 135 sec at 100°C on a hotplate. The baked photoresist was patterned with a UV photolithography step in a Cobilt mask-aligner to define the array layout. After developing the pattern, the exposed SiO_2 regions were etched using a buffered oxide etch (BOE) solution and rinsed with DI water. Thin-films of the buffer layer (Ti) and the catalyst (Co) were sputtered using DC sputtering technique. After photo-resist lift-off, vertically aligned multi-walled CNTs were grown using hot-filament CVD process with methane as the carbon gas source. The height of the CNTs was controlled by varying the duration of CH_4. The fabrication steps of the CNT array structure are schematically presented in Figure 4.2.

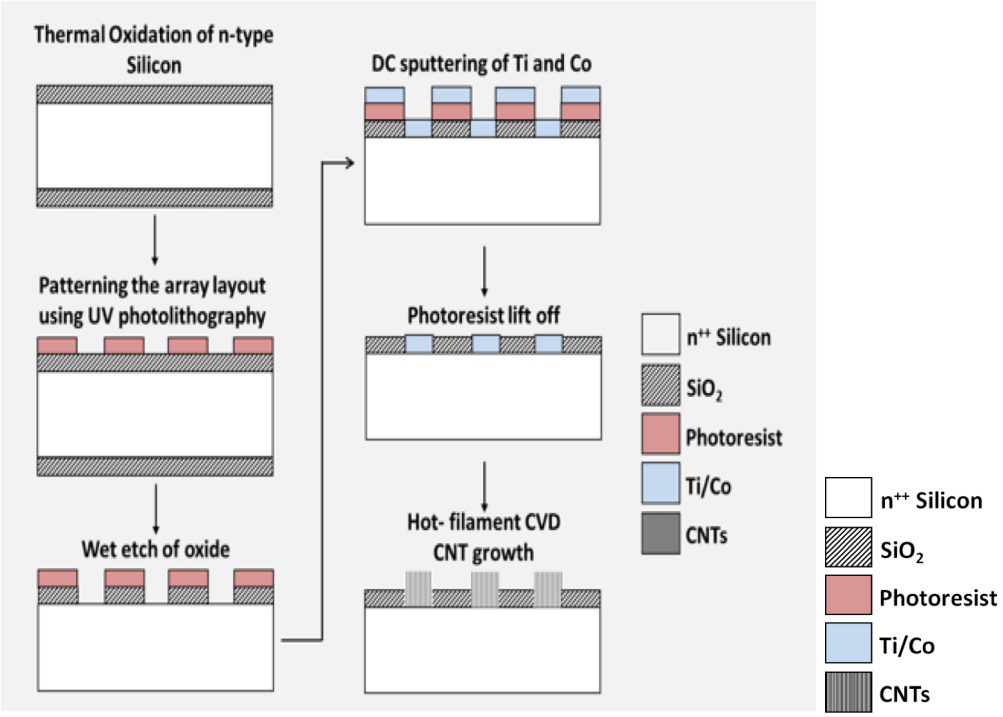

Figure 4.2 Process flow for fabricating 3D microelectrode array.

The characterization and material analysis were performed by scanning electron microscope (SEM). The cross-sectional SEM micrographs in figure 4.3(a) and (b) show SEM images of the array with ~75µm tall CNTs on the silicon substrate isolated by the SiO_2 layer from a tilt or perspective view and the top view. This process can be adapted to fabricate arrays with different geometries and dimensions. Deposition of MnO_2 on the CNT array was achieved by direct electrochemical reduction of $KMnO_4$. The SEM image in figure 4.3 (c) shows the MnO_2 coated CNTs' array. A high resolution SEM image in figure 4.3 (d) shows the porous microstructure of the MnO_2.

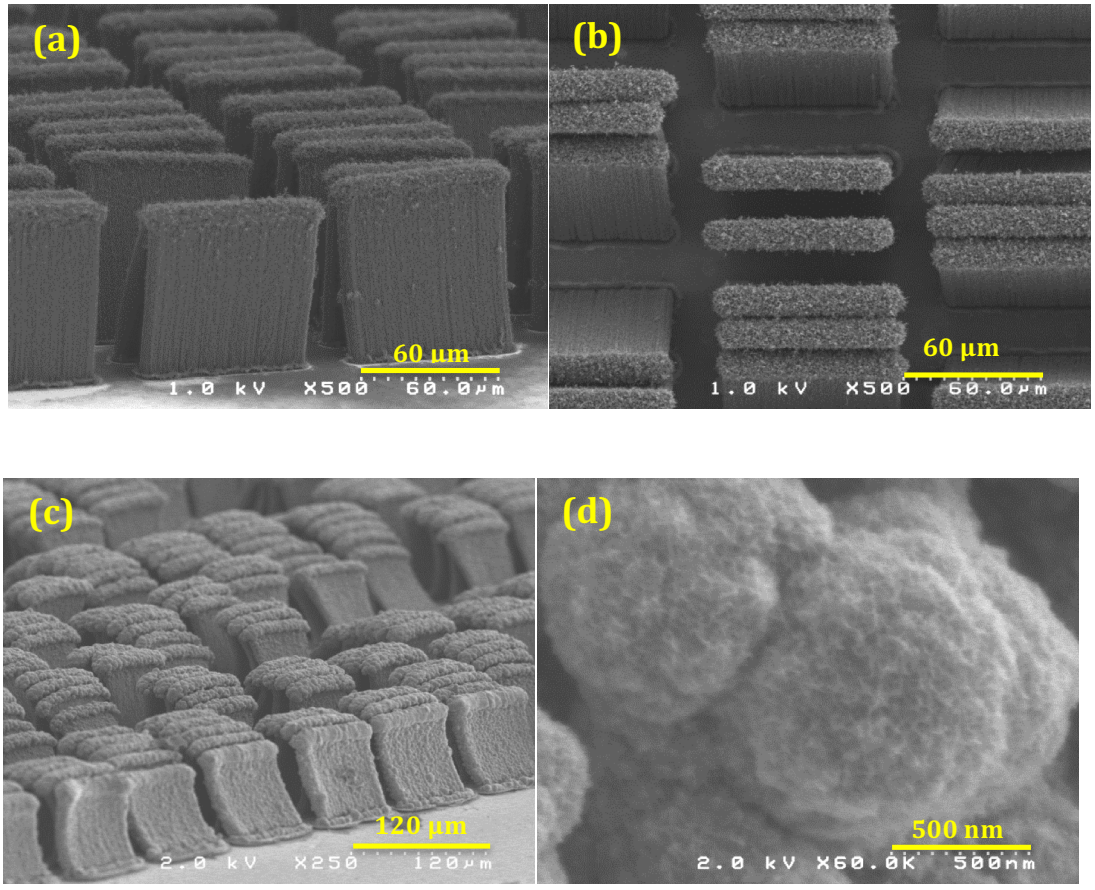

Figure 4.3 The microelectrode array consisting of vertically aligned CNTs with SiO2 insulation layer from (a) a tilt or perspective view and (b) the top view; (c) the final array structure after electrochemical deposition of MnO_2 onto the CNTs and (d) high resolution SEM micrograph showing the porous microstructure of MnO_2.

4.2 Electrochemical Characterization of the Microelectrodes Array – Results and Discussion

Electrochemical characterization of the CNT/MnO_2 array electrode was performed in a flat cell using cyclic voltammetry in a 3 electrode configuration with 0.1M KCl as the supporting electrolyte. Platinum wire was used as the counter electrode with a Ag/AgCl reference electrode. The main charge storage mechanism of the MnO_2/CNT supercapacitor is attributed to the pseudocapacitive reactions occurring due to inter/deintercalation of electrolyte cations in MnO_2. Cyclic voltammograms were recorded in a 0-1V potential window for different MnO_2 film thicknesses.

The cyclic voltammograms recorded at 50mV/s showed an enhancement in the pseudo-capacitive currents with increase in MnO_2 thickness, as seen in figure 4.4 (a). The variation of capacitance with MnO_2 thickness calculated from the CVs can be seen in figure 4.4 (b). A high value of capacitance, 1.8 F/cm^2 or in volumetric terms, 240 F/cm^3, was achieved which represented more than ***200x*** enhancement in the electrode capacitance due to the addition of MnO_2 can be seen in figure 4.4 (c). These results highlight the advantages of using the advanced 3-D nanostructured MnO_2/CNT microelectrode arrays.

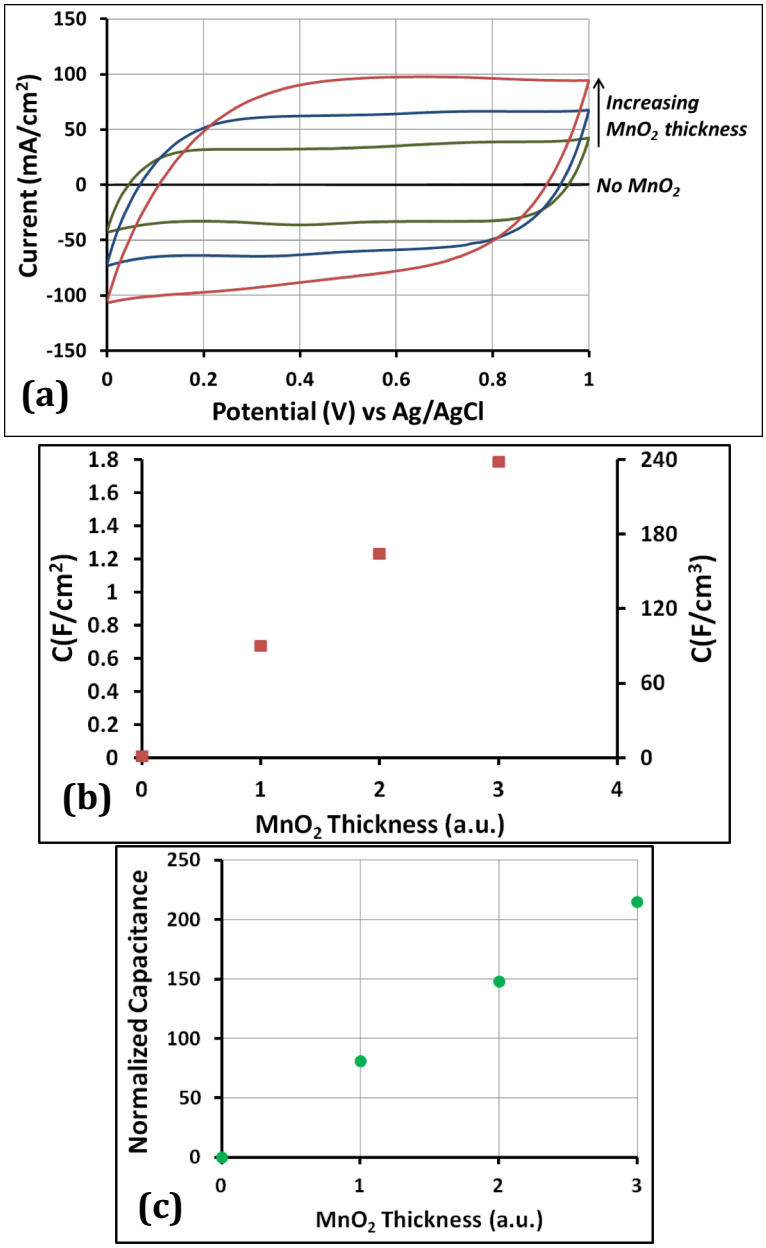

Figure 4.4 (a) CVs recorded at 50 mV/s in KCl for the MnO_2/CNT MEA before and after different MnO_2 thickness; (b) Capacitance variation as a function of the MnO_2 thickness showing a high capacitance value of 1.8 F/cm^2 or 240 F/cm^3; (c) Normalized capacitance as a function of MnO_2 thickness showing a 200x improvement in capacitance over just a CNT MEA.

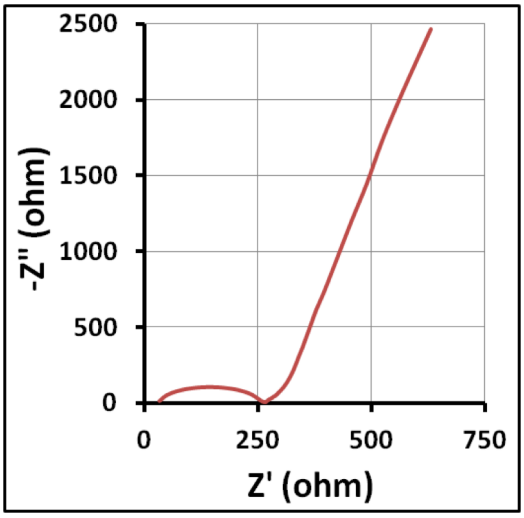

Figure 4.5 Nyquist plot recorded for the supercapacitor in 1M TEATFB in Acetonitrile using A.C. Impedance Spectroscopy showing a high ESR value of 260Ω.

Figure 4.5 shows the Nyquist plot of the supercapacitor recorded between 0.01 Hz and 100 kHz frequency range with an amplitude of 5 mV. The plot shows a high equivalent series resistance (ESR) value of 260 Ω.

Figure 4.6 shows results from galvanostatic charge and discharge experiments for microelectrode array in 0.1M KCl as supporting electrolyte at different current densities: 5mA/cm^2, 10mA/ cm^2, 50mA/ cm^2 and 100mA/ cm^2. As shown in Fig 4.6, all charge–discharge curves are a non-ideal triangular shape at various current densities, which is a typical characteristic of pseudocapacitors due to redox process.

The capacitance of the MnO_2/CNT microelectrode arrays was calculated from the slope of the discharge curve and the resistance was calculated from the potential drop of the initial part of the discharge curve for galvanostatic measurement. The highest capacitance for the MnO_2/CNT microelectrode arrays was obtained at 5mA/cm^2: 1.85 F/cm^2, or 246.7 F/cm^3.

The charge-discharge curves recorded at the different current densities can be seen in figure 4.6. Results from the charge-discharge experiments have been tabulated in table 4.1.

Table 4.1 Results from constant current charge-discharge experiments using MnO_2/CNT microelectrode arrays in 0.1 M KCl.

Current Density (mA/cm^2)	**C (F/cm^2)**	**C (F/cm^3)**	**ESR (Ω)**
5	1.85	246.7	668
10	1.78	237.7	598
50	1.42	189.3	554
100	1.15	153.3	502

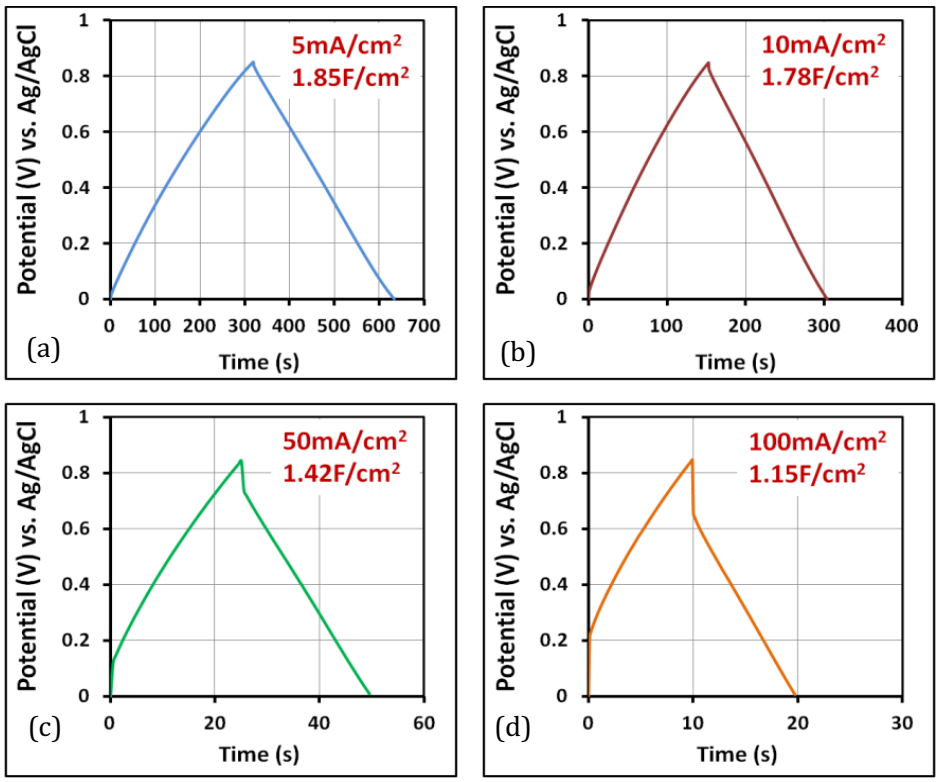

Figure 4.6 Constant current charge discharge curves recorded at different current densities (a) 5 mA/cm^2or 1.85 F/cm^2; (b) 10 mA/cm^2or 1.78 F/cm^2; (c) 50 mA /cm^2or 1.42 F/cm^2; (d) 100 mA/cm^2 or 1.15 F/cm^2.

CHAPTER V

DEVELOPMENT OF MnO_2/CNT SOLID-STATE SUPERCAPACITORS

This chapter describes the work done to fabricate and characterize high performance flexible solid-state supercapacitors based on 3D nanostructured MnO_2/CNTs microelectrode arrays and solid state electrolytes using spin coating and conventional methods. The planar and 3D patterned CNT electrodes were fabricated on graphite substrates using hot filament chemical vapor deposition (HF-CVD) to grow carbon nanotubes (CNTs). Electrochemical deposition technique was used for MnO_2 deposition, as described in chapters 3 and 4. Initial experiments consist of investigation of the influence of spin coating deposition parameters such as thickness based on spinning speed, and duration. The roadmap to achieve the final device is presented in this chapter.

Electrochemical characterization of the CNT electrodes was first performed in 0.1 M KCl aqueous electrolyte in symmetric configuration to evaluate the performance of each electrode in order to correlate the design to the corresponding capacitance. In the next stage, solid electrolyte performance was evaluated by using macro-supercapacitors, in symmetric configuration. This allowed me to understand and develop the use of solid electrolytes and optimize the parameters including concentrations, thickness and curing conditions. These electrolytes are applied in liquid phase followed by a drying/curing period that turns them solid or gel. After optimizing the solid-state electrolyte on macro electrodes, the final stage involved integrating it with the flexible solid-state supercapacitors. The use of solid electrolytes will promote ease of packaging, without

any risk of leakage and eliminate the risk posed from flammable organic liquid electrolytes.

5.1 Solid-State Supercapacitor Cell Based on CNT Electrodes

5.1.1 Fabrication

Before fabrication of the solid-state supercapacitor cells, preliminary work was performed to experimentally investigate the spin coating parameters such as spinning speed and spinning duration to optimize the surface roughness of solid-state electrolyte on CNT/Graphite substrate.

Spin coating is currently the most popular technique used to produce uniform thin layer films of photosensitive materials with different thicknesses of the order of micrometers and nanometers [110]. Spin coating process has been mainly used in the manufacturing of optical mirrors [111], color television screens [112], integrated circuits and magnetic disk for data storage [113,114].

The spin coating technique's numerous advantages include its low cost, fast operating system, good uniformity, reproducibility and excellent control on film thickness. Its few disadvantages include lesser material efficiency, size restriction, and higher material cost [115,116].

The spin coating can be divided into several key stages sketched in Figure 5.1: fluid deposition, spin-up, spin-off, and finally, evaporation [117]. The spin-off and evaporation process are the stages with the most impact on final coating thickness. The last two stages describe the processes that mostly occur at the same time throughout evaporation and viscous flow [118,119].

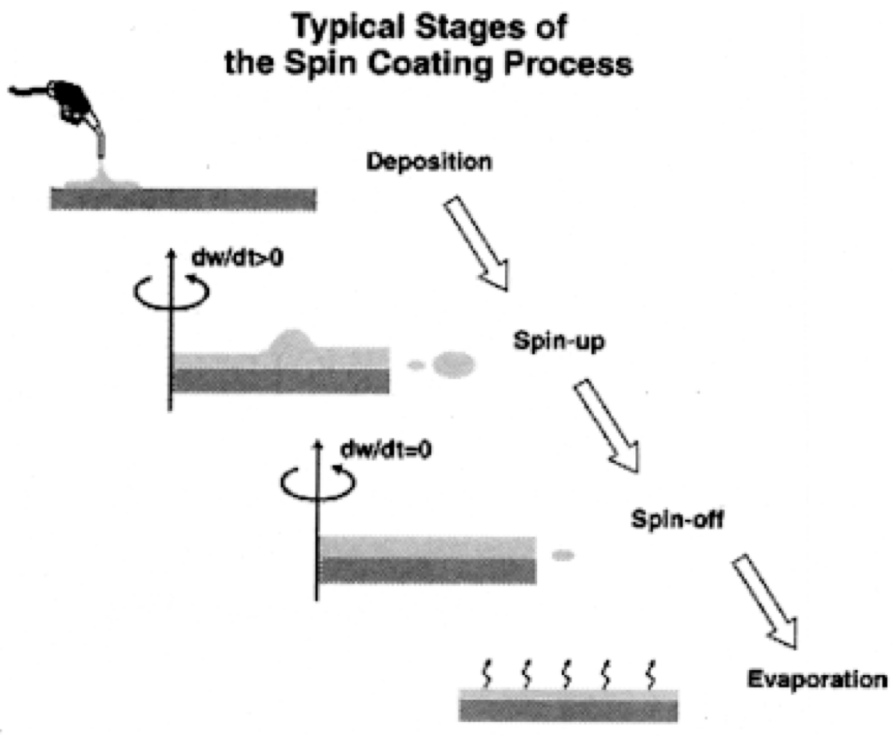

Figure 5.1 Spin coating process [117].

During the deposition stage, electrolyte is allowed to fall on rotating substrates from the syringe (or a dispenser) and the graphite or CNT/graphite substrate is accelerated to the desired speed. The spin-up stage is when the graphite substrate is accelerated to its final rotation speed.

The spin-off is when the graphite substrate is spinning at a constant rate and the degree of centrifugal forces affect fluid thinning behavior. The last stage is when the substrate drying stage begins [120].

In order to investigate the spin coating parameters, the PVA/ H_3PO_4 (1:1) electrolyte solution was directly deposited on the graphite substrate using the spin coating technique. Table 5.1 shows the spin coating parameters used followed by evaluating the surface roughness for each of the experiments.

Table 5.1 Results from the spin coating experiment.

Trial #	Step 1 Spinning speed/Duration	Step 2 Spinning speed/Duration	Results
1	500 rpm/60 sec	2000 rpm/60 sec	Not Uniform
2	750 rpm/60 sec	2000 rpm/60 sec	“
3	500 rpm/60 sec	1000 rpm/60 sec	“
4	200 rpm/60 sec	1000 rpm/60 sec	“
5	200 rpm/30 sec	500 rpm/30 sec	Uniform-Best
6	200 rpm/60 sec	500 rpm/30 sec	“
7	200 rpm/60 sec	500 rpm/45 sec	“
8	100 rpm/60 sec	500 rpm/30 sec	Not Uniform
9	100 rpm/60 sec	500 rpm/60 sec	“
10	300 rpm/60 sec	500 rpm/60 sec	“

Spin coater with speed range 100-5000 rpm and spinning duration up to 120 seconds was used in this experiments and the best parameter was obtained at trail 5.

The electrolyte thickness is one of the key factors that need to be considered before successful fabrication of the solid-state supercapacitor. The electrolyte serves a dual role of providing ionic conductivity while also serving as the ‘separator’ to prevent

an electrical short. The PVA/ H_3PO_4 solid-state electrolyte was tested with planar structure to optimize the electrolyte thickness followed by application in the solid-state supercapacitor for the final work.

Optimizing the electrolyte thickness was the biggest challenge in the second part of the experiment. If the electrolyte is too thin, it usually shorts out the device. If it is too thick then the high cell impedance will limit the high power performance. To overcome this problem, two approaches of the electrolyte fabrication were performed including;

- Enough rest time between each spin coating to provide better incorporation between electrolyte and CNTs
- Building up electrolyte layers with successive spin coating steps until the optimum thickness obtained

In the first approach, vertically aligned multi-walled CNTs (~10 μm - 15 μm tall) were grown using the hot filament thermal CVD process with methane (CH_4) as the carbon gas source. The PVA/ H_3PO_4 (1:1) electrolyte is poured over the CNT/Graphite substrate with a waiting period of 5,10, and 60 minutes to allow the solution to settle into the CNT network, followed by spin coating at 200rpm for 30 sec and 500rpm for 30 sec. This process is repeated three times and the sample is then left at room temperature approximately 16 hours to dry.

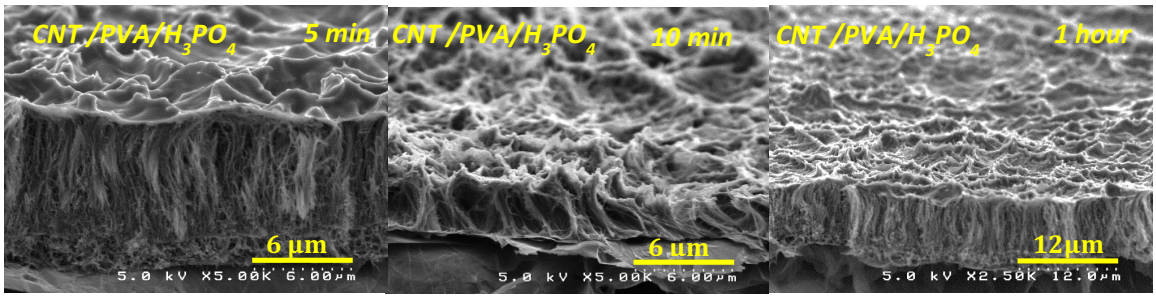

Figure 5.2 SEM images showing the cross-section of the electrodes with deposited solid-electrolyte on CNTs. Different waiting period during the spin coating process; (5min-left), (10 min-middle), and (60min-right).

Figure 5.2 shows the SEM micrographs of the three test electrodes with the deposited solid electrolyte. The SEM micrographs show there is no significant difference between waiting period of 10, and 60 minutes. However, the longer waiting period made the electrode more fragile and soft, which made it hard to handle. The shortest waiting period with electrolyte gave worse electrolyte coating and it was also visually seen during the experiments. Each pair of electrodes fabricated under same conditions were then sandwiched together and tested. Symmetric cells with these electrodes were shorting out. Based on this, the conclusion was the thicker electrolyte coating was required to avoid an electrical short.

In the second approach, three-part spin coating steps were performed to overcome the shorting problem and create effective electrolyte layer in a supercapacitor test cell. On the first day, the electrolyte is poured over the electrode with a waiting period of 10 minutes, followed by and spin coating at 200rpm for 30 sec and 500rpm for 30 sec. This is repeated twice more. The sample is then left at room temperature to dry. On the second day, the spin coated repeated at 200rpm for 30 sec and 500rpm for 30 sec with no waiting period in between repetitions for a total of five times. The sample is once again left at

room temperature to dry. When the sample is dry, the final spin coating step is performed at 1000 rpm for 30 seconds; this last step yields a barrier or separator layer on the substrates that will prevent any electrical short. The electrodes are then sandwiched together and tested. Symmetric cells with these electrodes were not shorting out. The effective electrolyte thickness of 10 μm was obtained after the final step as shown in the SEM micrograph in Figure 5.3.

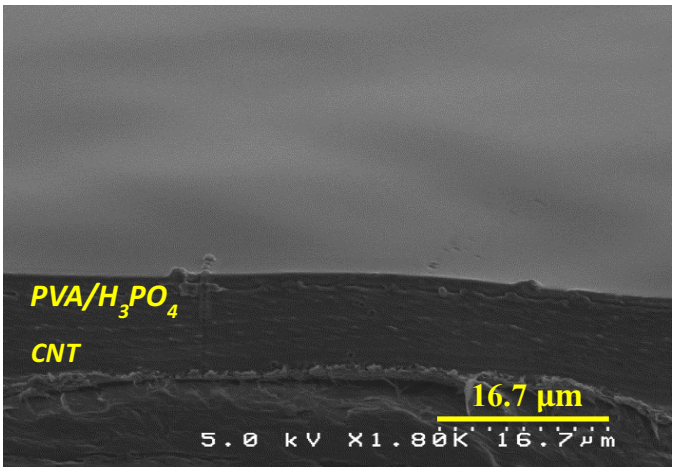

Figure 5.3 SEM image of CNT electrode with solid polymer electrolyte.

Another key factor that need to be considered before successful fabrication of the supercapacitor is electrolyte concentration. The research on solid-state supercapacitors with the solid polymer electrolyte is quite minimal. Most of the publications focused on the fabrication process of pure solid polymer electrolytes on the electrodes [121-125]. This section offers a step by step approach on the experimental preparation and characterization of solid polymer electrolytes and integrating it with the solid-state supercapacitors.

An aqueous solution of PVA was prepared by mixing PVA with distilled water in the ratio of 1:10 by mass. This solution was heated at 60 °C with magnetic stirring for four hours to completely dissolve the PVA in the distilled water. This is followed by mixing H_3PO_4 with the PVA aqueous solution in the percentage of 90:10, 80:20, 60:40, 50:50, 30:70, 20:80, and 10:90. This has been summarized in Table 5.2. The percentage of the H_3PO_4 was calculated the following equation;

$$x\% = \frac{\mathrm{n}}{n+5} \times \%100 \qquad 5.1$$

where x is the percentage of H_3PO_4, and n is the value of H_3PO_4 in grams.

The mixture is heated at 70 °C with magnetic stirring for 12 hours to form a homogeneous solution. The resulting solution is allowed to cool down to room temperature and then put inside the glass beaker to avoid contamination from the environment for further experimental tests.

Table 5.2. Solid-State electrolyte preparation parameters.

Electrolyte Solution	**PVA mass (g)**	**H_3PO_4 mass (g)**	**Percentage of H_3PO_4**
S1	5	0.55	10
S2	5	1.25	20
S3	5	3.325	40
S4	5	5	50
S5	5	11.6	70
S6	5	20	80
S7	5	45	90

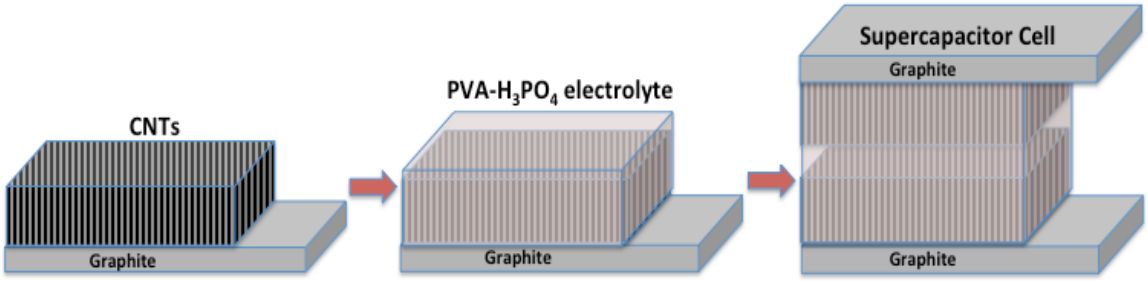

Figure 5.4 Schematic of the fabrication process of a solid-state supercapacitor assembled in sandwich configuration. Vertically aligned CNTs were grown on the graphite substrate (Left). Solid-State electrolyte was applied to the electrodes by spin coating method (Middle). The electrodes were sandwiched together using hydraulic pressure (Right).

The electrolyte was applied to both the electrodes by spin coating and sandwiched together using hydraulic pressure before the curing step as shown in the schematic in Figure 5.4. This was followed by electrochemical characterization to evaluate the device performance.

5.1.2 Electrochemical Characterization – Results and Discussion

The first electrochemical characterization test of supercapacitors was conducted after a 72 hour waiting period and was performed at CHI 660 C workstation. All cyclic voltammetry (CV), galvanostatic charge/discharge and electrochemical impedance spectroscopy (EIS) profiles of solid-state supercapacitors showed very inconsistent results. These results showed that the short curing period is not enough to solidify the solid polymer electrolyte in solid-state supercapacitors. Longer curing period is required for more hydrolyzing of water and better incorporation of electrolyte with electrode.

The second electrochemical characterization test of supercapacitors was performed after 16 days curing time at room temperature. The cyclic voltammetry was recorded at 10 $mV.s^{-1}$ and expressed as current ($mA.cm^{-2}$) versus voltage (V). Figure 5.5

(a) shows the overlaid CV curves of the solid-state supercapacitors containing different concentration of H_3PO_4 (%10, 20, 40, 50, 70, 80, and 90) in the solid electrolyte.

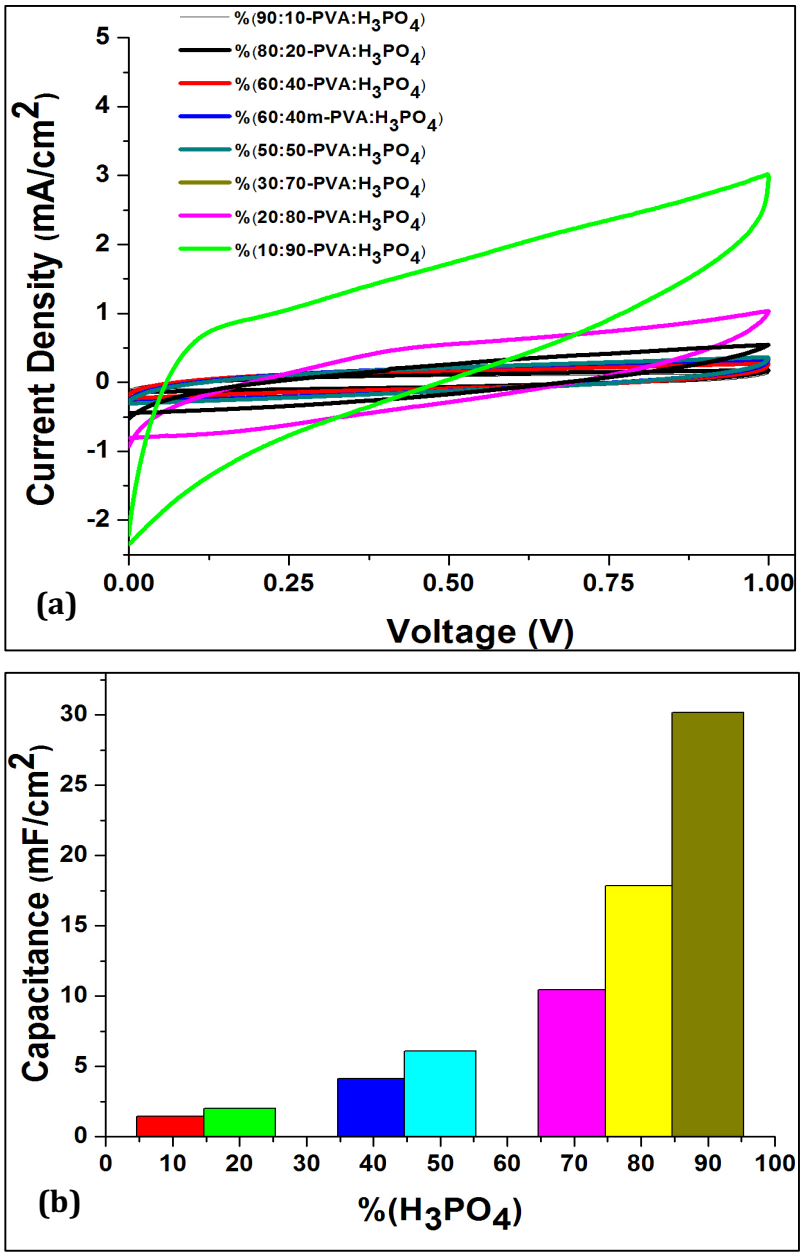

Figure 5.5 Electrochemical characterizations of solid-state supercapacitors with different concentrations of H_3PO_4 PVA electrolytes. (a) CV curves at 10 mV/s ; (b) Calculated capacitance vs. H_3PO_4 concentration.

All CV curves retain nearly rectangular shapes indicating the capacitive behavior from double layer formation The total capacitance of the supercapacitors was calculated at 10 mV/s scan rate from the CV curves using the following equation.

$$C_T = \frac{1}{2} \times \frac{1}{v(Vf - Vi)} \int_{Vi}^{Vf} I(v)dV \qquad 5.2$$

where C_T is the total capacitance (F), $\int_{Vi}^{Vf} I(v)dV$ is the area of the CV curve, (V_f-V_i) is the potential voltage window, and ν (V/s) is the scan rate.

The highest capacitance of 30.18 mF.cm^{-2} was achieved in the solid-state supercapacitor with a 90% of H_3PO_4 in solid electrolyte. These values decreased to 1.44 mF.cm^{-2} with 10% of H_3PO_4 in solid electrolyte as shown in figure 5.5 (b).

Galvanostatic charge/discharge measurements were also used to characterize the performance of the solid-state supercapacitors. As shown in Figure 5.6, all the galvanostatic charge/discharge curves are close to triangular shape at a current density of 0.625 mA.cm^{-2}, indicating the typical capacitive behavior and charge balance between the electrodes.

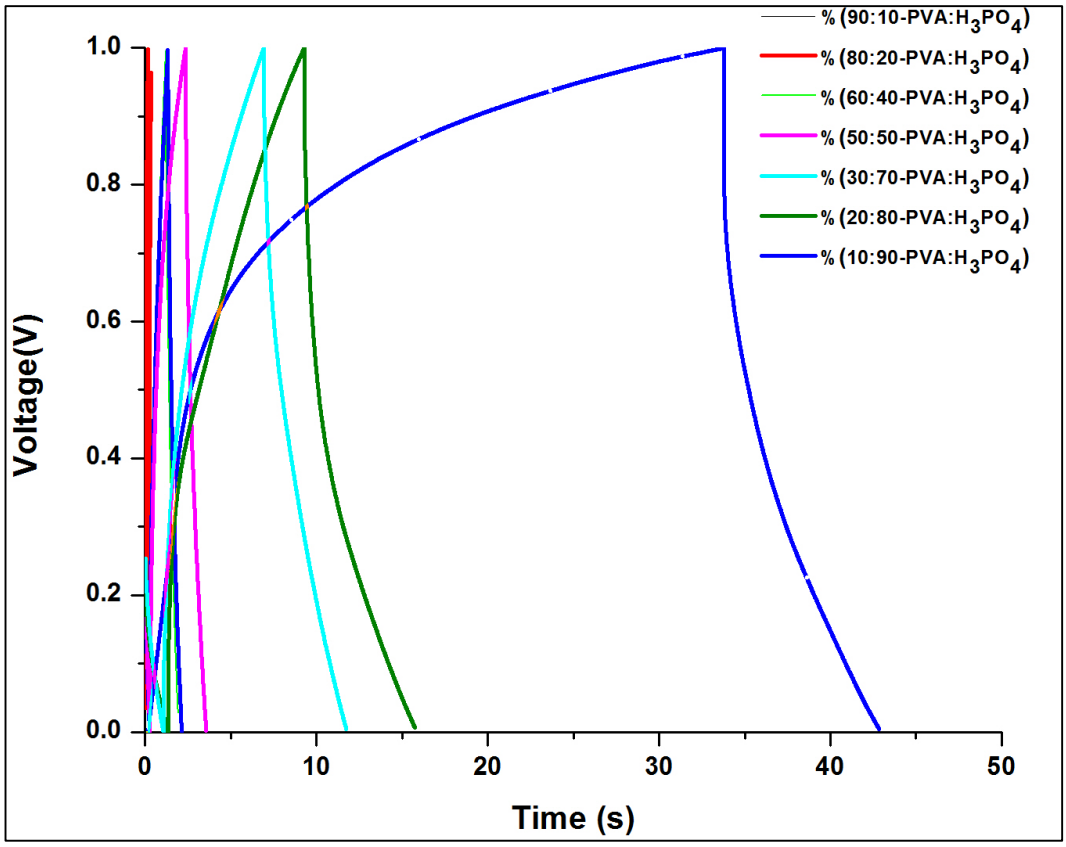

Figure 5.6 Overlaid galvanostatic charge/discharge curves at 0.625 mA.cm^{-2}.

In addition, the ionic conductivity of the electrolyte is a critical factor in determining the electrochemical performance of the supercapacitors [126,127]. If the electrolyte has high ionic conductivity, it supports rapid ion transport between the electrodes, which results in the high power and energy density. The ionic conductivity (σ) of solid polymer electrolyte can be estimated using impedance spectra and applying the following equation.

$$\sigma = \frac{L}{R_b \times A} \qquad 5.3$$

where the L (cm) is the distance between the two electrodes, A (cm^2) is the total contact area of the electrolyte and electrodes, and R_b (Ω) is the bulk resistance.

The thickness of the supercapacitors was measured three times at different parts of the cell and average thickness was calculated using a digital micrometer. Figure 5.7 (a-g) shows the Nyquist plot of the supercapacitor cells scanned in the frequency range between 0.01 Hz and 100 kHz with an A.C. amplitude of 5 mV. The calculated R_b for all the seven supercapacitors were determined by extrapolating the curves on the Nyquist plots to intersect the x-axis.

The highest ionic conductivity was 3.93×10^{-3} $S.cm^{-1}$ for the S7 supercapacitor which has the highest H_3PO_4 concentration of 90 wt. % and while the lowest ionic conductivity was 3.76×10^{-5} $S.cm^{-1}$ for the S1 supercapacitor with 10 wt. % of H_3PO_4. This results clearly demonstrates that as the acid concentration increased, the conductivity increase several orders of magnitude and further supports the enhanced the performance of the device with 90 wt. % of H_3PO_4. Details of calculated R_b and conductivity of the solid-state electrolytes has been summarized in Table 5.3. This is lower compared to that obtained 0.1 M KCl solution (at 25^oC) NIST data : 1.28×10^{-2} $S.cm^{-1}$.

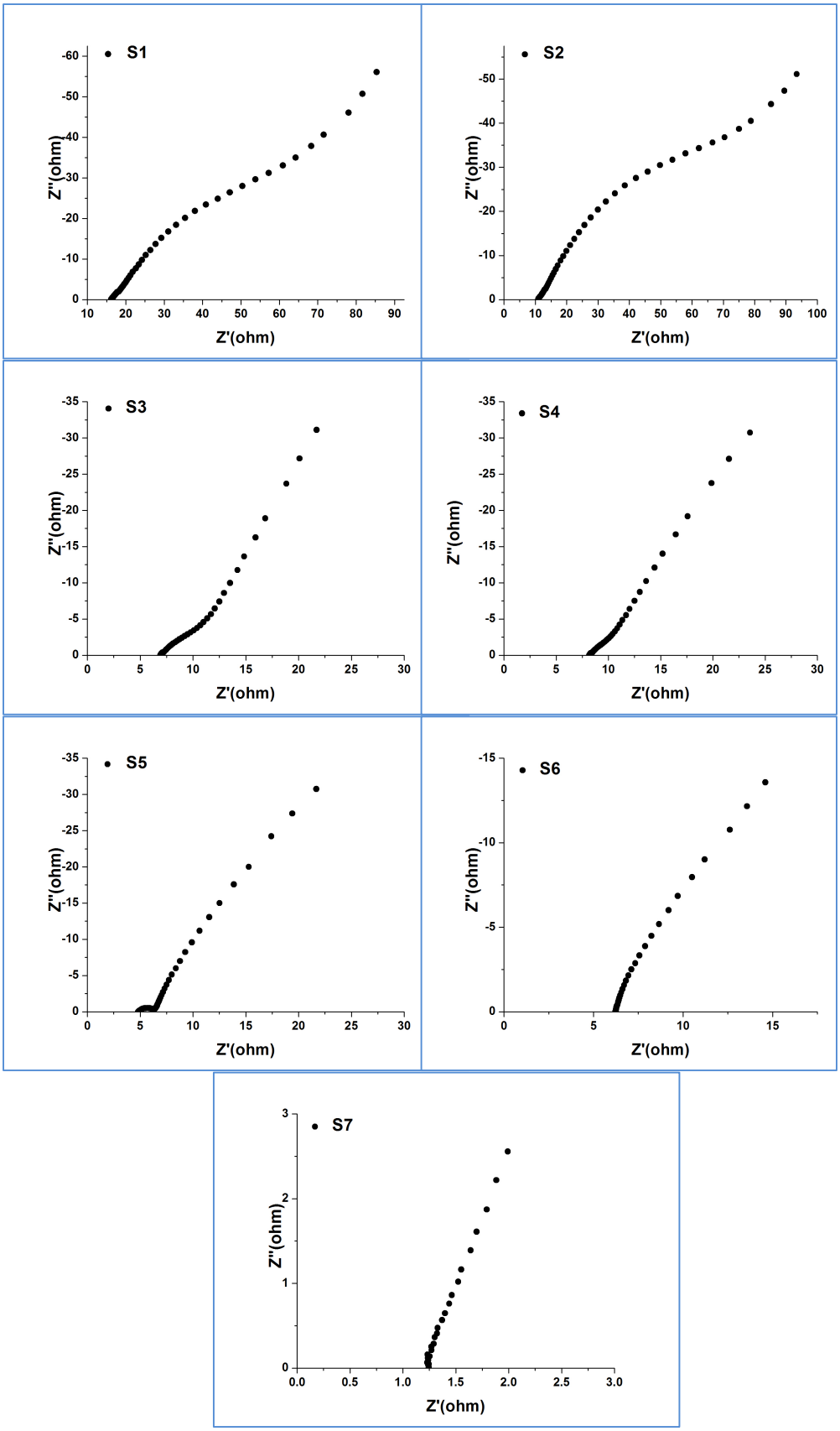

Figure 5.7 Nyquist plots recorded for test cells in the frequency range of 0.01 Hz -100 kHz.

Table 5.3 Conductivity results for different concentration of solid-state electrolyte.

Electrolyte Solution	Percentage of H_3PO_4	Thickness (mm)	R_b (Ω)	σ (Scm^{-1})
S1	10	0.046	15.26	$3.76x10^{-5}$
S2	20	0.066	10.07	$8.19x10^{-5}$
S3	40	0.110	8.89	$1.54x10^{-4}$
S4	50	0.123	7.65	$2.09x10^{-4}$
S5	70	0.176	6.75	$3.26x10^{-4}$
S6	80	0.256	5.20	$6.1x10^{-4}$
S7	90	0.346	1.1	$3.93x10^{-3}$

5.2 Solid-State Supercapacitor Cell Based on CNT/MnO_2 Electrodes

5.2.1 Fabrication

Solid-state supercapacitors based on vertically aligned CNT arrays and solid-state electrolytes demonstrated consistent capacitive behavior and a low equivalent series resistance (ESR) as discussed in the previous section. However, energy storage is only limited to the double layers formed at electrolyte-electrode interfaces and the maximum specific capacitance can typically only reach 10-40 F/g or 10-40 $\mu F/cm^2$. However, in the work reported in this dissertation, in section 5.1, I have achieved much higher capacitance values of nearly 30 $mF.cm^{-2}$.

In contrast to the charge storage mechanism of EDLCs, pseudocapacitors store energy by faradaic reactions involving electron transfer that follow reduction-oxidation (redox) reactions and intercalation processes [128]. The most commonly used pseudocapacitive materials are: (i) conducting polymers and (ii) transition-metal oxides.

Conductive polymer pseudocapacitors have disadvantages over metal oxide based pseudocapacitors in terms of long-term stability, cost and cycle life, which limits their commercial potential. Among transition-metal oxides, manganese oxide (MnO_2) has been regarded as the most appealing electrode materials for the next generation of electrochemical supercapacitors (ES) because of its outstanding capacitive performance, abundance, environment-friendliness and low price.

The major motivation of this work is to combine the high pseudocapacitance of MnO_2 film with the high electrical conductivity and high surface area-to mass- ratio of CNT arrays to achieve extraordinary capacitors, and combine these electrodes with PVA/H_3PO_4 solid polymer electrolytes for integration into a solid-state supercapacitor cells, without any additives or binders.

In this work, the graphite foil (127μm) substrates were cleaned with acetone and then dried with compressed air for 15-20 sec. Then, a titanium (Ti ~45nm) buffer layer was deposited followed by cobalt (Co ~7 nm) as the catalyst, using a Cressington 308R DC magnetron sputtering system. Vertically aligned CNTs (~5 μm - 15μm tall) were grown using hot filament thermal CVD process with methane as the carbon gas source. The procedure of CNT growth is similar to the one described in previous sections. The substrates used had an active area of 3.5cm x 2cm and 2cm x 2 cm tabs for electrical contacts.

Electrochemical deposition of manganese dioxide (MnO_2) on the CNTs was achieved by direct reduction of 10 mM potassium permanganate ($KMnO_4$) in de-ionized water (18MΩ-cm) using a CH Instruments CHI660C potentiostat. The deposition was carried out in a flat cell using cyclic voltammetry in a standard three electrode

configuration. Platinum (Pt) foil was used as the counter electrode with a Ag/AgCl reference electrode. The CV parameters used for this step consisted of 30 cycles at 0.1V/s in a potential window of -1V to +1V and 120s intervals between each cycle.

The highest ionic conductivity solid polymer electrolyte, containing 90 wt. % of H_3PO_4, was chosen as the solid-state electrolyte for supercapacitors in this work. The solid electrolyte was applied to both the electrodes by spin coating at 200rpm for 30 sec and 500rpm for 30 sec and sandwiched together using hydraulic pressure at 250 psi. The curing time of the solid polymer electrolyte can be changeable due to environmental conditions such as relative humidity or addition of other materials.

5.2.2 Electrochemical Characterization – Results and Discussion

The electrochemical characterization of the solid-state supercapacitor, including cyclic voltammetry (CV), galvanostatic charge-discharge, and electrochemical impedance spectrometry, were performed after drying for 3, 9, 16, and 21 days at room temperature and results are summarized in table 5.4. The calculation methods for capacitance and impedance are similar to the one described in previous sections, based on equation 5.2. These results clearly demonstrate that 16 days curing time is enough to solidify the electrolyte.

Table 5.4 Results from characterization test for supercapacitor.

Curing Time →	**3 days**	**9 days**	**16 days**	**21 days**
Capacitance (mF) (CV- 100 mV/s)	72.12	82.617	88.14	88.12
Impedance (Ω) (0.01Hz-100 KHz)	2	1.8	1.7	1.7

The efficient coating of MnO_2 on CNTs is also necessary for the development of advanced MnO_2-CNT supercapacitors. Therefore, in this experiment, the various electrochemical deposition cycles were used to maximize MnO_2 coverage on CNTs and thereby the capacitance. The preparation of the samples and the procedure of CNT growth are similar to the one described in previous sections. Electrochemical deposition of manganese dioxide (MnO_2) on the CNTs was achieved by direct reduction of 10 mM potassium permanganate ($KMnO_4$) in de-ionized water (18MΩ-cm). The CV parameters used for this step consisted of various cycles at 0.05 V/s in a potential window of -1V to +1V and 120s interval between each cycle. The mass of MnO_2 was determined by weighing the substrate on a microbalance, before and after MnO_2 deposition. Parameters for MnO_2 deposition and the resulting mass have been summarized in table 5.5.

Table 5.5 Parameters for MnO_2 deposition using 50 mV/s scan rate and resulting MnO_2 mass for 12 substrates.

Sample #	CV Cycles	Substrate Mass Before MnO_2 (mg)	Substrate Mass After MnO_2 (mg)	MnO_2 Weight (mg)
S1	15	238.3	245.6	7.3
S2	15	231.2	238.0	8.6
S3	30	234.5	243.9	9.4
S4	30	227.9	238.1	10.2
S5	60	225.3	233.2	7.9
S6	60	229.2	241.8	12.6
S7	**15**	**240.2**	**248**	**7.8**
S8	**15**	**244.8**	**252.6**	**7.8**
S9	**30**	**235.7**	**247.0**	**11.3**
S10	**30**	**226.5**	**237.8**	**11.3**
S11	**60**	**231.3**	**247.9**	**16.3**
S12	**60**	**232.6**	**249.6**	**16.3**

Due to some experimental difficulties, the mass loading of MnO_2 in the electrode was not consistent for some samples even with the same number of deposition cycles. A new experimental setup was used to overcome this problem. The substrates were easily sliding off from the Teflon holder during the deposition steps, so it was replaced with a glass slide to provide better support for the substrates**.** The electrodes S7 and S8 (15 cycles), S9 and S10 (30 cycles), and S11 and S12 (60 cycles) were chosen to further fabricate the three solid-state supercapacitors cells. The electrodes S7 and S8 are labeled as supercapacitor cell TR1, the electrodes S9 and S10 are labeled as supercapacitor cell TR2, and the electrodes S11 and S12 are labeled as supercapacitor cell TR3. The solid polymer electrolyte, containing 90 wt. % of H_3PO_4, was applied to both the electrodes by spin coating and sandwiched together using hydraulic pressure before the curing step, as described previously. After 16 days curing time, electrochemical characterization including CV, galvanostatic charge-discharge, and electrochemical impedance spectrometry, were performed for the all solid-state supercapacitors cells at room temperature. The total capacitance of the supercapacitors was calculated at 10 mV/s scan rate from the CV curves, based on equation 5.2.

The specific capacitance of the solid-state supercapacitor cell based on total MnO_2 mass can be calculated by the following equation.

$$C_{sp}\left(\frac{F}{g}\right) = \frac{C_T}{m_T} \qquad 5.4$$

where C_{sp} is the specific capacitance (Fg^{-1}), C_T is the total capacitance, and m_T is the total mass of MnO_2 on the two electrodes.

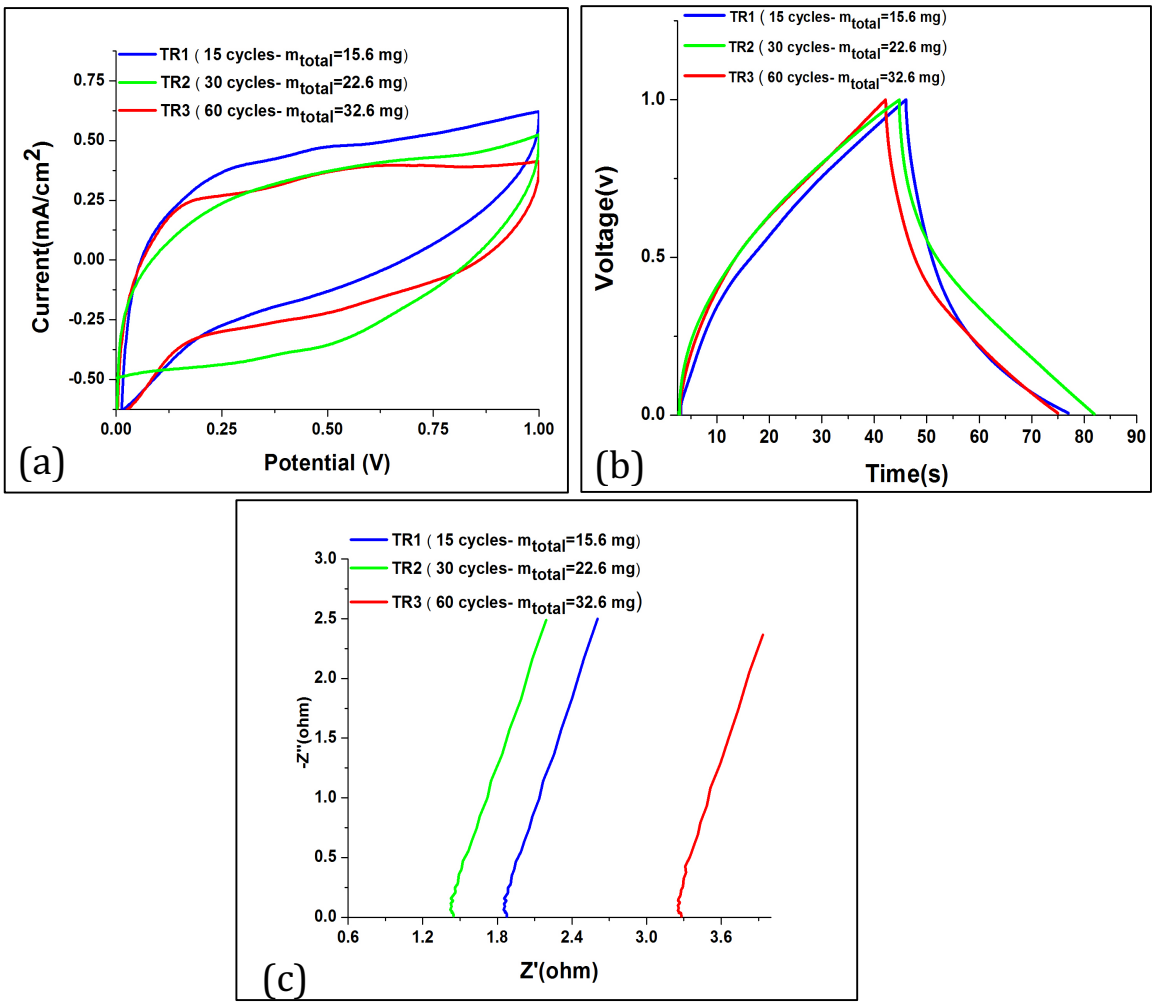

Figure 5.8 Electrochemical characterization of solid-state supercapacitor cells. (a) Cyclic voltammograms recorded at 10 mV/s. (b) Galvanostatic charging/discharging curves for solid-state supercapacitors at 0.625mA/cm^2. (c) The Nyquist plot recorded for solid-state supercapacitors in the frequency range of 0.001 Hz-100 kHz.

Figure 5.8 (a) CV curves show the ideal pseudocapacitive nature of MnO_2 and the fast oxidation-reduction (redox) reaction with PVA/H_3PO_4 solid electrolyte. The highest specific capacitance of 17.30 F.g^{-1} was achieved at a scan rate of 10 mV/s with supercapacitor TR2.

Galvanostatic charge/discharge measurements were used to characterize the performance of the solid-state supercapacitor cells. The capacitance of the solid-state

supercapacitors was calculated from the slope of the discharge curves and the calculation method is similar to the one described in previous chapters. The supercapacitor TR2 exhibited the highest capacitance of 190 mF at a constant discharge current of 0.625 mA/cm^2 and overlaid graphs from all the cells are shown in Figure 5.8 (b).

Figure 5.8 (c) shows the Nyquist plot of the solid-state supercapacitors in the frequency range of 0.001 Hz-100 kHz. The lowest ESR recorded was for TR2, 1.4 Ω, which is a very low value for the solid-state supercapacitors.

These results suggest that the optimum mass loading of MnO_2 can be achieved with 30 cycles at 0.05 V/s in a potential window of -1V to +1V and 120s intervals between each cycle.

The maximum operating potential window is another important parameter for the supercapacitors which can yield greater energy and power densities. The supercapacitor cell TR2 was chosen for the experimental test and the device demonstrates a maximum working potential window of 1.5V shown in Figure 5.9. This operating potential window is far wider than previously reported solid-state supercapacitors [129-131] and is comparable to some of the asymmetric solid-state supercapacitors [132-134].

Figure 5.9 shows the CV curves of the supercapacitor TR2 at the scan rate of 5 mV/s within the potential window of 0-1V and 0-1.5V. The quasi-rectangular shape of the CVs indicates the capacitive behavior of the solid-state supercapacitor. The maximum specific capacitance of 21.31 $F.g^{-1}$ was obtained at a scan rate of 5 mV/s within 0-1.5V.

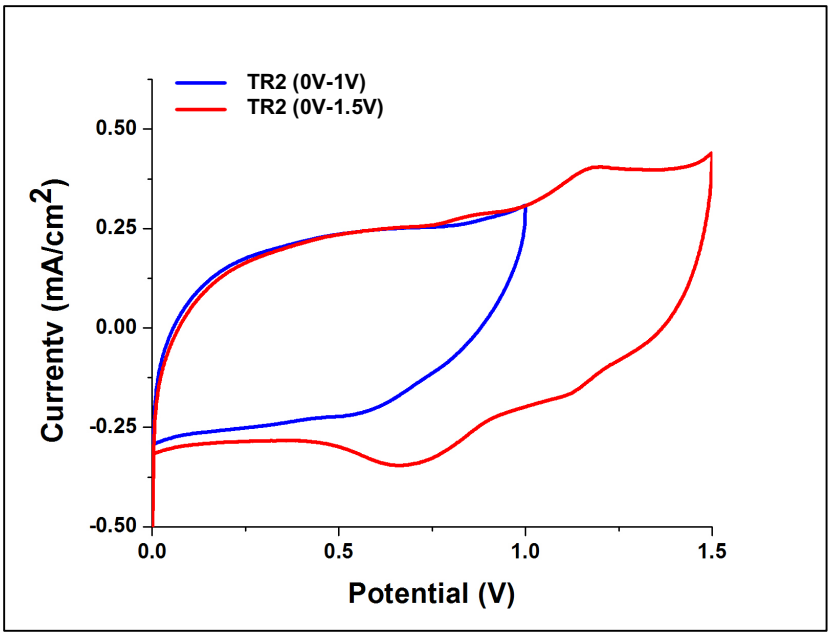

Figure 5.9 CV curves of supercapacitor TR2 at different operating windows 0 to 1.5V at scan rate of 5mv/s.

The solid-state supercapacitors based on CNT/MnO_2 electrodes and solid-state electrolytes were successfully fabricated and characterized using the spin coating method discussed in the previous section. However, there are some drawbacks including:

1. The CNT height doesn`t result in higher specific capacitance due to poor MnO_2 coverage in the interior of the CNT network.
2. Excess MnO_2 might limit specific capacitance due to increased resistance and hinder cation diffusion.
3. The planar structure limits MnO_2 dispersion on CNTs and does not allow for enhanced mobility of the electrolyte to access the interior of the porous CNT/MnO_2 macroelectrodes.

In order to overcome these drawbacks, vertically aligned CNTs were grown shorter than before and a new 3D nanostructured CNT/MnO_2 micro electrode array were fabricated for the supercapacitors.

In the first approach, planar macro electrodes with shorter CNTs were fabricated and tested in this experiment. Vertically aligned CNTs (~3 μm - 6 μm tall) were grown using the hot filament thermal CVD process with CH_4 as the carbon gas source. The procedure of CNT growth is similar to the one described in previous sections.

Electrochemical deposition of MnO_2 was achieved using parameters discussed in table 5.5. In the final step, a solid-state supercapacitor cell was fabricated and the electrochemical characterization test performed. The electrochemical characterization test result was compared with the previous results. The highest specific capacitance was 17.1 $F.g^{-1}$ at a scan rate of 2 mV/s. This is very similar to the previous supercapacitor cell. These results suggest that this approach may not improve the specific capacitance of the solid-state supercapacitors.

In the second approach, the 3D nanostructured CNT/MnO_2 micro electrodes were fabricated and tested. The 3D design improves the accessibility of the cations, allowing greater use of the high surface area, which was not possible with the planar macro electrodes. In addition to that, the thin film coating of MnO_2 reduces the solid-state diffusion length for the cations and also provides for facile electron transfer kinetics between the MnO_2 and the CNT current conductors. This 3-D microelectrode array provides an efficient design for MnO_2 electrodeposition as represented by the schematic seen in figure 5.10.

A perforated brass foil (406µm thick) with opening of 406µm diameter and 660µm pitch was used as a shadow mask to create array layout on the graphite foil substrate. Thin layers of titanium (Ti ~45nm) as a buffer layer followed by cobalt (Co ~7nm) as the catalyst were deposited on the graphite foil substrates with the metal shadow mask on top using a Cressington 308R DC magnetron sputtering system. Electrochemical deposition of MnO_2 was used as mentioned in section 5.2.2. More detailed fabrication will be discussed in the next section.

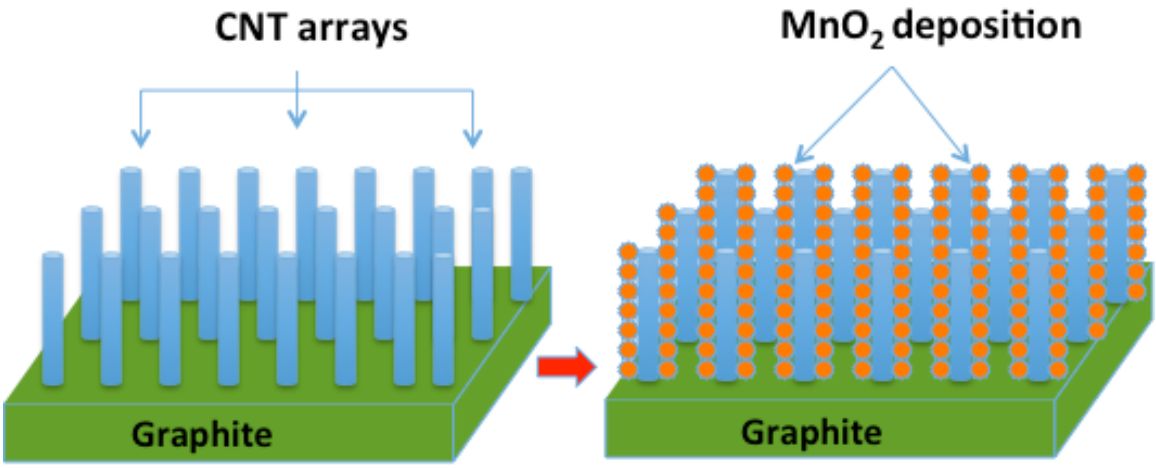

Figure 5.10 Left; Schematic 3D view of a CNT electrode; Right-Schematic 3D view of a CNT/MnO_2 electrode.

The optimum CV parameters for MnO_2 deposition were 3 cycles at 0.05 V/s in a potential window of -1V to +1V and 120s intervals between each cycle. After the electrochemical deposition of MnO_2, the solid electrolyte was applied to both the electrodes by spin coating and sandwiched together using hydraulic pressure and then electrochemical characterization test was performed. The solid-state supercapacitor was labeled as TR4 for this experiment.

Figure 5.11 shows the CV curve of the supercapacitor TR4 at a scan rate of 1 mV/s within a potential window of 0-1V. The quasi-rectangular shape of the CV indicates capacitive behavior of the solid-state supercapacitor. The supercapacitor TR4 has the specific capacitance of 110 $F.g^{-1}$ which is almost 7*x* times higher than that observed for the planar structured solid-state supercapacitors. These results highlight the advantages of using the advanced 3-D nanostructured MnO_2/CNT microelectrodes.

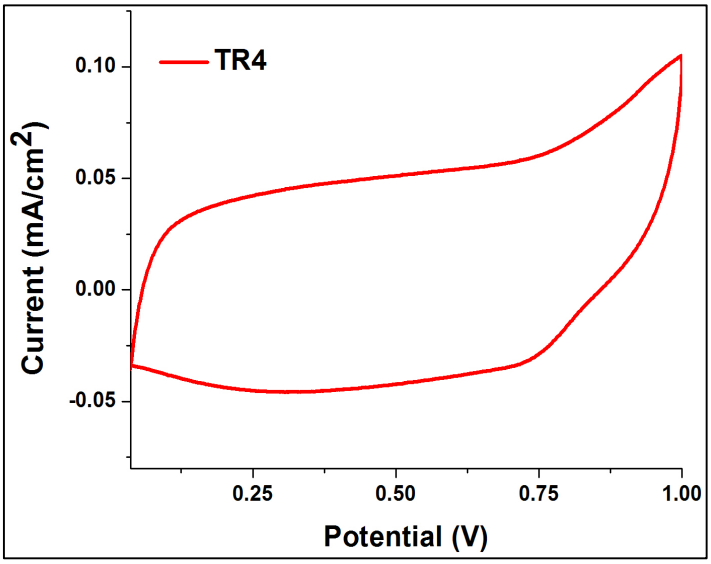

Figure 5.11 CV curve of supercapacitor TR4 at scan rate of 1mv/s at operating voltage windows 0 to 1V.

Following the above experiments, it was realized that the solid electrolyte, when in liquid phase, was etching the MnO_2 and which was responsible for the severely reduced specific capacitance. More experiments were performed subsequently with an increased PVA to phosphoric acid ratio, including trials at 90:10, 60:40, 50:50, and 40:60. Since there was still etching of the MnO_2 in spite of the reduced acid concentration, the spin coating method was abandoned in favor of a modified solution casting method.

5.3 Solid-State Supercapacitor Cell Based on 3D Nanostructured CNT/MnO_2 Microelectrodes

5.3.1 Fabrication and Material Characterization

The objective of this section was to fabricate a solid-state supercapacitor cell using 3D nanostructured CNT/MnO_2 microelectrode array on highly flexible graphite foil with polyvinyl alcohol-phosphoric acid (PVA-H_3PO_4) gel as the solid electrolyte. Modified solution casting method was used to first fabricate a free-standing partially cured electrolyte layer which is then incorporated in between the electrodes using a hydraulic press.

A perforated brass foil (406µm thick) with opening of 406µm diameter and 660µm pitch was purchased from McMaster-Carr and was used as a shadow mask to create array layout on the graphite foil substrate. The morphologies and microstructure of MnO_2/CNT electrodes were characterized by Hitachi S4200 and Zeiss Merlin scanning electron microscopes.

The fabrication process to achieve the solid state supercapacitor cell can be seen in the schematic flow chart in figure 5.12. First, thin layers of titanium (Ti ~45nm) as a buffer layer followed by cobalt (Co ~7nm) as the catalyst were deposited on the graphite foil substrates with the metal shadow mask on top using a Cressington 308R DC magnetron sputtering system, as seen in figure 5.12(a). The substrates used had an active area of 3.5cm x 2cm and 2cm x 2 cm tabs for electrical contacts. Prior to the sputtering step, the substrates were rinsed with methanol and then dried with compressed air for 20-30 sec.

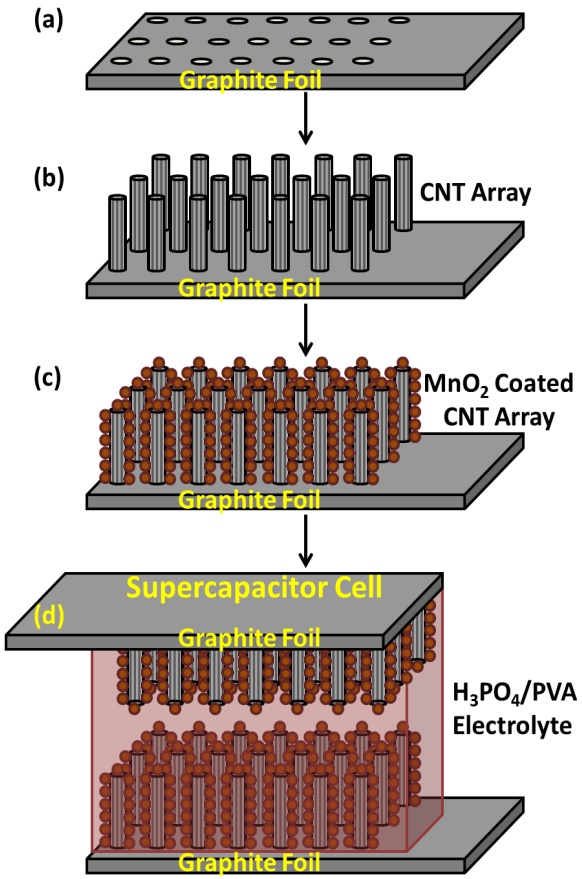

Figure 5.12 Schematic of the fabrication process of a solid-state supercapacitor assembled in sandwich / symmetric configuration.

The 3D array of vertically aligned carbon nanotubes, as seen in the figure 5.12(b) schematic, were grown directly on the graphite foil in a hot filament chemical vapor deposition (HFCVD) system. The substrate was annealed at 520^{o}C for 7 minutes in hydrogen and ammonia (100ppm in N_2) ambient at 15 torr chamber pressure as part of the pre-treatment process. Then, the carbon feed gas, CH_4 was introduced with the tungsten filament at 2000^{o}C with the substrate maintained 2.5 cm below the filament; the CNT growth time was determined by the duration of CH_4 flow for 15 minutes. The gases ratio used in this recipe was 3:1:3 (H_2:CH_4:NH_3).

Controlled electrochemical deposition of manganese dioxide (MnO_2) on the CNTs was achieved by direct reduction of 10 mM potassium permanganate ($KMnO_4$) solution in de-ionized water (18MΩ-cm) without any supporting electrolyte. The deposition was carried out in a beaker using cyclic voltammetry in a standard three electrode configuration with an Ag/AgCl reference electrode and Platinum (Pt) foil as the counter electrode. The CV parameters used for this step consisted of 3 cycles at 0.05V/s in a potential window of -1V to +1V and 120s interval between each cycle. This step yields a 3D supercapacitor electrode as seen in the perspective view in figure 5.12(c). The mass of MnO_2 was calculated by subtracting the electrode mass after the MnO_2 deposition from that recorded previous to that step. Two electrodes were fabricated using this approach with MnO_2 mass of 0.84 mg and 0.81 mg, respectively. Reaction (1) corresponding to MnO_2 deposition can be expressed as follows:

$$MnO_4^- + 2H_2O + 3e^- \rightarrow MnO_2 + 4OH^- \qquad (1)$$

The H_3PO_4/PVA solid electrolyte works as a separator and allows ionic transport between the electrodes of the supercapacitor cell [135-139]. An aqueous solution of PVA was first prepared by dissolving 5 grams of PVA with 50 mL DI water which was heated at 60 °C with magnetic stirring for four hours to completely dissolve the PVA. This was followed by mixing 7.5 grams of H_3PO_4 into the aqueous solution based on specific gravity of 1.70. This ratio of 3:2 (H_3PO_4:PVA) was chosen to achieve a balance in terms of flexibility , ionic conductivity, strength, and curing time. The mixture was heated at 70 °C with magnetic stirring for 12 hours to form a homogeneous solution. The resulting

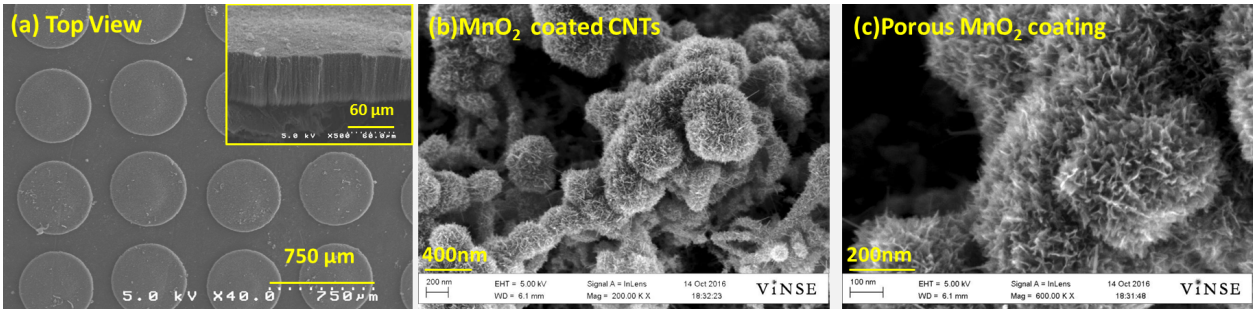

Figure 5.13. (a) Top view of SEM image of the array structure consisting of vertically aligned CNTs on highly flexible graphite substrate. The inset SEM micrograph shows cross-sectional view of the dense CNT growth (~66µm) on the graphite substrate; (b) and (c) High resolution SEM micrographs showing conformal coating of the CNTs with MnO_2 film and porous microstructure of MnO_2.

homogeneous solution was allowed to cool down at room temperature. The electrolyte was cured at room temperature for 15 hours inside a petri dish to avoid contamination. It was then peeled as a free-standing layer from its petri dish. The dimensions of the resulting film were larger than the active area of the electrodes. The film was assembled between the two electrodes and compressed in a hydraulic press at 250 psi. This allowed the electrolyte to infiltrate the 3D MnO_2/CNT network resulting in a solid-state supercapacitor cell as seen in the schematic diagram in figure 5.12(d).

The CNT array layout can be seen from the top-view SEM micrograph in figure 5.13(a), showing individual microelectrodes with a diameter of 530µm and spacing or pitch of 660µm. The diameter is larger than the shadow mask dimensions, probably due to less than optimum contact with the substrate during the sputtering step of Ti/Co metal layers. Inset of figure 5.13(a) shows the cross-section of the sample with vertically aligned CNTs that are ~68µm tall. The high resolution SEM micrographs in figure 5.13(b) shows conformal coating of individual CNTs with MnO_2 film, while the porous microstructure of MnO_2 is distinct from figure 5.13(c), which is beneficial for its application as a supercapacitor. The 3D MnO_2/CNTs nanostructures can maintain their

mesoporous structure, which enhances the accessibility of electrolyte, resulting in excellent rate capability and enhanced specific capacitance. Characterization of the MnO_2 and CNT were also performed using Raman spectroscopy using a DXR Raman Instrument, manufactured by Thermo Scientific, which uses a 532-nm green laser for excitation. The Raman spectra, as seen in figure 3.16, confirms the presence of α-MnO_2.The mass of MnO_2 was determined by weighing the substrate on a microbalance (Denver instruments, APX-100), before and after MnO_2 deposition. Two electrodes fabricated in this work had MnO_2 mass of 0.81 and 0.84 mg, respectively. Manganese dioxide based pseudocapacitors normally have small mass densities (<0.5 $mg.cm^{-2}$) due to their low electrical conductivity ($10^{-6}S.cm^{-1}$), low ion diffusion constant (10^{-12} $cm^2.s^{-1}$), and Mn dissolution into the electrolyte. The unique and highly porous structure of our 3D CNT array electrode allowed a MnO_2 mass loading of 0.12 $mg.cm^{-2}$ by the controlled electrochemical deposition method, but much higher values can be attained with proper optimization of the structure.

5.3.2 Electrochemical Characterization – Results and Discussion

The electrochemical characterization of the solid-state supercapacitor, including cyclic voltammetry (CV), galvanostatic charge–discharge, and electrochemical impedance spectrometry (EIS), were investigated using an electrochemical working station (CHI660C) at room temperature.

Before assembling the solid-state supercapacitor cell, electrochemical characterization of the electrodes was performed using cyclic voltammetry (CV) technique in 0.1M KCl as the supporting electrolyte with platinum foil as the counter electrode and Ag/AgCl reference electrode. Figure 5.14(a) shows the overlaid CVs

recorded for the MnO_2/CNT array electrode at different scan rates (1 $mV.s^{-1}$, 2 $mV.s^{-1}$, 5 $mV.s^{-1}$ and 10 $mV.s^{-1}$) showing nearly rectangular shapes consistent with capacitive behavior. The capacitance of the MnO_2/CNT array electrode was calculated from the CV curves, based on equation 5.2.

The highest capacitance recorded at 1$mV.s^{-1}$ was 721 mF which corresponds to a specific capacitance value of 858 $F.g^{-1}$, in the potential range of 0-1V. The calculated specific capacitance of the MnO_2/CNT array electrode is higher than previous reported values such as Au-doped MnO_2 films (626 F.g-1 at 5 mV.s-1) [140], carbon nanoparticles/MnO2 nanorods (800 F.g-1 at 5 mV.s-1) [141], Co3O4/Pt/MnO_2 (539 F.g-1 at 1 A.g-1) [142], MnO_2/s-MWNT (392.1 F.g-1 at 2 mV.s-1) [143], Ag/PANI/ MnO_2 (800 F.g-1 at 1 mA.cm-2) [144], and MnO_2/SnO_2 (367.1 F.g-1 at 50 mV.s-1) [145]. The Nyquist plot from the A.C. impedance spectroscopy scanned between 0.01Hz and 100 kHz and a 5mV amplitude can be seen in figure 5.14(b). The equivalent series resistance (ESR) is determined by the intersection of the plot with the real axis (x-axis), which in this case is 6.1Ω.

The specific energy and specific power for the single electrode was calculated according to equations (5.5) and (5.6), respectively:

$$E_{sp}\left(\frac{Wh}{kg}\right) = \frac{1}{2}\,\frac{C_T V^2}{3600\, m_T} \qquad (5.5)$$

$$P_{sp}\left(\frac{W}{kg}\right) = \frac{V^2}{4Rm_T} \qquad (5.6)$$

where E_{sp} (Wh/kg) is the specific energy, P_{sp} (W/kg) is the specific power, C_T (F) is the total capacitance, R(Ω) is the equivalent series resistance (ESR) from the Nyquist plot or DC resistance from the charge-discharge curve , m_T is the total mass of MnO_2 in kg, and V is the potential window. The maximum specific energy of 119.2 $Wh.kg^{-1}$ was achieved at a scan rate of 1 $mV.s^{-1}$ in a potential window of 0-1V while the maximum specific power was 48.8 $kW.kg^{-1}$.

Additional characterization of the MnO_2/CNT array electrode was performed in 0.1M KCl using galvanostatic charge/discharge measurements using different currents- 5mA (6 $A.g^{-1}$ or 0.7$mA.cm^{-2}$), 10mA (12 $A.g^{-1}$ or 1.4 $mA.cm^{-2}$), and 20 mA (24 $A.g^{-1}$ or 2.8 $mA.cm^{-2}$). Figure 5.14(c) show overlaid curves from the charge-discharge experiments at different currents for the voltage window ranging from 0-1 V. All the galvanostatic charge/discharge curves are a non-ideal triangular shape at various current densities, indicating the typical characteristic of pseudocapacitors during the charging and discharging process.

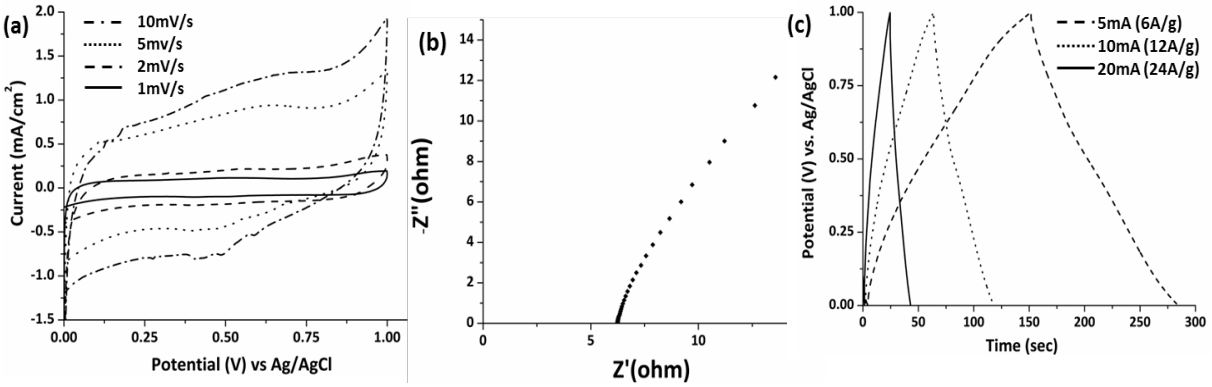

Figure 5.14. Electrochemical characterization of the 3D MnO_2/CNTs array electrode on highly flexible graphite; (a) Overlaid cyclic voltammograms recorded at different scan rates ranging from 1 to 10 mV/s and expressed as Current (mA/cm^2) versus potential (V) vs. Ag/AgCl; (b) Nyquist plot obtained from scanning between 0.01Hz to 100kHz; (c) Overlaid curves from galvanostatic charge and discharge experiments for MnO_2/CNTs electrode at various current densities.

The capacitance was calculated from the slope of the discharge curves as seen in equation (5.7), where C_T (mF) is the total capacitance, I (mA) is the discharge current, ΔV (V) is the discharge potential drop and Δt (s) is the discharge time.

$$C_T(mF) = \frac{I\ (mA)}{\frac{\Delta V\ (V)}{\Delta t\ (s)}} \qquad (5.7)$$

The D.C. resistance R (Ω) was calculated from the potential drop of the initial part of the discharge curves as seen in equation (5.8), where, ΔV (V) is the initial potential drop in the discharge curve and I (A) is the discharge current:

$$R(\Omega) = \frac{\Delta V\ (V)}{I\ (A)} \qquad (5.8)$$

The highest capacitance obtained was 692mF at 5mA current, which corresponds to specific energy of 114 $Wh.kg^{-1}$ and while the highest specific power of 75.1 $kW.kg^{-1}$ was obtained at a discharge current of 20 mA in the potential window of 0-1V, which is higher than a similar system reported previously using carbon based materials/MnO_2 [146-149].

This was followed by assembling/fabrication of the flexible solid-state supercapacitor cell and characterized to determine its electrochemical charge storage performance, in a symmetric configuration. The cyclic voltammograms (CV) recorded at different scan rates ranging from 1-10 $mV.s^{-1}$ and expressed as current ($mA.cm^{-2}$) versus potential (V) can be seen in Figure 5.15 (a). As expected, the shape and symmetry of the CV curves show the ideal pseudocapacitive nature of MnO_2 and the fast oxidation-reduction (redox) reaction with PVA/H_3PO_4 solid electrolyte. We however do observe a set of oxidation (0.65V) and reduction (0.11V) peaks at $1mV.s^{-1}$, which corresponds to

the anion intercalation ↔ deintercalation reaction on the surface and the bulk of MnO_2 film. These peaks are not seen at higher scan rates due to slower reaction kinetics. A capacitance of 1369 mF was obtained at $1mV.s^{-1}$ which decreased to 262 mF at $10mV/s^{-1}$. The specific capacitance for the supercapacitor cell based on total MnO_2 mass of 1.65 mg was nearly 830 $F.g^{-1}$ at the lowest scan rate of $1mV.s^{-1}$. These values decreased to 727 mF and 441 $F.g^{-1}$ at 2mV/s, respectively.

A.C. impedance spectroscopy test also was performed to evaluate the electrochemical behavior of the solid-state supercapacitor cell. Figure 5.15 (b) shows the Nyquist plot of the solid-state supercapacitor cell scanned between 0.01Hz and 100 kHz. In this case the equivalent series resistance (ESR) can be determined by the intersection of the plot with the real axis (x-axis), which is 2.05Ω. A low value of ESR in this solid-state supercapacitor cell can be attributed to the interconnected network of highly conductive CNTs within the MnO_2 in combination with a thin layer of the solid state electrolyte-separator. Summary of the results using the solid-state supercapacitor cell from the cyclic voltammetry and the AC impedance experiments can be seen in table 5.6.

Table 5.6. Solid-state supercapacitor cell- Summary of results from the cyclic voltammetry and AC impedance experiments for the cell with active area of 7 cm^2, MnO_2 mass of 1.65 mg, potential window of 1 V and an ESR value of 2.05 Ω. The specific power is 73.9 $kW.kg^{-1}$.

Scan Rate ($mV.s^{-1}$)	**C (mF)**	**C ($mF.cm^{-2}$)**	**E_{sp} ($Wh.kg^{-1}$)**
1	1369	195.5	115.2
2	727	103.8	61.2
5	405	57	34.1
10	262	37.4	22.1

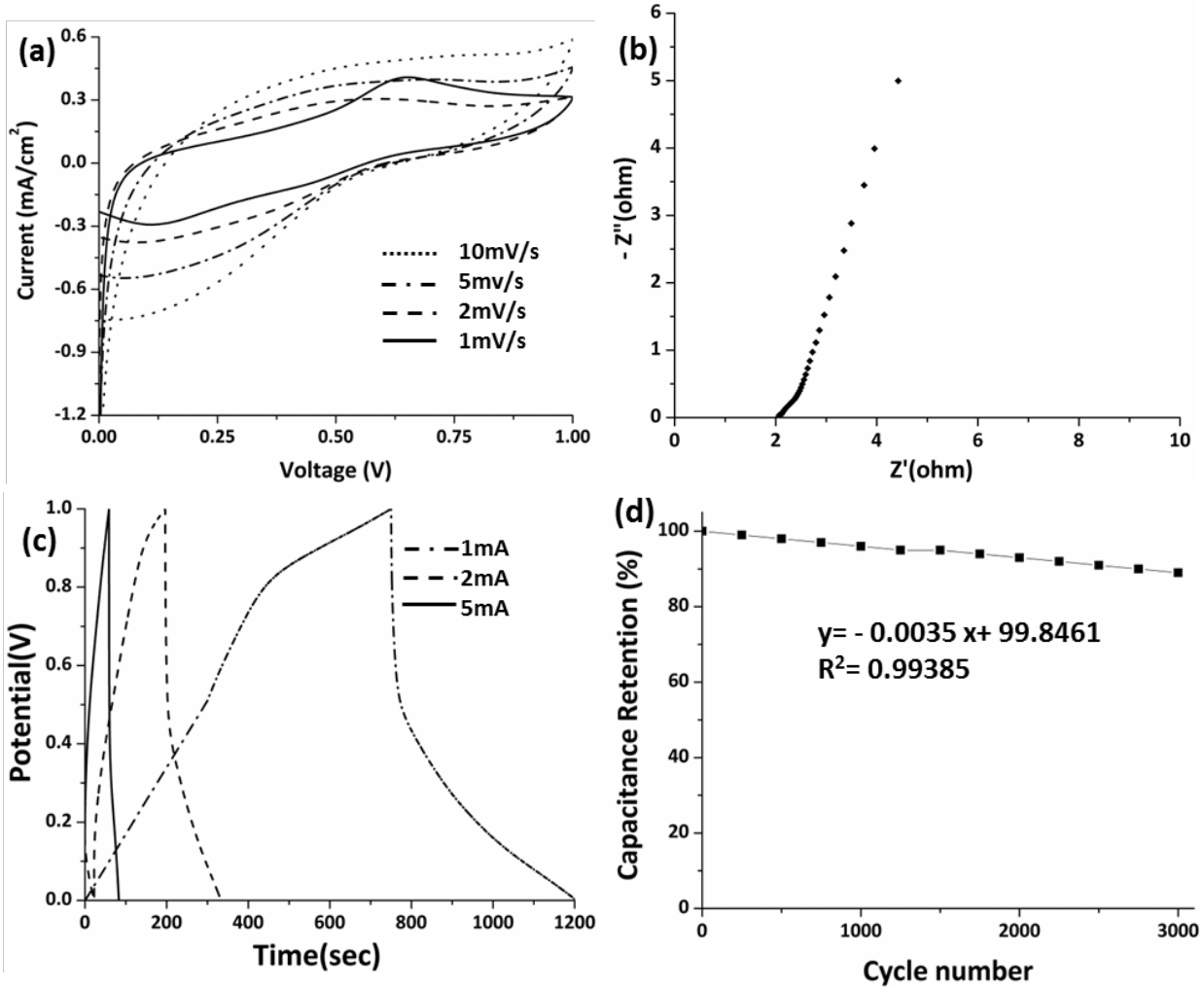

Figure 5.15. Electrochemical characterization of the flexible solid-state supercapacitor cell; (a) Overlaid cyclic voltammograms recorded at different scan rates ranging from 1 to 10 mV/s. and expressed as current (mA/cm^2) versus potential (V); (b) Nyquist plot recorded for solid-state supercapacitor cell in the frequency range of 0.001Hz-100KkHz; (c) Overlaid galvanostatic charging/discharging curves for the solid-state supercapacitor cell at different currents; (d) Cycling stability of supercapacitor device at 20mA over 3000 cycles as calculated by the % capacitance retention.

Galvanostatic charge/discharge measurements were also used to characterize the performance of the solid-state supercapacitor cell. The graph in figure 5.15 (c) shows results from these experiments at different currents - 1mA (0.14mA.cm^{-2}), 2mA (0.28 mA.cm^{-2}), and 5 mA (0.7 mA.cm^{-2}) for the voltage window of 0-1 V. All charge–discharge curves are of non-ideal triangular shape, which is a typical characteristic of pseudocapacitors due to the pseudocapacitive redox process. The discharge capacitances and the corresponding DC resistance values were calculated using equations 5.9 and 5.10.

The highest capacitance obtained was 520 mF at a constant discharge current of 1mA or 0.14 mA.cm^{-2} which drops to 326mF at 20mA discharge current. The maximum specific energy of 43.8 Wh.kg^{-1} was obtained at a current of 1 mA in the same potential window while the highest value of specific power, 38.3 kW.kg^{-1} was obtained at 20mA discharge current. Results from the galvanostatic charge-discharge experiments, including at 20mA current, have been summarized in table 5.7.

Table 5.7: Solid-state supercapacitor cell- Summary of results from the galvanostatic charge discharge experiments for the cell with active area of 7 cm^2, MnO_2 mass of 1.65 mg and potential window of 1 V.

C (mF)	I (mA)	C (mF.cm^{-2})	E_{sp} (Wh.kg^{-1})	R (Ω)	P_{sp} (kW.kg^{-1})
520	1	74.3	43.8	5.6	27.1
480	2	68.6	40.4	4.8	31.6
410	5	58.6	34.5	4.2	36.1
326	10	46.6	27.4	3.96	38.3

Cycling stability of the supercapacitor cell is a critical factor for practical applications. This was evaluated by running a constant current charge-discharge test at a current density of 20 mA or 2.9 mA.cm^{-2}. The solid-state supercapacitor maintains 89% of the initial capacitance after 3000 cycles showing a stable performance, as seen in the

plot in Figure 5.15 (d). Using a linear data fitting function and extrapolating the capacitance retention to 80%, we can predict the number of cycles this cell would require, which is 5760. This number is much higher than conventional lithium batteries and can be further improved by optimizing the CNT structure, the MnO_2 deposition and mass loading and the fabrication process of the solid-state polymer electrolyte/separator component.

As summary, a solid-state supercapacitor cell consisting of 3D nanostructured MnO_2/CNT array electrodes on highly flexible graphite foil and H_3PO_4/PVA composite as a solid-state electrolyte/separator were successfully fabricated and characterized. The 3D MnO_2/CNT array electrode structure provides several advantages including supporting rapid reversible redox kinetics, facile charge transfer, shorter ion diffusion lengths, absence of additives or binders, high mass loading of MnO_2 and high specific surface area resulting from the mesoporous MnO_2/CNT network. The H_3PO_4/PVA composite solid-state electrolyte supports ionic transport while simultaneously serving as the separator between the electrodes of the solid-state supercapacitor cell. The electrochemical characterization results yield a very high capacitance value of 1.4 F at $1mV.s^{-1}$ from the solid-state supercapacitor cell corresponding to a specific energy value of 115.2 $Wh.kg^{-1}$ and a specific power value of 73.9 $W.kg^{-1}$. Constant current charge-discharge experiments yielded 520mF capacitance at 1mA current providing specific energy value of nearly 44 $Wh.kg^{-1}$, while higher specific power of 38 $W.kg^{-1}$ was obtained at 20mA discharge current. Excellent cycle life was also obtained with more than 89% capacitance retention after 3000 cycles at 20mA current. This work demonstrates that feasibility and benefits of 3D nanostructured MnO_2/CNT array

electrodes which can be easily incorporated into solid-state supercapacitors cells. The technology can be scaled up to fabricate more safety, flexible supercapacitors while providing high power and energy densities, thus making them promising candidates for wearable electronics, renewable energy storage technology, and portable electronics such as roll up displays and photovoltaic cells.

CHAPTER VI

CONCLUSIONS AND FUTURE WORK

In this dissertation, the advanced planar macro supercapacitors, 3D micro supercapacitors, and solid-state supercapacitors have been designed, fabricated, and characterized. The important findings from the research are summarized in this chapter, followed by recommendations for future studies on the supercapacitor technology.

6.1 Conclusions

6.1.1 Planar Macro Supercapacitors

- Vertically aligned multi-walled CNTs have been successfully synthesized by hot filament chemical vapor deposition (HFCVD).
- Ammonia (NH_3) and hydrogen (H_2) have been found to be essential to the growth of CNTs.
- Growing CNT samples with a higher NH_3 flow rate provided higher electrode capacitance compared to those fabricated with lower ammonia rate.
- Multi-walled CNTs can be used as supercapacitors in the form of EDLCs taking advantage of the very high specific surface area: C= ~10mF/cm^2.
- Planar supercapacitor electrodes consisting of MnO_2/CNT on silicon substrate were successfully fabricated by using the electrochemical deposition technique.
- In-situ deposition of MnO_2 on CNTs can be achieved by using cyclic voltammetry in a $KMnO_4$ solution. Parameters including the potential scan windw, potential scan rates, potassium permanganate concentration and CNT height were evaluated.

- Cyclic voltammetry in the negative potential region (0V to -1V) has a much higher deposition rate than that observed in the positive potential region (0V to +1V).
- The deposition rate varies inversely with the scan rate used. Increasing the scan rate reduces the deposition rate, thus providing better control.
- Increasing the potential scan limits at the same scan rate yields a better coverage of MnO_2 on the CNTs as inferred from the greater enhancement in the capacitive currents
- Increasing the potential scan limits at the same scan rate yields a better coverage of MnO_2 on the CNTs as inferred from the greater enhancement in the capacitive currents.
- Introducing a wait-period (60s) between successive CV scans during the deposition process may increase the proportion of CNTs covered. The deposition rate however is less than that with no wait-period.
- The deposition rate is directly proportional to the concentration of the $KMnO_4$ solution used. A lower concentration can be used to achieve better control at the same scan rate.
- Taller CNT height does not result in higher supercapacitance due to poor MnO_2 coverage in the interior of the CNT network.
- Excess MnO_2 limits the capacitance due to increased resistance and hinders cation diffusion.
- CNT synthesis on flexible graphite foil was achieved using the thermal CVD technique. MnO_2 coated CNTs on graphite substrate yield a maximum capacitance value of 240 mF/cm^2 and ~12x capacitance improvement over As-synthesized CNTs.

- Double-sided electrodes were successfully achieved by CNT synthesis on both sides of the graphite foil substrate in a tube furnace.
- A high capacitance of 1.8 F/cm^2 was achieved from a single double sided MnO_2/CNT/Graphite electrode.
- The prototype supercapacitor cell delivers a very high total capacitance of 3.7F. The highest capacitance and low equivalent series resistance (ESR) value of 0.8 Ω yields a maximum specific power value of 68.5 $kW.kg^{-1}$ and a maximum specific energy of 111.6 Wh. kg^{-1} at 2.5V.

6.1.2 3D Micro Patterned Supercapacitor Electrodes

- Conventional silicon microfabrication, the CVD technique for CNT synthesis and the electrochemical technique for MnO_2 deposition were combined to fabricate a 3D micropatterned microelectrode array
- Optimized combination of the CNT structure and the efficient in-situ electro deposition of MnO_2 can yield a 3-D micropatterned array that can deliver much higher capacitance values: C= ~1800mF/cm^2 or 240 F/cm^3→ 200x enhancement over as-synthesized CNTs.

6.1.3 Solid-State Supercapacitors

- Solid-state electrolytes (PVA/H_3PO_4) were successfully fabricated by spin coating method on the highly flexible graphite substrate.
- The effective electrolyte thickness of 10 μm was obtained for the electrodes to overcome the electrical shorting problem.

- A solid-state supercapacitor cell based on CNT/Graphite electrodes was successfully fabricated and the highest capacitance of 30.18 mF/cm^2 was achieved with a 90% concentration of H_3PO_4 in the solid electrolyte.
- As the acid concentration increases, the conductivity of the solid-state electrolyte increases several orders of magnitude and further confirms the enhanced performance of the device.
- A solid-state supercapacitor cell based on CNT/MnO_2 electrodes was successfully fabricated and the highest specific capacitance of 21.31 $F.g^{-1}$ was achieved at scan rate of 5 mV/s within 0-1.5V.
- A solid-state supercapacitor cell based on 3-D nanostructured MnO_2/CNT micro electrode array achieved a specific capacitance of 110 $F.g^{-1}$ which is almost 7*x* times higher than that observed for the planar structured solid-state supercapacitors.
- The solid-state electrolyte was etching the MnO_2 during the spin coating and was therefore responsible for the severely reduced specific capacitance. This result clearly indicates that the exposure to the electrolyte solution in liquid phase was not useful to fabricate MnO_2/CNT electrodes with solid-state electrolytes.
- A solid-state supercapacitor cell consisting of 3-D nanostructured MnO_2/CNT microelectrode array on highly flexible graphite foil and PVA/H_3PO_4 composite as a solid-state electrolyte/seperator were successfully fabricated and yielded a very high specific capacitance value of 1.4 F or 839 $F.g^{-1}$ at $1mv.s^{-1}$ scan rate.
- A new, efficient, simple, and low-cost process has been developed for the fabrication of solid-state supercapacitors. The resulted structure demonstrates outstanding

capacitance behavior with high specific energy and power density and excellent cycle life.

6.2 Recommendations for future work

This dissertation has introduced several ideas to fabricate planar macro supercapacitors, 3D micro supercapacitors, and solid-state supercapacitors with improved electrochemical performance. There are new possibilities for development of supercapacitors based on the information gathered from this research. Some recommendations for future work include:

(i). Designing and fabricating a 3D micro-supercapacitor with an inter-digitated array (IDA) which would provide a pair of co-planar electrodes which eliminating the need for a separator film and increasing the speed of the device; by incorporating MnO_2 on the high specific surface area CNTs, very high specific energy and power values can be achieved.

(ii). Optimize the deployment of solid electrolyte onto the 3D IDA structure which would promote ease of packaging, without any risk of leakage and would eliminate the risk posed from flammable electrolytes.

(iii). Investigation of novel electrode active materials for higher capacitance supercapacitors.

(iv). Optimize the recipes of solid- state electrolytes for capacitance enhancement while minimizing their negative impact on the electrodes.

(v). Investigation of different solid-state electrolytes for the solid-state supercapacitors.

(vi). A more detailed study could be done of MnO_2/CNT electrodes with solid-state electrolytes to improve the life cycle and the operating voltage window, which will be beneficial in increasing the energy density and overall performance.

(vii). Further understand the physical and chemical processes at electrode-electrolyte interfaces and develop new designs.

PUBLICATIONS

1. Serkan Akbulut, M. Yilmaz, Supil Raina, Shao-Hua Hsu, Weng Poo Kang. "Solid-state supercapacitor cell based on 3D nanostructured MnO_2/CNT microelectrode array on graphite and H_3PO_4/PVA electrolyte", *Diamond and Related Materials*, Volume 74, April 2017, Pages 222-228, ISSN 0925-9635.
2. Serkan Akbulut, M. Yilmaz, Supil Raina, Shao-Hua Hsu, Weng Poo Kang "Advanced Supercapacitor Prototype Using Nanostructured Double-Sided MnO_2/CNT Electrodes on Flexible Graphite Foil", *Journal of Applied Electrochemistry*, JACH-D-16-01085, Accepted, In Press.

APPENDIX

SUPERCAPACITORS PERFORMANCE EVALUATION

Table A.1 Summary of the Planar Macro Supercapacitors in the literature.

Reference No	Electrode active material	Cell capacitance (F or mF/cm^2)	Specific Energy Density ($Wh\ kg^{-1}$ or $Wh\ cm^{-3}$)	Specific Power Density ($Wh\ kg^{-1}$ or $W\ cm^{-3}$)
150	MnO_2/Si Nanowires	27 mF/cm^{-2}	0.17 $mWh\ cm^{-3}$	16 $mW\ cm^{-3}$
151	RuO_2/Si/Au	99 mF/cm^2	12 $mWh\ cm^{-3}$	5 $mW\ cm^{-3}$
152	PANI/MnO_2	0.48 F	5.9 $Wh\ kg^{-1}$	42.1 $kW\ kg^{-1}$
153	Activated Carbon/MnO_2	31 mF/cm^2	17.3 $Wh\ kg^{-1}$	19 $kW\ kg^{-1}$
154	Fe_3O_4/MnO_2	18 mF/cm^2	10.2 $Wh\ kg^{-1}$	8.1 $kW\ kg^{-1}$
155	MnO_2/MnO_2	2.5 F/cm^{-3}	3.1 $Wh\ kg^{-1}$	3.3 $kW\ kg^{-1}$
156	AC/MnO_2	109 mF/cm^2	7 $Wh\ kg^{-1}$	10 $kW\ kg^{-1}$
OUR SC	CNT/MnO_2	**2.25 F or 187.8 mF/cm^2**	**22.68 $Wh\ kg^{-1}$**	**12.4 $kW\ kg^{-1}$**

Table A.2 Summary of the Micro Supercapacitors in the literature.

Reference No	Electrode active material	Cell capacitance (F/cm^2)	Cell capacitance (F/cm^3)
157	Activated carbon	0.9	80.64
158	Carbide-drived Carbon	0.45	160
159	MnO_2/Si MicroTubes	0.67	166
160	MnO_2/SnO_2	0.98	----
161	RuO_2/Pt Nanotubes	0.3	196
162	MnO_2/C/Al nanowall	1.08	196
163	RuO_2/C/Al nanowall	1.2	212
OUR SC	CNT/MnO_2	**1.8**	**240**

Table A.3 Summary of the Solid-State Supercapacitors in the literature.

Reference No	Electrode active material	Cell capacitance (F or mF/cm^2)	Specific Energy Density ($Wh\ kg^{-1}$ or $Wh\ cm^{-3}$)	Specific Power Density ($Wh\ kg^{-1}$ or $W\ cm^{-3}$)
164	Graphene/Carbon Cloth	0.84 F	1.64 $Wh\ kg^{-1}$	72 $kW\ kg^{-1}$
165	CNTs/Bacterial nano cellulose	20.2 mF/cm^2	15.5 $Wh\ kg^{-1}$	1.5 $kW\ kg^{-1}$
166	Ppy/MnO_2	0.48 F	6.16 $Wh\ cm^{-3}$	0.04 $W\ cm^{-3}$
167	PANI/CNTs	14.6 mF/cm^2	7.1 $Wh\ kg^{-1}$	2.2 $kW\ kg^{-1}$
168	Graphene/SSCs	4.8 mF/cm^2	1.36 $Wh\ kg^{-1}$	20 $kW\ kg^{-1}$
169	MnO_2/Carbon Core-shell fiber	2.5 F/cm^{-3}	2.22 $Wh\ cm^{-3}$	0.4 $W\ cm^{-3}$
170	Carbon Nanoparticles MnO_2/SSCs	109 mF/cm^2	71 $Wh\ kg^{-1}$	39 $kW\ kg^{-1}$
OUR SC	CNT/MnO_2	**1.4 F or 195.5 mF/cm^2**	**115.2 $Wh\ kg^{-1}$**	**73.9 $kW\ kg^{-1}$**

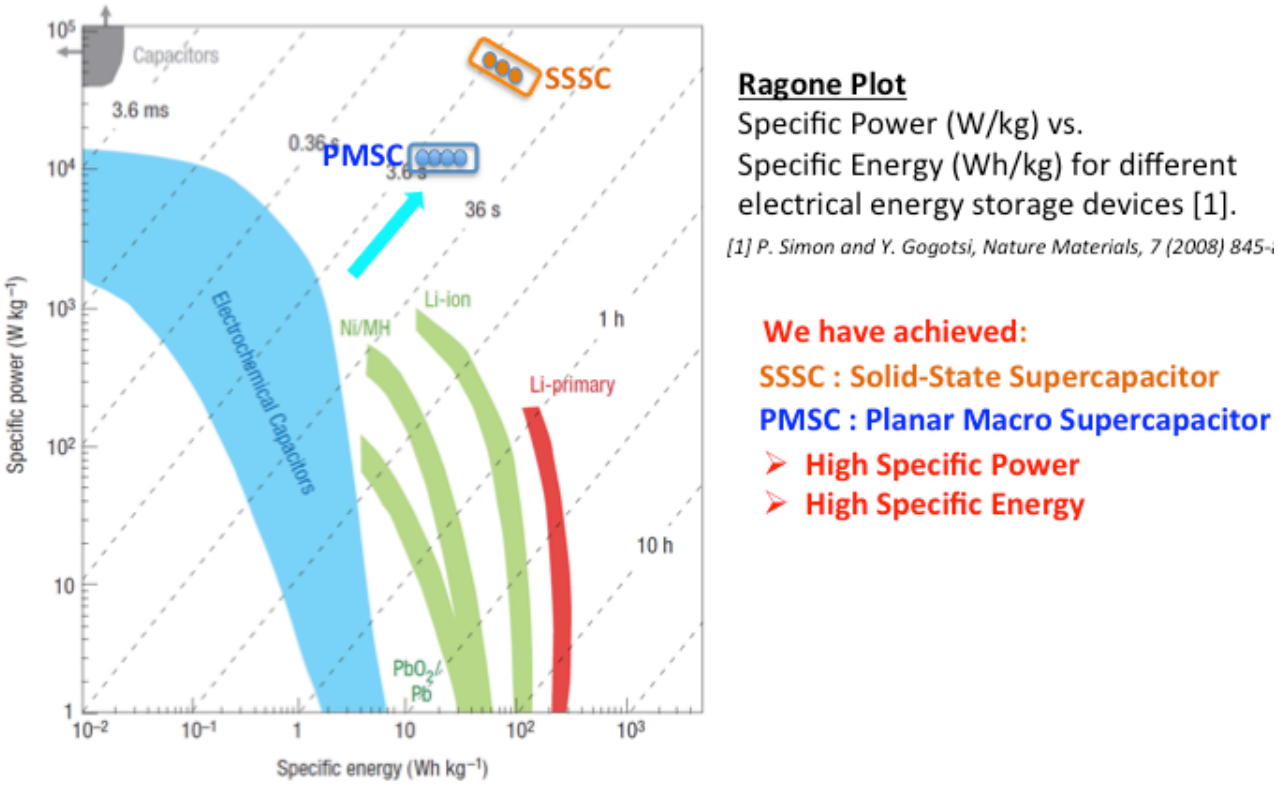

Figure A.1 Ragone plot for energy storage devices.

REFERENCES

[1] Q. Cheng, J. Ma, H. Zhang, N. Shinya, L.-C. Qin, J. Tang, "Electrodeposition of MnO_2 on Carbon Nanotube Thin Films as Flexible Electrodes for Supercapacitors," *Transactions of the Materials Research Society of Japan*, 2010,vol. 35, issue 2, pp. 369-372.

[2] Wang, Yaohui, "Manganese dioxide based composite electrodes for electrochemical supercapacitors" Open Access Dissertations and Theses. Paper 7437, McMaster University, 2012.

[3] Guihua Yu, Xing Xie, Lijia Pan, Zhenan Bao, Yi Cui, "Hybrid nanostructured materials for high-performance electrochemical capacitors. *Nano Energy*, 2, 213 (2013).

[4] S. Akbulut, "Optimization of carbon nanotube supercapacitor electrode," M.S. thesis, Dept. Elect. Eng., Vanderbilt Univ., Nashville, TN, 2011.

[5] J. Li, X. Cheng, A. Shashurin and M. Keidar, "Review of Electrochemical Capacitors Based on Carbon Nanotubes and Graphene," *Graphene*, No. 1, Vol. 1, 2012, pp. 1-13.

[6] Burak Caglar, "Production of Carbon Nanotubes by PECVD and Their Applications to Supercapacitors," Dept. App. Physics and Optics, Universitat de Barcelona, Barcelona, Spain, 2010.

[7] Beidaghi, Majid, "Design, Fabrication, and Evaluation of On-chip Micro-supercapacitors" (2012). FIU Electronic Theses and Dissertations. Paper 660.

[8] Wei Sun, " Three dimensional MEMS supercapacitors" (2011). Faculty of Mathematics and Natural Sciences, University of Oslo, No. 1042,ISSN 1501-7710.

[9] R. Miller, A. F. Burke, *The Electrochemical Society interface*, spring 2008.

[10] G. Wang, L. Zhang, J. Zhang, *Chem. Soc. Rev.* 41 (2012) 797-828.

[11] Zhang Li Li," Carbon-Based Materials As Supercapacitor Electrodes" (2010). National University of Singapore.

[12] Majid Beidaghi, Chunlei Wang, Micro-supercapacitors based on three dimensional interdigital polypyrrole/C-MEMS electrodes, *Electrochimica Acta*, Volume 56, Issue 25, 30 October 2011, Pages 9508-9514, ISSN 0013-4686, http://dx.doi.org/10.1016/j.electacta.2011.08.054.

[13] M. Beidaghi, W. Chen, C. Wang, *J. Power Sources* 2011, 196, 2403.

[14] M. Xue, Z. Xie, L. Zhang, X. Ma, X. Wu, Y. Guo, W. Song, Z. Li, T. Cao, *Nanoscale* 2011, 3, 2703-8.

[15] K. Wang, W. Zou, B. Quan, A. Yu, H. Wu, P. Jiang, Z. Wei, Adv. *Energy Mater*, 2011, 1, 1068-1072.

[16] M. Heon, S. Lofland, J. Applegate, R. Nolte, E. Cortes, J. D. Hettinger, P.L. Taberna, P. Simon, P. Huang, M. Brunet, Y. Gogotsi, *Energy Environ. Sci*. 2011,4, 135.

[17] Patrice Simon, Andrew Burke, "Nanostructured carbons: Double Layer Capacitance and More", *The Electrochemical Society Interface*, Spring 2008, 38-45

[18] M. Kaempgen, C. K. Chan, J. Ma, Y. Cui, G. Gruner, *Nano let*. 2009, 9, 1872.

[19] Siyu Wei, "Field emitters and supercapacitors based on carbon nanotube films," Ph.D. dissertation, Dept. Elect. Eng., Vanderbilt Univ., Nashville, TN, 2009.

[20] Christopher M. Anton and Matthew H. Ervin, Carbon Nanotube Based Flexible Supercapacitors, April 2011.

[21] Helena Malmberg, "Nanoscientific investigations of electrode materials for supercapacitors," Ph.D. dissertation, Chemical Science and Engineering, Kungliga Tekniska högskolan, Lindstedtsvägen, Stockholm, 2007.

[22] Wen-wen Liu, Xing-bin Yan, Jun-wei Lang, Chao Penga and Qun-ji Xue, "Flexible and conductive nanocomposite electrode based on graphene sheets and cotton cloth for supercapacitor," *Journal of Materials Chemistry*, 2012, vol. 22, pp. 17245- 17253.

[23] J.H Chen, W.Z Li, D.Z Wang, S.X Yang, J.G Wen, Z.F Ren, "Electrochemical characterization of carbon nanotubes as electrode in electrochemical double-layer capacitors," *Carbon*, Volume 40, Issue 8, July 2002, Pages 1193-1197.

[24] P. Simon, Y. Gogotsi, Nature Materials 7 (2008) 845.

[25] Guihua Yu, Xing Xie, Lijia Pan, Zhenan Bao, Yi Cui, Hybrid nanostructured materials for high-performance electrochemical capacitors, *Nano Energy*, Volume 2, Issue 2, March 2013, Pages 213-234, ISSN 2211-2855, http://dx.doi.org/10.1016/j.nanoen.2012.10.006.

[26] Melanie Elisa Guittet, Adrianus I. Aria, and Morteza Gharib, "Use of Vertically-Aligned Carbon Nanotube Array to Enhance the Performance of Electrochemical Capacitors," IEEE Nano 2011, 11th International Conference on Nanotechnology.

[27] J. J. Yoo, K. Balakrishnan, J. Huang, V. Meunier, B. G. Sumpter, A. Srivastava, M. Conway, A. L. M. Reddy, J. Yu, R. Vajtai, P. M. Ajayan, *Nano lett*. 2011, 11,1423.

[28] V. Shanov, Yeo-Heung Yun, M. J. Schulz, "Synthesis and characterization of carbon nanotube materials," *Journal of the University of Chemical Technology and Metallurgy*, 2006, vol. 35, issue. 4, pp. 377-390.

[29] Veronica Augustyn, Jérémy Come, Michael A. Lowe, Jong Woung Kim, Pierre-Louis Taberna, Sarah H. Tolbert, Héctor D. Abruña, Patrice Simon & Bruce Dunn, "High-rate electrochemical energy storage through Li+ intercalation pseudocapacitance" *Nature Materials 12, 518–522 (2013) doi:10.1038/nmat3601*

[30] Nae-Lih Wu. (2002). Nanocrystalline oxide supercapacitors. *Materials Chemistry and Physics*. doi:10.1016/s0254-0584(02)00022-6

[31] Sofiane Boukhalfa, Kara Evanoff and Gleb Yushin, "Atomic layer deposition of vanadium oxide on carbon nanotubes for high-power supercapacitor electrodes," *Energy Environ. Sci*. 2012, vol.5, pp. 6872.

[32] Xiaoping Dong, Weihua Shen, Jinlou Gu, Liangmin Xiong, Yufang Zhu, Li, and, and Jianlin Shi, "MnO2-Embedded-in-Mesoporous-Carbon-Wall Structure for Use as Electrochemical Capacitors," *The Journal of Physical Chemistry*, 2006, vol. 110, issue. 12, pp. 6015-6019.

[33] Zhiyi Lu, Qiu Yang, Wei Zhu, Zheng Chang, Junfeng Liu, Xiaoming Sun, David G. Evans, Xue Duan, "Hierarchical Co3O4@Ni-Co-O supercapacitor electrodes with ultrahigh specific capacitance per area," *Nano Research*, March 2012, Volume 5, Issue 5 , pp 369-378.

[34] Torsten Brezesinski, John Wang, Sarah H. Tolbert & Bruce Dunn, "Ordered mesoporous α-MoO3 with iso-oriented nanocrystalline walls for thin-film pseudocapacitors," *Nature Materials,* 2010, volume 9, pp.146–151.

[35] David Pech, Magali Brunet, Hugo Durou, Peihua Huang, Vadym Mochalin, Yury Gogotsi, Pierre-Louis Taberna& Patrice Simon "Ultrahigh-power micrometre-sized supercapacitors based on onion-like carbon," *Nature Nanotechnology* 5, 651–654 (2010) doi:10.1038/nnano.2010.162

[36] Weifeng Wei, Xinwei Cui, Weixing Chena and Douglas G. Ivey, "Manganese oxide-based materials as electrochemical supercapacitor electrodes," *Chem. Soc. Rev*, 2011, volume 40, Issue 3, pp. 1697-1721.

[37] Liangbing Hu, Wei Chen, Xing Xie, Nian Liu, Yuan Yang, Hui Wu, Yan Yao, Mauro Pasta, Husam N. Alshareef, and Yi Cui, "Symmetrical MnO2–Carbon Nanotube–Textile Nanostructures for Wearable Pseudocapacitors with High Mass Loading," *ACS Nano,* 2011, vol.5, no. 11, pp. 8904-8913.

[38] Fang Xiao, Youlong Xu, "Electrochemical co-deposition and characterization of MnO2/SWNT composite for supercapacitor application," *J Mater Sci: Mater Electron,* 2013, vol.24, pp. 1913-1920.

[39] A. Brandt, S. Pohlmann, A. Varzi, A. Balducci and S. Passerini, *MRS Bull.*, 2013, 38, 554–559.

[40] N. A. Choudhury, S. Sampath and A. K. Shukla, *Energy Environ. Sci*., 2009, 2, 55–67.

[41] H. Gao and K. Lian Proton-conducting polymer electrolytes and their applications in solid supercapacitors: a review, *RSC Adv*., 2014, 4, 33091–33113.

[42] Cheng Zhong, Yida Deng, Wenbin Hu, Jinli Qiao, Lei Zhang, and Jiujun Zhang, "A review of electrolyte materials and compositions for electrochemical supercapacitors*", Chem. Soc. Rev*., 2015,44, 7484-7539.

[43] M. Ue, K. Ida and S. Mori, J. *Electrochem. Soc*., 1994, 141,2989–2996.

[44] M. Deschamps, E. Gilbert, P. Azais, E. Raymundo-Pin˜ero, M. R. Ammar, P. Simon, D. Massiot and F. BeÅLguin, *Nat. Mater*. 2013, 12, 351–358.

[45] K. Naoi, *Fuel Cells*, 2010, 10, 825–833.

[46] K. Chiba, T. Ueda, Y. Yamaguchi, Y. Oki, F. Saiki and K. Naoi, J. *Electrochem. Soc*., 2011, 158, A1320–A1327.

[47] A. Janes, T. Thomberg, J. Eskusson and E. Lust, *J. Electrochem. Soc*., 2013, 160, A1025–A1030.

[48] S. F. Tian, L. Qi, M. Yoshio and H. Y. Wang, *J. Power Sources*, 2014, 256, 404–409.

[49] M. Armand, F. Endres, D. R. MacFarlane, H. Ohno and B. Scrosati, *Nat. Mater*., 2009, 8, 621–629.

[50] P. Wasserscheid and T. Welton, Ionic liquids in synthesis, *Wiley-VCH Verlag* GmbH & Co. KGaA, 2002.

[51] B. E. Francisco, C. M. Jones, S. H. Lee and C. R. Stoldt, *Appl. Phys. Lett*., 2012, 100, 103902.

[52] A. S. Ulihin, Y. G. Mateyshina and N. F. Uvarov, *Solid State Ionics*, 2013, 251, 62–65.

[53] A. A. ŁatoszynÅLska, G. Z. Zukowska, I. A. Rutkowska, P. L. Taberna, P. Simon, P. J. Kulesza and W. Wieczorek, *J. Power Sources*, 2014, 274, 1147,1154.

[54] Y.D. Chiou, D.-S. Tsai, H. H. Lam, C.-h. Chang, K.-Y. Lee and Y.-S. Huang, *Nanoscale*, 2013, 5, 8122–8129.

[55] H. Gao, J. Li and K. Lian, *RSC Adv.,* 2014, 4, 21332–21339.

[56] C.C. Yang, S.-T. Hsu and W.-C. Chien, *J. Power Sources*, 2005, 152, 303–310.

[57] H.K. Kim, S.-H. Cho, O. Young-Woo, T.-Y. Seong and Y. S. Yoon, J. Vac. Sci. Technol., B: Microelectron.Nanometer Struct.–Process., Meas., Phenom., 2003, 21, 949–952.

[58] L. M. Miller, P. K. Wright, C. C. Ho, J. W. Evans, P. C. Shafer and R. Ramesh, in Energy Conversion Congress and Exposition, 2009, ECCE 2009, IEEE, 2009, pp. 2627–2634.

[59] K. Yu Jin, C. Haegeun, H. Chi-Hwan and K. Woong, *Nanotechnology*, 2012, 23, 065401.

[60] M. F. El-Kady and R. B. Kaner, *Nat. Commun*., 2013, 4, 1475.

[61] S. Ketabi, Z. Le and K. Lian, *Electrochem. Solid-State Lett*., 2011, 15, A19–A22.

[62] S. Ketabi and K. Lian, *Electrochim. Acta*, 2013, 103, 174–178.

[63] D. E. Fenton, J. M. Parker, P. V. Wright, Complexes of alkali metal ions with poly(ethylene oxide), Polymer, 14 (1973) 589.

[64] Z. Wang, B. Huang, H. Huang, R. Xue, L. Chen, and F. Wang, A vibrational spectroscopic study on the interaction between lithium salt and ethylene carbonate plasticizer for PAN-based electrolytes, *J. Electrochem. Soc*., 143 (1996) 1510-1514.

[65] Y.S. Yoon, W. I. Cho, J. H. Lim, D. J. Choi, Solid-state thin-film supercapacitor with ruthenium oxide and solid electrolyte thin films, *J. Power Sources*, 101 (2001) 126-129.

[66] K. W. Park, H. J. Ahn; Y. E. Sung, All-solid-state supercapacitor using a Nafion(R) polymer membrane and its hybridization with a direct methanol fuel cell, *J.Power Sources*, 109 (2002) 500-506.

[67] Sung JH, Kim S, Lee KH. Fabrication of all-solid-state electrochemical microcapacitors. *J Power Sources* 2004;133:312-9.

[68] Long, J. W., Rolison, D. R., Dunn, B., White, H. S., "Three-Dimensional Battery Architectures," *Chem. Rev*. 104,4463-4492.

[69] Sung, J.W., Kim, S.-J., and Lee, K.-H., "Fabrication of all-solid-state electrochemical microcapacitors," *J. Power Sources* 133, 312-319 (2004).

[70] Sun, W., Chen, X., "Preparation and characterization of polypyrrole films for three-dimensional microsupercapacitor," *J. Power Sources* 193, 924-929.

[71] Y. Q. Jiang, Q. Zhou, L. Lin, Micro Electro Mechanical Systems, 2009. MEMS 2009. IEEE 22nd International Conference on, 25-29 Jan. 2009, Sorrento, Italy.

[72] C. Shen, X. Wang, W. Zhang, F. Kang, *J. Power Sources* 196 (2011) 10465-10471.

[73] Y. Xie, C. Huang, L. Zhou, Y. Liu, H. Huang, *Composites Science and Technology* 69 (2009) 2108-2114.

[74] P. Banerjee, I. Perez, L. H. Lecordire, S. B. Lee, G. W. Rubloff, *Nature nanotechnology*, letters, DOI:10.1038/nnano.2009.37.

[75] S. M. George, *Chem. Rev.* 110 (2010) 111-131.

[76] J. Chmiola, C. Largeot, P.L. Taberna, P. Simon, Y. Gogotsi, *Science* 328 (2010) 480-483.

[77] M. Heon, S. Lofland, J. Applegate, R. Nolte, E. Cortes, J.D. Hettinger, P.-L. Taberna, P. Simon, P. Huang, M. Brunet, Y. Gogotsi, *Energy Environ. Sci*. 4 (2011) 135.

[78] D. Pech, M. Brunet, H. Durou, P. Huang, V. Mochalin, Y. Gogotsi, P. -L. Taberna, P. Simon, *Nat. Nanotechnol*. 5 (2010) 651-654.

[79] Pech, D., Brunet, M., Taberna, P.–L., Simon, P., Fabre, N., Mesnilgrente, F., Conedera, V., and Durou, H.,"Elaboration of a microstructured inkjet-printed carbon electrochemical capacitor," *J. Power Sources* 195, 1266–1269 (2010).

[80] C. -C. Liu, D. -S. Tsai, D. Susanti, W. -C. Yeh, Y. -S. Huang, F. -J. Liu, *Electrochim. Acta* 55 (2010) 5768-5774.

[81] M. Xue, Z. Xie, L. Zhang, X. Ma, X. Wu, Y. Guo, W. Song, Z. Li, T. Cao, *Nanoscale* 3 (2011) 2703-8.

[82] W. Gao, N. Singh, L. Song, Z. Liu, A. L. M. Reddy, L. Ci, R. Vajtai, Q. Zhang, B.Wei, P. M. Ajayan, *Nat. Nanotechnol*. 6 (2011) 6-10.

[83] Chamran, F., Yeh, Y., Min, H.-S., Dunn, B., and Kim, C-J., "Fabrication of High-Aspect-Ratio Electrode Arrays for Three-Dimensional Microbatteries," *J. Microelectromech. Syst*., 16(4), 844-852 (2007).

[84] Menachem Nathan, Diana Golodnitsky, et al.,"Three-Dimensional Thin-Film Li-Ion Microbatteries for Autonomous Mems, *Journal of Microelectromechanical Systems*," Vol. 14, No. 5, October 2005,879~885.

[85] Golodnitsky, D., Nathan, M., Yufit, V., Strauss, Freedman, K., Burstein, L., Gladkich, A., and Peled, E., "Progress in three-dimensional (3D) Li-ion microbatteries,"*Solid State Ionics* 177, 2811–2819.

[86] Cheah, S. K., Perre, E., Rooth, M., Fondell, M., Harsta, A., Nyholm, L., Boman, M., Gustafsson, T., Lu, J., Simon,P., and Edstrom, K., "Self-Supported Three-Dimensional Nanoelectrodes for Microbattery Applications," *Nano Lett*.9(9), 3230-3233.

[87] C. Zhao, C. Wang, Z. Yue, K. Shu, G.G. Wallace, Intrinsically Stretchable Supercapacitors Composed of Polypyrrole Electrodes and Highly Stretchable Gel Electrolyte, *ACS Applied Materials & Interfaces*, 5(2013) 9008-9014.

[88] C. Meng, C. Liu, L. Chen, C. Hu, S. Fan, Highly Flexible and All-Solid-State Paperlike Polymer Supercapacitors, *Nano Letters*, 10(2010) 4025-4031.

[89] Q. Wang, J. Xu, X. Wang, B. Liu, X. Hou, G. Yu, P. Wang, D. Chen, G. Shen, Core– Shell CuCo2O4@MnO2 Nanowires on Carbon Fabrics as High-Performance Materials for Flexible, All-Solid-State, Electrochemical Capacitors, *ChemElectroChem*, (2013).

[90] M. Sawangphruk, M. Suksomboon, K. Kongsupornsak, J. Khuntilo, P. Srimuk, Y. Sanguansak, P. Klunbud, P. Suktha, P. Chiochan, High-performance supercapacitors based on silver nanoparticle-polyaniline-graphene nanocomposites coated on flexible carbon fiber paper, *Journal of Materials Chemistry A*, (2013).

[91] B. Liu, B. Liu, Q. Wang, X. Wang, Q. Xiang, D. Chen, G. Shen, New Energy Storage Option: Toward ZnCo2O4 Nanorods/Nickel Foam Architectures for High-Performance Supercapacitors, *ACS Applied Materials & Interfaces*, 5(2013) 10011-10017.

[92] S.T. Senthilkumar, R.K. Selvan, J.S. Melo, C. Sanjeeviraja, High Performance Solid-State Electric Double Layer Capacitor from Redox Mediated Gel Polymer Electrolyte and Renewable Tamarind Fruit Shell Derived Porous Carbon, *ACS Applied Materials & Interfaces*, 5(2013) 10541-10550.

[93] M. F. El-Kady and R. B. Kaner, "Scalable fabrication of high-power graphene microsupercapacitors for flexible and on-chip energy storage," *Nat. Commun*.,vol. 4, p. 1475, February 2013.

[94] S. T. Senthilkumar, R. K. Selvan, N. Ponpandian and J. S. Melo, "Redox additive aqueous polymer gel electrolyte for an electric double layer capacitor," *RSC Adv*, vol. 2, pp. 8937-8940, 2012.

[95] A. B. Dalton, S. Collins, E. Munoz, J. M. Razal, V. H. Ebron, J. P. Ferraris, J. N. Coleman, B. G. Kim and R. H. Baughman, "Super-tough carbon-nanotube fibres," *Nature*, vol. 423, p. 703, 2003.

[96] C. Meng, C. Liu, L. Chen, C. Hu and S. Fan, "Highly flexible and all-solid-state paperlike polymer supercapacitors," *Nano Lett*, vol. 10, pp. 4025-4031, 2010.

[97] V. Shanov, Yeo-Heung Yun, M. J. Schulz, *Journal of the University of Chemical Technology and Metallurgy*, 41, 4, 2006, 377-390.

[98] Nikkon Ghosh, "CNT Field Emission Cell with Built-in Electron Beam Source for Electron Stimulated Amplified Field Emission", Electrical Engineering & Computer Science of Vanderbilt University, August 2008

[99] http://en.wikipedia.org/wiki/Carbon_nanotube

[100] A.V. Melechko, V.E. Merkulov, M.A. Guillorn, K.L. Klein, D.H. Lowndes, M.L. Simpson, *Journal of Applied Physics* 97, 041301, 2005

[101] S. C. Pang, M. A. Anderson, and T. W. Chapman, *J. Electrochem. Soc*., 147, 444 (2000).

[102] Ajuba, A.E., S.C. Ezugwu, B.A. Ezekoye, F.I. Ezema and P.U. Asogwa, 2010. Influence of pH on the structural, optical and solid state properties of chemical bath deposited ZnO thin films. *J. Optoelectron. Biomed. Mater*., 2: 73-78.

[103] Chigane M, Ishikawa M, Inoue H. Further XRD characterization of electrochromic nickel oxide thin films prepared by anodic deposition. *Sol Energ Mat Sol C*. 2000;64:65–7.

[104] Al-Hamdane, N.A., Habubi, N.F, Gasgus, B.A., 2002, *J. of Al Fath*, 15, 328.

[105] C. C. Hu and T. W. Tsou, *Electrochem. Comm*. 4 (2002) 105.

[106] Gao, T., Fjellvåg, H., Norby, P. (2009). A comparison study on Raman scattering properties of α- and β-MnO_2. Anal. Chim. Acta, 648(2):235-239. doi:10.1016/j.aca.2009.06.059.

[107] Xiao, C., Chen, J., Liu, B., Chu, X., Wu, L., Yao, S. (2011). Sensitive and selective electrochemical sensing of l-cysteine based on a caterpillar-like manganese dioxide–carbon nanocomposite. *Phys. Chem. Chem. Phys*., 13(4):1568-1574. doi:10.1039/c0cp00980f.

[108] Buciuman, F., Patcas, F., Craciun, R., Zahn, D. R. (1999). Vibrational spectroscopy of bulk and supported manganese oxides. *Phys. Chem. Chem. Phys*., 1(1), 185-190. doi:10.1039/a807821a.

[109] Caiwei Shen, Xiaohong Wang, Siwei Li, Jian'gan Wang, Wenfeng Zhang, Feiyu Kang, A high-energy-density micro supercapacitor of asymmetric MnO2–carbon configuration by using micro-fabrication technologies, *Journal of Power Sources,* Volume 234, 15 July 2013, Pages 302-309, ISSN 0378-7753, http://dx.doi.org/10.1016/j.jpowsour.2012.10.101.

[110] A G Emsile, F T Bonner and L G Peek *J. Appl. Phys*. 29 858 (1958).

[111] D Meyerhofer *J. Appl. Phys*. A9 3993 (1978).

[112] D E Bornside, C W Macosko et al, *J. Imaging Tech*. 13 122 (1987).

[113] R K Yonkoski and D S Soane *J. Appl. Phys*. 72 725 (1992).

[114] C J Lawrence and W Zhou Journal of Non-Newtonian Fluid Mechanics 39 137 (1991).

[115] S Middleman An Introduction to Fluid Dynamics (New York : John Wiley and Sons) (1998).

[116] O Omar, A K Ray, A K Hassan and F Davis Supramolecular Science 4 417 (1997).

[117] Niranjan Sahu., B Parija and S.Panigrahi, "Fundamental understanding and modeling of spin coating". *Indian J. Phys*. 83 (4) 493-502 (2009).

[118] W W Flack, D S Soong, A T Bell and D W Hess *J. Appl. Phys*. 56 1199 (1983).

[119] http://www.cise.columbia.edu/clean/process/spintheory.pdf.

[120] http://www.mse.arizona.edu/faculty/birnie/Coatings.

[121] Ahmad Khiar, A. S., & Arof, A. K. (2010). Conductivity Studies of Starched-based polymer electrolytes. *Ionics*, 16, 123-129. http://dx.doi.org/ 10.1007/s11581-009-0356-y.

[122] Hashim, M. A, Sa'adu, L., Baharuddin, M., & Dasuki, A. K. (2014). Using PVA, Methacrylate and Lauroyl Chitosan as Separator in Supercapacitors. *Journal of Materials Science Research*, 3(1). http://dx.doi.org/ 10.5539/jmsr.v3n1p25.

[123] Hashmi, S. A. (2013). Polymer-Based Gel electrolytes for New Generation Supercapacitors. Paper presented at the Workshop on Advanced Energy Storage Materials & Devices (WAESD). Universiti Pertahanan Nasional Malaysia (National Defense University Malaysia).

[124] Jiang, L., Vangari, M., Pryor, T., Xiao, Z. & Korivi, N. S. (2013). Miniature Supercapacitors Based on Nanocomposite Thin Films. Microelectronic Engineering, 111, 52-57. http://dx.doi.org/10.1016/j.mee.2013.01.030.

[125] Prajapati, G. K., Roshan, R., & Gupta, P. N. (2010). Effect of plasticizer on ionic transport and dielectric properties of PVA-H3PO4 proton conducting polymeric electrolytes. *Journal of Physics and Chemistry of Solids*, 71, 1717-1723. http://dx.doi.org/10.1016/j.jpcs.2010.08.023.

[126] Nilesh R. Chodankar, Deepak P. Dubal, Abhishek C. Lokhande, Chandrakant D. Lokhande, Ionically conducting PVA–$LiClO_4$ gel electrolyte for high performance flexible solid state supercapacitors, *Journal of Colloid and Interface Science*, Volume 460, 15 December 2015, Pages 370-376, ISSN 0021-9797, http://dx.doi.org/10.1016/j.jcis.2015.08.046.

[127] Sun, Kanjun, Miaomiao Dong, Enke Feng, Hui Peng, Guofu Ma, Guohu Zhao, and Ziqiang Lei. "High performance solid state supercapacitor based on a 2-mercaptopyridine redox-mediated gel polymer." *RSC Advances* 5, no. 29 (2015): 22419-22425.

[128] E. Frackowiak, *Phys. Chem. Chem. Phys*. 9, 1774 (2007).

[129] D. P. Dubal, R. Holze, *Energy*, 51 (2013) 407.

[130] K. Chi, Z. Zhang, J. Xi, Y. Huang, F. Xiao, S. Wang, Y. Liu, *ACS Appl. Mater. Interfaces* 6, (2014) 16312.

[131] G. S. Gund, D. P. Dubal, S. S. Shinde, C. D. Lokhande, *ACS Appl. Mater. Interfaces*, 6 (2014) 3176.

[132] S. Wu, W. Chen, L. Yan, *J. Mater. Chem*. A, 2 (2014) 2765.

[133] P. Yang, Y. Ding, Z. Lin, Z. Chen, Y. Li, P. Qiang, M. Ebrahimi, W. Mai, C. P. Wong, Z. L. Wang, *Nano Lett*., 14 (2014) 731.

[134] Nilesh R. Chodankar, Deepak P. Dubal, Girish S. Gund, Chandrakant D. Lokhande, A symmetric MnO_2/MnO_2 flexible solid state supercapacitor operating at 1.6 V with aqueous gel electrolyte, *Journal of Energy Chemistry*, Volume 25, Issue 3, May 2016, Pages 463-471, ISSN 2095-4956, http://dx.doi.org/10.1016/j.jechem.2016.01.020.

[135] Suchetana Sadhukhan, "Preparation and characterization of polymer electrolyte," M.S. thesis, Dept. Phy., National Institute of technology , Rourkela, 2012.

[136] T. Gao, H. Fjellvag and P. Norby, "A comparison study on Raman scattering properties of alpha- and beta-MnO_2", *Analytica Chimica Acta,* 648, 235–239 (2009).

[137] C. Xiao, J. Chen, B. Liu, X. Chu, L. Wu and S. Yao, "Sensitive and selective electrochemical sensing of L-cysteine based on a caterpillar-like manganese dioxide – carbon nanocomposite", *Physical Chemistry Chemical Physics*, **13**, 1568-1574 (2011).

[138] J. G. Wang, D. Jin, R. Zhou, X. Li, X. Liu, C. Shen, K. Xie, B. Li, F. Kang, and B. Wei, "Highly Flexible Graphene/Mn_3O_4 Nanocomposite Membrane as Advanced Anodes for Li-Ion Batteries", *ACS Nano,* 10 (6), 6227-6234 (2016).

[139] B. Unnikrishnan, C. W. Wu, I. W. P. Chen, H. T. Chang, C.H. Lin, and C. C. Huang, "Carbon Dot-Mediated Synthesis of Manganese Oxide Decorated Graphene Nanosheets for Supercapacitor Application", *ACS Sustainable Chemistry & Engineering*, 4 (6), 3008-3016 (2016).

[140] Kang, J.; Hirata, A.; Kang, L.; Zhang, X.; Hou, Y.; Chen, L.; Li, C.; Fujita, T.; Akagi, K.; Chen, M. Angew. *Chem., Int. Ed*. **2013**, 52, 1664−1667.

[141] L. Yuan, X. H. Lu, X. Xiao, T. Zhai, J. Dai, F. Zhang, B. Hu, X. Wang, L. Gong, J. Chen, C. Hu, Y. Tong, J. Zhou, and Z. L. Wang, Flexible Solid-State Supercapacitors Based on Carbon Nanoparticles/MnO_2 Nanorods Hybrid Structure, *ACS Nano* ***2012*** 6 (1), 656-661.

[142] Xia, H.; Zhu, D. D.; Luo, Z. T.; Yu, Y.; Shi, X. Q.; Yuan, G. L.; Xie, *J. P. Sci. Rep.* **2013**, 3, 2978−2978.

[143] Zhang, J. H.; Wang, Y. H.; Zang, J. B.; Xin, G. X.; Ji, H. Y.; Yuan,Y. *G. Mater. Chem. Phys*. **2014**, 143, 595−599.

[144] Kim, J.; Ju, H.; Inamdar, A. I.; Jo, Y.; Han, J.; Kim, H.; *Im, H. Energy* **2014**, 70, 473−477.

[145] Dai, Y. M.; Tang, S. C.; Peng, J. Q.; Chen, H. Y.; Ba, Z. X.; Ma, Y. J.; Meng, X. K. Mater. *Lett.* **2014**, 130, 107−110.

[146] Yu, G.; Hu, L.; Vosgueritchian, M.; Wang, H.; Xie, X.;McDonough, J. R.; Cui, X.; Cui, Y.; Bao, Z. Solution-Processed Fraphene/MnO_2 Nanostructured Textiles for High-Performance Electrochemical Capacitors. *Nano Lett*. **2011**, 11, 2905–2911.

[147] Kim, J. H.; Lee, K. H.; Overzet, L. J.; Lee, G. S. Synthesis and Electrochemical Properties of Spin-Capable Carbon Nanotube Sheet/MnOx Composites for High-Performance Energy Storage Devices. *Nano Lett*. **2011**, 11, 2611–2617.

[148] Wu, Z. S.; Ren, W.; Wang, D. W.; Li, F.; Liu, B.; Cheng, H. M. High-Energy MnO_2 Nanowire/Graphene and Graphene Asymmetric Electrochemical Capacitors. *ACS Nano* **2010**,4, 5835–5842.

[149] Chen, P. C.; Shen, G.; Shi, Y.; Chen, H.; Zhou, C. Preparation and Characterization of Flexible Asymmetric Supercapacitors Based on Transition-Metal-Oxide Nanowire/SingleWalled Carbon Nanotube Hybrid Thin-Film Electrodes. *ACS Nano* **2010**, 4, 4403–4411.

[150] Deepak P. Dubal1, David Aradilla, Gérard Bidan, Pascal Gentile, Thomas J.S. Schubert, Jan Wimberg, Saïd Sadki, Pedro Gomez-Romero. 3D hierarchical assembly of ultrathin MnO2 nanoflakes on silicon nanowires for high performance micro-supercapacitors in Li-doped ionic liquid. *Scientific Reports* 5, Article number: 9771. (2015).

[151] Xiaofeng Wang, Yajiang Yin, Xiangyu Li, Zheng You, Fabrication of a symmetric micro supercapacitor based on tubular ruthenium oxide on silicon 3D microstructures, *Journal of Power Sources*, Volume 252, 2014, Pages 64-72, ISSN 0378-7753.

[152] Khomenko, V., Raymundo-Piñero, E., Frackowiak, E. et al. *Appl. Phys. A* (2006) 82: 567.

[153] M.S. Hong , S.H. Lee , S.W. Kim Use of KCl aqueous electrolyte for 2 V manganese oxide/activated carbon hybrid capacitor. *Electrochem. Solid-State Lett.* 2002 volume 5, issue 10, A227-A230.

[154] T. Brousse , D. Belanger A hybrid Fe3O4–MnO2 capacitor in mild aqueous electrolyte. *Electrochem. Solid-State Lett*. Volume 6, issue 11, A244-A248.

[155] J-Y. Luo , J-L. Liu , P. He , Y-Y. Xia A novel $LiTi_2(PO_4)_3/MnO_2$ hybrid supercapacitor in lithium sulfate aqueous electrolyte. *Electrochimica Acta*, Volume 53, Issue 28, Pages 8128-8133, ISSN 0013-4686.

[156] T. Brousse , M. Toupin , D. Bélanger A hybrid activated carbon-manganese dioxide capacitor using a mild aqueous electrolyte. *J. Electrochem. Soc.* Volume 151, issue 4, A614-A62.

[157] Wang, X., Yin, Y., Li, X. & You, Z. Fabrication of a symmetric micro supercapacitor based on tubular ruthenium oxide on silicon 3D microstructures. *Journal of Power Sources*, Volume 252, 2014, Pages 64-72, ISSN 0378-7753.

[158] J. Chmiola, C. Largeot, P. L. Taberna, P. Simon, Y. Gogotsi,. Hong , S.H. Lee , S.W. Kim. *Science* 2010, 328, 480.M.S.

[159] Seung Woo Lee, Junhyung Kim, Shuo Chen, Paula T. Hammond, and Yang Shao-Horn. Carbon Nanotube/Manganese Oxide Ultrathin Film Electrodes for Electrochemical Capacitors, *ACS Nano* 2010 4 (7), 3889-3896.

[160] Liu, Y. et al. Enhanced electrochemical performance of hybrid SnO_2@MOx (M = Ni, Co, Mn) core–shell nanostructures grown on flexible carbon fibers as the supercapacitor. *J. Mater. Chem. A*, 2015,3, 3676-3682.

[161] A. Ponrouch, S. Garbarino, E. Bertin, D. Guay. Ultra high capacitance values of Pt@RuO core–shell nanotubular electrodes for microsupercapacitor applications, *Journal of Power Sources*, Volume 221, 2013, Pages 228-231.

[162] Shuijian He, Ruizhong Zhang, Chunmei Zhang, Minmin Liu, Xiaohui Gao, Jian Ju, Lei Li, Wei Chen, Al/C/MnO sandwich nanowalls with highly porous surface for electrochemical energy storage, *Journal of Power Sources*, Volume 299, 2015, Pages 408-416.

[163] Ty Mai Dinh, Amine Achour, Sorin Vizireanu, Gheorghe Dinescu, Leona Nistor, Kevin Armstrong, Daniel Guay, David Pech, Hydrous RuO2/carbon nanowalls hierarchical structures for all-solid-state ultrahigh-energy-density micro-supercapacitors, *Nano Energy*, Volume 10, November 2014, Pages 288-294, ISSN 2211-2855.

[164] S. Y. Wang, B. Pei, X. S. Zhao and R. A. W. Dryfe, *Nano Energy*, 2, 530J.

[165] Y. J. Kang, S. J. Chun, S. S. Lee, B. Y. Kim, J. H. Kim, H. Chung, S. Y. Lee and W. Kim, *ACS Nano*, 6, 6400.

[166] J. Tao, N. Liu, W. Ma, L. Ding, L. Li, J. Su and Y. Gao, *Sci. Rep*., 3, 2286.

[167] C. Meng, C. Liu, L. Chen, C. Hu and S. Fan, *Nano Lett*., 10, 4025–4031.

[168] F. Meng, N. V. Aieta, S. F. Dec, J. L. Horan, D. Williamson, M. H. Frey, P. Pham, J. A. Turner, M. A. Yandrasits, S. J. Hamrock and A. M. Herring, *Electrochim. Acta*, 53, 1372–1378.

[169] X. Xiao, T. Li, P. Yang, Y. Gao, H. Jin, W. Ni, W. Zhan, X. Zhang, Y. Cao, J. Zhong, L. Gong, W.-C. Yen, W. Mai, J. Chen, K. Huo, Y.-L. Chueh, Z. L. Wang and J. Zhou, *ACS Nano*, 2012, 6, 9200–9206.

[170] L. Y. Yuan, X. H. Lu, X. Xiao, T. Zhai, J. J. Dai, F. C. Zhang, B. Hu, X. Wang, L. Gong, J. Chen, C. G. Hu, Y. X. Tong, J. Zhou and Z. L. Wang, *ACS Nano*, 2012, 6, 656 .